Type Ia Supernova Cosmology: Quantitative Spectral Analysis

Gastón Folatelli

Stockholm University
Department of Physics
2004

Doctoral Dissertation 2004
Department of Physics
Stockholm University
Sweden

ISBN 91-7265-847-9

Printed in Sweden by Universitetsservice US AB

Abstract

Type Ia supernovae have been successfully used as *standardized candles* to study the expansion history of the Universe. In the past few years, these studies led to the exciting result of an accelerated expansion caused by the repelling action of some sort of *dark energy*. This result has been confirmed by measurements of cosmic microwave background radiation, the large-scale structure, and the dynamics of galaxy clusters. The combination of all these experiments points to a "concordance model" of the Universe with flat large-scale geometry and a dominant component of dark energy.

However, there are several points related to supernova measurements which need careful analysis in order to doubtlessly establish the validity of the concordance model. As the amount and quality of data increases, the need of controlling possible systematic effects which may bias the results becomes crucial. Also important is the improvement of our knowledge of the physics of supernovae events to assure and possibly refine their calibration as standardized candle.

This thesis addresses some of those issues through the quantitative analysis of supernova spectra. The stress is put on a careful treatment of the data and on the definition of spectral measurement methods. The comparison of measurements for a large set of spectra from nearby supernovae is used to study the homogeneity and to search for spectral parameters which may further refine the calibration of the standardized candle. One such parameter is found to reduce the dispersion in the distance estimation of a sample of supernovae to below 6%, a precision which is comparable with the current lightcurve-based calibration, and is obtained in an independent manner. Finally, the comparison of spectral measurements from nearby and distant objects is used to test the possibility of evolution with cosmic time of the intrinsic brightness of type Ia supernovae.

Accompanying Papers

I. G. Folatelli, G. Garavini, S. Nobili, G. Aldering, R. Amanullah, P. Astier, C. Balland, G. Blanc, M. S. Burns, A. Conley, T. Dahlén, S. E. Deustua, R. Ellis, S. Fabbro, X. Fan, B. Frye, E. L. Gates, R. Gibbons, G. Goldhaber, B. Goldman, A. Goobar, D. E. Groom, D. Hardin, I. Hook, D. A. Howell, D. Kasen, S. Kent, A. G. Kim, R. A. Knop, B. C. Lee, C. Lidman, J. Mendez, G. Miller, M. Moniez, M. Mouchet, A. Mourão, H. Newberg, P. E. Nugent, R. Pain, N. Panagia, O. Perdereau, S. Perlmutter, V. Prasad, R. Quimby, J. Raux, N. Regnault, J. Rich, G. T. Richards, P. Ruiz-Lapuente, G. Sainton, B. Schaefer, K. Schahmaneche, E. Smith, A. L. Spadafora, V. Stanishev, N. A. Walton, L. Wang, W. M. Wood-Vasey, N. Yasuda, T. York
(THE SUPERNOVA COSMOLOGY PROJECT).
The Nearby Supernova Cosmology Project Spectroscopic Follow-up: Uncertainty Estimation for Quantitative Studies,
to be submitted.

II. G. Folatelli, G. Garavini, A. Goobar, S. Nobili, G. Aldering, R. Amanullah, P. Astier, C. Balland, G. Blanc, M. S. Burns, A. Conley, T. Dahlén, S. E. Deustua, R. Ellis, S. Fabbro, X. Fan, B. Frye, E. L. Gates, R. Gibbons, G. Goldhaber, B. Goldman, D. E. Groom, D. Hardin, I. Hook, D. A. Howell, D. Kasen, S. Kent, A. G. Kim, R. A. Knop, B. C. Lee, C. Lidman, J. Mendez, G. Miller, M. Moniez, M. Mouchet, A. Mourão, H. Newberg, P. E. Nugent, R. Pain, O. Perdereau, S. Perlmutter, V. Prasad, R. Quimby, J. Raux, N. Regnault, J. Rich, G. T. Richards, P. Ruiz-Lapuente, G. Sainton, B. Schaefer, K. Schahmaneche, E. Smith, A. L. Spadafora, V. Stanishev, N. A. Walton, L. Wang, W. M. Wood-Vasey, T. York
(THE SUPERNOVA COSMOLOGY PROJECT).
A new set of spectral quantities characterizing type Ia supernovae and their correlations with peak luminosity,
to be submitted.

III. G. Garavini, G. Folatelli, A. Goobar, S. Nobili, G. Aldering, A. Amadon, R. Amanullah, P. Astier, C. Balland, G. Blanc, M. S. Burns, A. Conley, T. Dahlén, S. E. Deustua, R. Ellis, S. Fabbro, X. Fan, B. Frye, E. L. Gates, R. Gibbons, G. Goldhaber, B. Goldman, D. E. Groom, J. Haissinski, D. Hardin, I. M. Hook, D. A. Howell, D. Kasen, S. Kent, A. G. Kim, R. A. Knop, B. C. Lee, C. Lidman, J. Mendez, G. J. Miller, M. Moniez, A. Mourão, H. Newberg, P. E. Nugent, R. Pain, O. Perdereau, S. Perlmutter, V. Prasad, R. Quimby, J. Raux, N. Regnault, J. Rich, G. T. Richards, P. Ruiz-Lapuente, G. Sainton, B. E. Schaefer, K. Schahmaneche, E. Smith, A. L. Spadafora V. Stanishev, N. A. Walton, L. Wang, W. M. Wood-Vasey

(THE SUPERNOVA COSMOLOGY PROJECT).
Spectroscopic Observations and Analysis of the Peculiar SN 1999aa,
AJ, submitted.

IV. G. Garavini, G. Folatelli, A. Goobar, C. Lidman, S. Nobili, G. Aldering, P. Astier, G. Blanc, M. S. Burns, A. Conley, S. E. Deustua, M. Doi, R. Ellis, S. Fabbro, A. S. Fruchter, S. Garmond, K. Garton, R. Gibbons, G. Goldhaber, D. E. Groom, D. Hardin, I. Hook, D. A. Howell, A. G. Kim, R. A. Knop, B. C. Lee, J. Mendez, P. E. Nugent, R. Pain, N. Panagia, C. R. Pennypacker S. Perlmutter, R. Quimby, J. Raux, N. Regnault, P. Ruiz-Lapuente, G. Sainton, B. Schaefer, K. Schahmaneche, E. Smith, A. L. Spadafora, V. Stanishev, M. Sullivan, N. A. Walton, L. Wang, W. M. Wood-Vasey, N. Yasuda
(THE SUPERNOVA COSMOLOGY PROJECT).
Search for spectral evolution in high-redshift Type Ia supernovae: evidence for an SN 1991T/SN 1999aa-like object at z=0.279,
to be submitted.

Other Related Papers

A. Knop, R. A., Aldering, G., Amanullah, R., Astier, P., Blanc, G., Burns, M. S., Conley, A., Deustua, S. E., Doi, M., Ellis, R., Fabbro, S., Folatelli, G., Fruchter, A. S., Garavini, G., Garmond, S., Garton, K., Gibbons, R., Goldhaber, G., Goobar, A., Groom, D. E., Hardin, D., Hook, I., Howell, D. A., Kim, A. G., Lee, B. C., Lidman, C., Mendez, J., Nobili, S., Nugent, P. E., Pain, R., Panagia, N., Pennypacker, C. R., Perlmutter, S., Quimby, R., Raux, J., Regnault, N., Ruiz-Lapuente, P., Sainton, G., Schaefer, B., Schahmaneche, K., Smith, E., Spadafora, A. L., Stanishev, V., Sullivan, M., Walton, N. A., Wang, L., Wood-Vasey, W. M., Yasuda, N.
New Constraints on Ω_M, Ω_Λ, and w from an Independent Set of 11 High-Redshift Supernovae Observed with the Hubble Space Telescope,
ApJ, 598,102–132 (2003).

B. Sullivan, M., Ellis, R. S., Aldering, G., Amanullah, R., Astier, P., Blanc, G., Burns, M. S., Conley, A., Deustua, S. E., Doi, M., Fabbro, S., Folatelli, G., Fruchter, A. S., Garavini, G., Gibbons, R., Goldhaber, G., Goobar, A., Groom, D. E., Hardin, D., Hook, I., Howell, D. A., Irwin, M., Kim, A. G., Knop, R. A., Lidman, C., McMahon, R., Mendez, J., Nobili, S., Nugent, P. E., Pain, R., Panagia, N., Pennypacker, C. R., Perlmutter, S., Quimby, R., Raux, J., Regnault, N., Ruiz-Lapuente, P., Schaefer, B., Schahmaneche, K., Spadafora, A. L., Walton, N. A., Wang, L., Wood-Vasey, W. M., Yasuda, N.
The Hubble diagram of type Ia supernovae as a function of host galaxy morphology,
MNRAS, 340, 1057 (2003).

C. Blanc, G., Afonso, C., Alard, C., Albert, J.N. Aldering, G., Amadon, A., Andersen, J., Ansari, R., Aubourg, É., Balland, C., Bareyre, P., Beaulieu, J. P., Charlot, X., Conley, A., Coutures, C., Dahlén, T., Dereu, F., Fan, X., Ferlet, R., Folatelli, G., Fouqué, P., Garavini, G., Glicenstein, J. F., Goldman, B., Goobar, A., Gould, A., Graff, D., Gros, M., Haissinski, J., Hamadache, C., Hardin, D., Hook, I. M., de Kat, J., Kent, S., Kim, A., Lasserre, T. Le Guillou, L. Lesquoy, É, Loup, C., Magneville, C., Marquette, J. B., Maurice, É, Maury, A., Milsztajn, A., Moniez, M., Mouchet, M., Newberg, H., Nobili, S., Palanque-Delabrouille, N., Perdereau, O., Prévot, L., Rahal, Y. R., Regnault, N., Rich, J., Ruiz-Lapuente, P., Spiro, M., Tisserand, P., Vidal-Madjar, A., Vigroux, L., Walton, N. A., Zylberajch, S.
Type Ia supernova rate at redshift of $\sim$ 0.1,
A&A, submitted.

D. Benetti, S., Meikle, P., Stehle, M., Altavilla, G., Desidera, S., Folatelli, G., Goobar, A., Mattila, S., Mendez, J., Navasardyan, H., Pastorello, A.,

Patat, F., Riello, M., Ruiz-Lapuente, P., Tsvetkov, D., Turatto, M., Mazzali, P., Hillebrandt, W.
Supernova 2002bo: inadequacy of the single parameter description.
MNRAS (2004) 348, 261–278

E. Folatelli, G.
Spectral homogeneity of type Ia supernovae,
New Astronomy Reviews (2004), in press.

F. S. Nobili, R. Amanullah, G. Garavini, A. Goobar, C. Lidman, V. Stanishev, G. Aldering, P. Astier, G. Blanc, M. S. Burns, A. Conley, S. E. Deustua, M. Doi, R. Ellis, S. Fabbro, A. S. Fruchter, G. Folatelli, S. Garmond, K. Garton, R. Gibbons, G. Goldhaber, D. E. Groom, D. Hardin, I. Hook, D. A. Howell, A. G. Kim, R. A. Knop, B. C. Lee, J. Mendez, P. E. Nugent, R. Pain, N. Panagia, C. R. Pennypacker S. Perlmutter, R. Quimby, J. Raux, N. Regnault, P. Ruiz-Lapuente, G. Sainton, B. Schaefer, K. Schahmaneche, E. Smith, A. L. Spadafora, M. Sullivan, N. A. Walton, L. Wang, W. M. Wood-Vasey, N. Yasuda
(THE SUPERNOVA COSMOLOGY PROJECT).
Restframe I-band Hubble diagram for Type Ia supernovae up to $z \sim 0.5$,
to be submitted.

G. C. Lidman, D. A. Howell, G. Folatelli, G. Garavini, S. Nobili, G. Aldering, R. Amanullah, P. Astier, C. Balland, G. Blanc, M. S. Burns, A. Conley, T. Dahlén, S. E. Deustua, R. Ellis, S. Fabbro, X. Fan, B. Frye, E. L. Gates, R. Gibbons, G. Goldhaber, B. Goldman, A. Goobar, D. E. Groom, D. Hardin, I. Hook, D. Kasen, S. Kent, A. G. Kim, R. A. Knop, B. C. Lee, J. Mendez, G. Miller, M. Moniez, M. Mouchet, A. Mourão, H. Newberg, P. E. Nugent, R. Pain, N. Panagia, O. Perdereau, S. Perlmutter, V. Prasad, R. Quimby, J. Raux, N. Regnault, J. Rich, G. T. Richards, P. Ruiz-Lapuente, G. Sainton, B. Schaefer, K. Schahmaneche, E. Smith, A. L. Spadafora, V. Stanishev, N. A. Walton, L. Wang, W. M. Wood-Vasey, N. Yasuda, T. York
(THE SUPERNOVA COSMOLOGY PROJECT).
Spectroscopic confirmation of high-redshift supernovae with ESO VLT,
in preparation.

H. G. Garavini, G. Aldering, A. Amadon, R. Amanullah, P. Astier, C. Balland, G. Blanc, M. S. Burns, A. Conley, T. Dahlén, S. E. Deustua, R. Ellis, S. Fabbro, X. Fan, G. Folatelli, B. Frye, E. L. Gates, R. Gibbons, G. Goldhaber, B. Goldman, A. Goobar, D. E. Groom, J. Haissinski, D. Hardin, I. M. Hook, D. A. Howell, D. Kasen, S. Kent, A. G. Kim, R. A. Knop, B. C. Lee, C. Lidman, J. Mendez, G. J. Miller, M. Moniez, A. Mourão, H. Newberg, S. Nobili, P. E. Nugent, R. Pain, O. Perdereau, S. Perlmutter, V. Prasad, R. Quimby, J. Raux, N. Regnault, J. Rich, G. T. Richards,

P. Ruiz-Lapuente, G. Sainton, B. E. Schaefer, K. Schahmaneche, E. Smith, A. L. Spadafora V. Stanishev, N. A. Walton, L. Wang, W. M. Wood-Vasey (THE SUPERNOVA COSMOLOGY PROJECT).
SN 1999ac: On the presence of high velocity carbon,
to be submitted.

Acronyms

2dFGRS	2-degree Field Galaxy Redshift Survey
APO	Apache Point Observatory
BCG	Bright cluster galaxies
CCD	Charge coupled device
CFHT	Canada-France-Hawaii Telescope
CMBR	Cosmic microwave background radiation
CTIO	Cerro Tololo Inter-American Observatory
DAR	Differential atmospheric refraction
EROS	Extremely Red Object Survey
ESO	European Southern Observatory
ESSENCE	Equation of State: SupErNovae trace Cosmic Expansion
EVM	Effective variance method
EW	Equivalent width
FLRW	Friedmann-Lemaître-Robertson-Walker
FWHM	Full-width-half-maximum
HST	Hubble Space Telescope
HZSNS	High-Z Supernova Search
IAU	International Astronomical Union
IDL	Interactive Data Language
IGM	Inter-galactic medium
IRAF	Image Reduction and Analysis Facility
KPNO	Kitt Peak National Observatory
MLCS	Multi-Color Lightcurve Shape
NEAT	Near-Earth Asteroid Tracking
NED	NASA/IPAC Extragalactic Database
NOT	Nordic Optical Telescope
QUEST	Quasar Equatorial Survey Team
r.m.s.	Root-mean-square
RW	Robertson-Walker
SCP	Supernova Cosmology Project
SN(e)	Supernova(e)
SN(e) Ia/Ib/Ic/II	Type Ia/Ib/Ic/II supernova(e)
SNAP	Supernova / Acceleration Probe
SNLS	Supernova Legacy Survey
VLT	Very Large Telescope
WMAP	Wilkinson Microwave Anisotropy Probe

Acknowledgements

There are many people to whom I am thankful for having helped me in various ways during these years. I would like to mention in particular only a few of them.

My supervisor, Ariel Goobar, whose guiding and teaching were continuously inspiring and who provided me with valuable support, both from the professional viewpoint and through his friendliness.

Christopher Lidman, who taught me some of his observational skills and was always supportive and encouraging about my research. I had the chance to share with him some of the most exciting moments of my career, when "fishing" supernovae with the VLT.

My colleague Vallery Stanishev, who carefully read parts of the manuscript and provided me with suggestions and ideas.

My fellow, Rahman Amanullah, whose computing skills saved me from disaster in many an occasion.

And finally, my former supervisor in Argentina, Nidia Morrell, who made it possible in many ways that I could become an astronomer and eventually come to Sweden, and to whom I might have not expressed all my gratitude yet.

Contents

1 Introduction **1**
- 1.1 Cosmology 1
- 1.2 This Thesis 3

2 The Standard Model of Cosmology **5**
- 2.1 A Homogeneous and Isotropic Universe 5
- 2.2 The Cosmological Parameters 6
- 2.3 The Distance–Redshift Relation 8
- 2.4 Cosmological Constant and Accelerated Expansion 12

3 Cosmological Parameters from Type Ia Supernovae **17**
- 3.1 Type Ia Supernovae as Standardized Candles 17
- 3.2 Supernova Searches 23
- 3.3 Results: The Accelerating Universe 25
- 3.4 Measurements of Dark Energy 39
- 3.5 Systematic Uncertainties 41

4 Observation of Type Ia Supernova Spectra **47**
- 4.1 The Spring 1999 Nearby Supernova Campaign 47
- 4.2 High-Redshift Supernova Spectroscopy with the VLT 70

5 Analysis of Type Ia Supernova Spectra **93**
- 5.1 Spectra: The Hidden Face of Supernovae 93
- 5.2 Newly Defined Spectral Measurements (EW) 102
- 5.3 Low- and High-Redshift Supernovae 113

6 Summary **123**

Chapter 1

Introduction

1.1 Cosmology

Cosmology is the branch of science that studies the structure and evolution of the Universe as a whole. Since the beginning of history, this has been a topic of special interest for the different cultures. Our view of the Universe has changed through the centuries as science developed. In the present, we know the Earth is a planet that orbits a star, the Sun, which in turn travels its orbit in a system formed by about 100 billion stars, our galaxy, the Milky Way. The Milky Way is one in billions of galaxies that form the large-scale structure of the observable Universe. Studying the gravitational effects on the observable matter, we have gathered evidence that there is a large fraction of matter in the Universe which we cannot directly observe, the so-called *dark matter*. Assessing the nature of these components is a main goal of cosmology.

In the present time, cosmology is based on Einstein's theory of general relativity. This theory provides the basic mathematical tools to state the dynamics of physical systems in a relativistic frame, where the classical Newtonian formulation fails. Einstein brilliantly accomplished the generalization of Newton's laws of gravitation, and at the same time provided the interpretation of matter as the source of space-time curvature.

The Universe viewed on large scales —the physical system to which the laws of general relativity are applied in cosmology— is modeled as a homogeneous and isotropically distributed perfect fluid. In the 1920s, Friedmann and Lemaître independently found that Einstein's equations, when applied to a cosmic fluid composed of ordinary matter, would only yield non-static solutions. This was contrary to the paradigm of the time by which the Universe was believed to be static. Einstein therefore introduced an additional term in his equations, a constant term, defined by the *cosmological constant* Λ, which had to be fine-tuned to compensate the effect of gravity and thus yield a static solution. It was a few years later that Hubble surveyed the distances and recession velocities of

galaxies and arrived at a surprising result: the further the galaxy, the faster it receded from the Earth. The Universe appeared to be indeed expanding and thus non-static! The need for a cosmological constant seemed to be ruled out, and Einstein is said to have regretted having ever introduced it. However, this ad hoc term was not forbidden by any physical principle and the "ghost" of the cosmological constant survived the decades.

The discovery of the expansion of the Universe by Hubble set the foundations of what currently is the standard model of cosmology, that is the *Hot Big Bang model*. According to this model, the Universe is not infinitely old but came to existence about 10 billion years ago, in a state which after a small fraction of a second was extremely compressed and hot, and has been expanding and cooling since then. Further evidence supporting this model has been gathered from different observations. For instance, the detection in all directions of the sky of the cosmic microwave background radiation (CMBR), which is predicted as the relic from the first, very hot stages. Also, the relative abundances of light elements observed in the local Universe, which agree with what would be synthesized in an expanding and cooling model.

The most recent break-through in our understanding of the expansion history of the Universe happened in 1998 when two teams independently found strong evidence for a non-vanishing cosmological constant. These teams used type Ia supernovae to reproduce Hubble's experiment with much higher accuracy and to larger distances. The relative dimness of distant supernovae, compared to the case of a Universe composed of only ordinary matter, implies the existence of a non-zero Λ. Moreover, the cosmological constant term was found to dominate over ordinary matter, which, given the repulsive effect of Λ, means that the Universe is undergoing a phase of *accelerated* expansion. These results are supported by other recent experiments. Firstly, measurements of the fluctuations in the CMBR indicate that the geometry of the Universe is flat; secondly, studies of the large-scale distribution of galaxies and dynamics of galaxy clusters show that the amount of ordinary matter is about 30% of what is needed for the Universe to be flat. The cosmological constant would therefore provide the additional energy to produce the observed flatness.

Understanding the physical origin of the cosmological constant is one the greatest challenges of modern cosmology. From the point of view of particle physics, Λ can be related to a form of *vacuum energy* with equation-of-state parameter $w_{\rm vac} \equiv p_{\rm vac}/\rho_{\rm vac} = -1$. However, nothing prevents the equation-of-state parameter of this mysterious form of matter to be $\neq -1$ or to be a function of time. This gives rise to more general forms of *dark energy*, which can be tested with experiments such as the one of type Ia supernovae (e.g., in the future, using extremely accurate distance measurements obtained with the *Supernova / Acceleration Probe* satellite, SNAP). A full theoretical description of this form of matter probably has to wait for the development of a theory of quantum gravity.

1.2 This Thesis

The excitement produced by the result of an accelerated expansion of the Universe led to intensive research in the field of supernovae as astrophysical systems and as tools for cosmology. Because of this, our knowledge of the physical properties of supernovae has greatly developed during the last decade, although many aspects are still under active research. Additionally, as the amount and quality of the supernova data increases, the study of possible systematic effects becomes more and more important. Also crucial is the investigation of other processes than acceleration which have been suggested to explain the observed dimness of distant supernovae.

This thesis focuses on the observational aspects of supernovae, in particular on the quantitative analysis of their spectra, with the dual aim of shedding light on the physics of these objects and testing some of the possible systematic effects and proposed alternatives to acceleration.

Chapter 2 gives a brief introduction of the principles and mathematical formulation of the standard model of cosmology and the ways in which the parameters of the model can be obtained. Chapter 3 focuses on the use of type Ia supernovae to solve for the cosmological parameters. Chapter 4 describes the observational aspects and the spectroscopic data treatment in relation with low- and high-redshift supernovae discovered in campaigns in which I participated as a member of the *Supernova Cosmology Project* (SCP). Chapter 5 presents the power of spectroscopic data for investigating the properties of type Ia supernovae and testing possible systematic effects in their use as distance indicators. Special attention is given to the results of newly defined spectral measurements (named "EW") applied to the spectra of low- and high-redshift supernovae introduced Chapter 4. Finally, Chapter 6 provides a summary of the problems addressed and results found.

Four papers are included in this thesis, labeled as **I** – **IV**. **Paper I** presents the data treatment method described in Chapter 4. Apart from the reduction of the spectra, my main contribution to this work is in the development of the methods to carefully estimate uncertainties and host-galaxy flux contamination levels. I took charge of writing most of the text and coordinating the whole work. **Paper II** presents the analysis of the newly defined EW measurements applied to a large set of nearby supernovae, as described in Chapter 5. The measurement definition, application and subsequent analysis is my contribution to this paper, as well as the writing of the text. **Paper III** shows the detailed spectral analysis of the peculiar type Ia supernova `SN 1999aa`, observed by the SCP. I took part in the reduction of the spectra and in the discussions leading to the analysis presented in the paper. **Paper IV** presents the study of 14 high-quality spectra from 12 high-redshift type Ia supernovae observed with the *Very Large Telescope*. I participated in the observation and reduction of the spectra, and in the analysis of the results, in particular, the comparison of EW measurements with those of nearby supernovae, and the writing of the related

section.

Other papers in which I was involved are given as reference (see **Other Related Papers**). For some of them, I contributed to the discussions held by the authors during the preparation process (**Papers A, B** and **F**). In other cases, I also took part in the observations and data reduction (**Papers C, D, G** and **H**). **Paper E** is a contribution to the proceedings of the Workshop on *Supernovae and Dust* held in Paris, in May 2003, and can be considered as a preliminary version of **Paper II**.

Chapter 2

The Standard Model of Cosmology

2.1 A Homogeneous and Isotropic Universe

Modern cosmology is based on Einstein's general theory of relativity. In order to solve the fundamental equations of general relativity (*Einstein's equations*), a model has to be given for the matter distribution in the Universe. The simplest of such models was introduced by Friedmann and Lemaître and is that of a homogeneous and isotropic fluid. This means that, viewed on scales larger than the local concentrations of matter, the Universe presents an even density and looks the same in all directions. Recent observations have confirmed that the large-scale distribution of matter in the Universe is highly isotropic. Now, if we base ourselves on the *Copernican principle*, the fact the we observe an isotropic Universe should not be a peculiarity of our observing location (this is usually called the *cosmological principle*). This implies that the Universe should be isotropic about any point we would choose to observe from. Homogeneity is thus a consequence of this reasoning: isotropy about more than one point implies that the density should be even in the entire Universe.

The geometry of an isotropic and homogeneous Universe is greatly simplified due to the symmetries introduced. Its mathematical formulation in terms of comoving spherical coordinates r, θ and ϕ, and cosmological time t leads to the following metric:

$$ds^2 = dt^2 - a^2(t)\left(\frac{dr^2}{1-kr^2} + r^2 d\theta^2 + r^2 \sin^2\theta d\phi^2\right), \tag{2.1}$$

where we set the speed of light $c = 1$ and $a(t)$ is the time-dependent scale factor which converts comoving distances into physical distances. The constant curvature is given by the parameter k which takes the values $+1$, 0, or -1 depending

on whether the Universe is closed, flat, or open, respectively. This is called the *Robertson–Walker* metric (or RW metric, for short). The solution of Einstein's equations for a perfect cosmological fluid described by the RW metric gives rise to the *Standard Model* of cosmology, also called the Friedmann–Lemaître–Robertson–Walker model (FLRW).

Einstein's equations can be viewed as a representation of matter and energy as the sources of space-time curvature. By introducing the RW metric and considering the Universe to be a perfect, homogeneous fluid of energy density ρ, one obtains the equations that determine the dynamics of the cosmic fluid, i.e. the evolution of the scale parameter $a(t)$. One of these equations is the *Friedmann equation*,

$$H^2 \equiv \left(\frac{\dot{a}}{a}\right)^2 = \frac{8\pi G_{\rm N}}{3}\rho - \frac{k}{a^2}, \tag{2.2}$$

where $G_{\rm N}$ is Newton's constant of gravitation. We have introduced the definition of the *Hubble parameter*, H, which governs the expansion rate of the FLRW Universe. $H(t)$ is in turn determined by $\rho(t)$ and the value of the curvature k.

The Hubble Law

Let us consider the local Universe, where Euclidean geometry is valid. We define the *Hubble constant* by evaluating $H(t)$ at the present cosmic time t_0:

$$H_0 \equiv H(t_0). \tag{2.3}$$

In such a geometry the physical distance between two objects with comoving distance r would be $d = ar$. It is easy to see that the change in the scale factor a would introduce a relative velocity between the objects of $v = \dot{a}r$. We therefore obtain the so-called *Hubble law* for the local Universe:

$$v = H_0 d. \tag{2.4}$$

This is what Edwin Hubble set to measure in 1929. His result of a non-vanishing Hubble constant [31] modified dramatically the view of the Universe which until then was believed to be static.

2.2 The Cosmological Parameters

Our aim is to extend Hubble's result to larger distances, where the Euclidean approximation is no longer valid. We will therefore transform the Friedmann equation (2.2) by explicitly introducing a set of *cosmological parameters* related to the energy density ρ in the FLRW model (see a more thorough derivation in [7]). Specifying the values of those parameters would thus determine the expansion history of the Universe.

Let us start by defining the *critical density* ρ_c of the cosmic fluid as

$$\rho_c \equiv \frac{3H^2}{8\pi G_{\rm N}}, \tag{2.5}$$

and the *density parameter* Ω as the ratio of density to critical density:

$$\Omega \equiv \frac{\rho}{\rho_c}. \tag{2.6}$$

Then Eqn. 2.2 can be rewritten as

$$\frac{k}{H^2 a^2} = \Omega - 1. \tag{2.7}$$

This means that the curvature of the Universe is solely determined by the value of Ω. If $\Omega > 1$, the Universe is closed. If $\Omega < 1$, the Universe is open. An exact value of $\Omega = 1$ would mean that the Universe is flat.

It is customary to simplify the physical interpretation of the Friedmann equation by specifying different components of the cosmic fluid. For instance, by writing

$$\rho = \rho_M + \rho_R + \rho_\Lambda, \tag{2.8}$$

where ρ_M and ρ_R are the contributions from non-relativistic matter and radiation, respectively, and ρ_Λ is the energy density of vacuum. The latter contribution emerges when a constant term, proportional to the *cosmological constant* Λ, is introduced in Eisntein's equations. Such a term can be viewed in terms of an energy density defined as

$$\rho_\Lambda \equiv \frac{\Lambda}{8\pi G_{\rm N}}. \tag{2.9}$$

Each of the components in the cosmic fluid is described by an equation of state which relates the energy density ρ with the pressure p. For a perfect fluid, this equation of state has the form $p = w\rho$, with some constant w. For the three components introduced, it is found that

$$\begin{cases} w_M &= 0 \\ w_R &= 1/3 \\ w_\Lambda &= -1 \end{cases}. \tag{2.10}$$

The problem is further simplified if we consider the FLRW model at the present era in the history of the Universe, when the contribution from radiation to the energy density is negligible in comparison with the contribution from matter. In such scenario, the total density can be written as

$$\rho = \rho_M + \rho_\Lambda. \tag{2.11}$$

For each of these components there is a simple dependence of ρ on the scale factor a. In the case of stable matter, there is no creation or destruction of particles and therefore the amount of matter inside a given comoving volume will be constant. This means that as the Universe expands, matter dilutes as

$$\rho_M \propto a^{-3}. \tag{2.12}$$

For a cosmological constant, by definition the energy density does not change, thus

$$\rho_\Lambda \propto const. \tag{2.13}$$

It is also useful to separate the same two components in the density parameter, evaluated at the present time t_0

$$\Omega_0 \equiv \Omega(t_0) = \Omega_M + \Omega_\Lambda, \tag{2.14}$$

where the *cosmological parameters* at present Ω_M and Ω_Λ are defined as

$$\begin{cases} \Omega_M & \equiv & \left(\frac{8\pi G_N}{3H_0^2}\right)\rho_0 \\ \Omega_\Lambda & \equiv & \frac{\Lambda}{3H_0^2} \end{cases}, \tag{2.15}$$

with $\rho_0 \equiv \rho_M(t_0)$, the matter density today. Using these definitions and the dependence of ρ on a (Eqns. 2.12 and 2.13), Eqn. 2.2 can be rewritten as

$$H^2 = H_0^2 \left[\Omega_\Lambda + \Omega_M \left(\frac{a}{a_0}\right)^{-3} - (\Omega_0 - 1)\left(\frac{a}{a_0}\right)^{-2}\right], \tag{2.16}$$

where $a_0 \equiv a(t_0)$ is the value of the scale factor today.

2.3 The Distance–Redshift Relation

We have found an expression (Eqn. 2.16) for the dependence of the Hubble parameter on time – through $a(t)$ – in terms of the cosmological parameters that define the FLRW model (H_0, Ω_M, and Ω_Λ). One way to solve for the cosmological parameters is to connect $H(t)$ with observable quantities, in the same manner that Hubble did for the local Universe using recession velocities and distances. In the case of the distant Universe, we need to introduce two important observables, namely the *redshift* and the *luminosity distance*.

Redshift

When observing an event occurring at cosmological distances it is not possible to directly measure the time t of its occurrance or the amount by which the Universe

expanded since that time $(a(t)/a_0)$. The quantity to be observed instead is the redshift z, defined by

$$1 + z \equiv \frac{\nu_e}{\nu_o}, \tag{2.17}$$

where ν_e is the frequency emited by the object and ν_o is the one observed. In modern observational astrophysics, it is straight-forward to measure the redshift for example, in terms of spectral lines. All we need to do is to identify a certain line in the spectrum of the observed object and compare the frequency we observe it at with its actual frequency, measured in the laboratory.

Let us now find the relation between redshift z and the scale factor a for the FLRW Universe. Consider a source at a comoving distance r_e from Earth that emits a photon at a time t_e which reaches the observer at a time t_o. Since photons follow light-like geodesics ($ds^2 = 0$), and we can choose coordinates such that $d\theta = d\phi = 0$, we find from the RW metric in Eqn. 2.1 that

$$\int_0^{r_e} \frac{dr}{\sqrt{1 - kr^2}} = \int_{t_e}^{t_o} \frac{dt}{a(t)}. \tag{2.18}$$

The left-hand side is a comoving quantity for a given source and is thus constant. If we now think of photons being emited at intervals δt_e and recieved at intervals δt_o, the condition that integral on the right-hand-side of Eqn. 2.18 should also be constant implies that $\delta t_e/\delta t_o = a(t_e)/a(t_o)$. In terms of the frequency (the number of wave crests per unit time) this means $\nu_e/\nu_o = a(t_o)/a(t_e)$ and therefore, using the definition of redshift we find,

$$1 + z = \frac{a(t_o)}{a(t_e)}. \tag{2.19}$$

We can now rewrite Eqn. 2.16 in terms of the redshift:

$$H^2 = H_0^2 \left[\Omega_\Lambda + \Omega_M (1+z)^3 - (\Omega_0 - 1)(1+z)^2\right]. \tag{2.20}$$

Using $\Omega_0 = \Omega_M + \Omega_\Lambda$, this becomes

$$H^2 = H_0^2 \left[(1+z)^2(1 + \Omega_M z) - z(2+z)\Omega_\Lambda\right]. \tag{2.21}$$

Let us now derive the relation between cosmic time t and redshift z. From the definition of the Hubble parameter

$$H = \left(\frac{\dot{a}}{a}\right) = \frac{d}{dt}\log\left(\frac{a(t)}{a_0}\right) = \frac{d}{dt}\log\left(\frac{1}{1+z}\right) = \frac{-1}{1+z}\frac{dz}{dt}. \tag{2.22}$$

Introducing this result in Eqn. 2.21, we obtain

$$\frac{dt}{dz} = -H_0^{-1}(1+z)^{-1}\left[(1+z)^2(1+\Omega_M z) - z(2+z)\Omega_\Lambda\right]^{-\frac{1}{2}}, \tag{2.23}$$

which provides the means to transform times into redshifts in the FLRW model.

Luminosity Distance

As the final step in solving for the cosmological parameters, we introduce the relation between distance measures and the Hubble parameter. In general, measuring accurate distances is one the most troublesome tasks of the astronomer. The ideal case is that of a *standard candle*, an object of known intrinsic brightness, whose distance is easily determined by the measured brightness through an inverse-square law. In Chapter 3 we will study in detail the properties of type Ia supernovae as the best standard candle found to the date.

Consider a source of which we know the luminosity L, located at a comoving distance r from Earth. Suppose that at a time t_e, the source emits isotropically a certain amount of photons. A telescope of area A located on Earth would detect a fraction $A/4\pi(a_0 r)^2$ of those photons. If each photon was emited with energy $h\nu_e$, it would arrive at the observer with energy $h\nu_0 = h\nu_e/(1+z)$. Also, if the photons were emited during a time interval δt_e, they would be recieved during an interval $\delta t_0 = (1+z)\delta t_e$. Therefore, the measured flux F of the source, given by the number of photons detected per unit time and unit area multiplied by the energy of each photon, would be

$$F = \frac{L}{4\pi(a_0 r(1+z))^2}. \tag{2.24}$$

We can assimilate this expression to an inverse-square law by defining the luminosity distance to the source as

$$d_L \equiv a_0 r(1+z). \tag{2.25}$$

The connection between the luminosity distance and the FLRW model is embedded in the comoving distance r. We have seen that Eqn. 2.18 is valid for photons traveling from the source to the observer (now $r_e \equiv r$, $t_e \equiv t$, and $t_o \equiv t_0$). Multiplying that equation by a_0 and using Eqn. 2.19, we obtain

$$a_0 \int_0^r \frac{dr'}{\sqrt{1-kr'^2}} = \int_t^{t_0} (1+z)dt'. \tag{2.26}$$

Using Eqn. 2.23 to change variables from t to z, we find

$$a_0 \int_0^r \frac{dr}{\sqrt{1-kr'^2}} = H_0^{-1} \int_0^z G(z)dz, \tag{2.27}$$

where we have defined the function

$$G(z) \equiv \left[(1+z)^2(1+\Omega_M z) - z(2+z)\Omega_\Lambda\right]^{-\frac{1}{2}}. \tag{2.28}$$

The integral on the left-hand side of Eqn. 2.27 has different solutions depending on the value of k:

$$\begin{cases} \frac{\arcsin(r\sqrt{k})}{\sqrt{k}} & \text{for } k=1 \\ r & \text{for } k=0 \\ \frac{\operatorname{arcsinh}(r\sqrt{-k})}{\sqrt{-k}} & \text{for } k=-1 \end{cases} . \tag{2.29}$$

By inverting the solutions above, we can obtain an expression for r as a function of z, as required by Eqn. 2.25.

Finally, introducing the definition of the total density parameter at t_0 (Eqn. 2.7) $k/H_0^2 a_0^2 = \Omega_0 - 1$, we arrive at the desired luminosity distance–redshift relation in terms of the cosmological parameters:

$$d_L(z; H_0, \Omega_M, \Omega_\Lambda) = \frac{(1+z)}{H_0\sqrt{|\Omega_0 - 1|}} \mathcal{S}_k\left(\sqrt{|\Omega_0 - 1|}\int_0^z G(z)dz\right), \tag{2.30}$$

where we have introduced the function

$$\mathcal{S}_k(x) \equiv \begin{cases} \sin(x) & \text{for } k=1 \\ x & \text{for } k=0 \\ \sinh(x) & \text{for } k=-1 \end{cases} . \tag{2.31}$$

The factors $\sqrt{|\Omega_0 - 1|}$ cancel each other in the case of a flat Universe ($k = 0$ and $\Omega_0 = 1$).

Going back to the question of observing a standard candle of luminosity L, we would like to explicitly introduce this quantity and its related observable F in our formulae. In optical astronomy, it is customary to express luminosities in logarithmic scale by defining a *magnitude* system. If the observations are carried out through a filter f with transmition function $T_f(\nu)$, the apparent magnitude is defined as

$$m_f \equiv -2.5 \log\left(\int_0^\infty T_f(\nu)F(\nu)d\nu\right) + C_f, \tag{2.32}$$

where C_f is a constant that sets the scale of the magnitude system for that filter. The minus sign in the definition implies that magnitudes are *lower* for brighter objects. Luminosities are given in this system as *absolute magnitudes* M_f, defined as the apparent magnitude that the object would have if it were located at a distance of 10 pc from the observer. For an object at a distance d, expressed in Mpc, $m_f = M_f + 5\log d + 25$. Using the luminosity distance (given in Mpc), we obtain the relation between the apparent magnitudes of a standard candle and its redshift (for simplicity, we drop the filter subscript)

$$m(z) = M + 5\log d_L(z; H_0, \Omega_M, \Omega_\Lambda) + 25. \tag{2.33}$$

Since m and z are directly measurable from astronomical data, this expression is useful in solving for the cosmological parameters. The problem reduces then to

measuring the apparent magnitudes of standard candles as a function of redshift, which yields the *Hubble diagram*, and then fitting the cosmological parameters to the data.

Figure 2.1 shows the predicted apparent magnitude of a standard candle in different cosmological scenarios, compared to the case of an empty Universe $(\Omega_M, \Omega_\Lambda) = (0, 0)$. In models with non-zero matter densities and no cosmological constant the standard candles appear brighter than in an empty Universe due to the decelerated expansion caused by gravity. On the other hand, if a cosmological constant term dominates, the standard candles appear dimmer because of the accelerated expansion. A mixture of matter and cosmological constant produces a family of solutions in between. In particular, in the case of $(\Omega_M, \Omega_\Lambda) = (0.3, 0.7)$ (the *concordance model*, see Chapter 3), the objects look dimmer in the local Universe up to $z \sim 1.3$. Further back in cosmic time (greater z) matter begins to dominate, as is clear from Eqns. 2.12 and 2.13, and the objects appear brighter than in an empty Universe. Figure 2.1, produced using the simulation package `SNOC` [19], provides an idea of the accuracy at which the standard candles need be observed in order to distinguish between the different models.

In Chapter 3 we will discuss the use of type Ia supernovae as standard candles and the implications of the resulting cosmological parameters.

2.4 Cosmological Constant and Accelerated Expansion

We now study the role of matter and vacuum energy in the determination of the acceleration of the scale factor ($\ddot{a}$). An additional component of Einstein's equations, in the case of the FLRW Universe, becomes

$$\frac{2\ddot{a}}{a} + \left(\frac{\dot{a}}{a}\right)^2 + \frac{k}{a^2} = -8\pi G_{\rm N} p. \tag{2.34}$$

Subtracting this equation to the Friedmann equation (Eqn. 2.2), gives

$$\frac{\ddot{a}}{a} = -\frac{4\pi G_{\rm N}}{3}(\rho + 3p). \tag{2.35}$$

Introducing the two components of ρ from Eqn. 2.11, and their equations of state, we obtain

$$\frac{\ddot{a}}{a} = -\frac{4\pi G_{\rm N}}{3}(\rho_M - 2\rho_\Lambda). \tag{2.36}$$

We can see that, while matter tends to decelerate the expansion (as expected from the attractive nature of gravity), a positive vacuum energy accelerates the expansion. In terms of the cosmological density parameters, the condition for an *accelerated* expansion of the Universe at the present time is

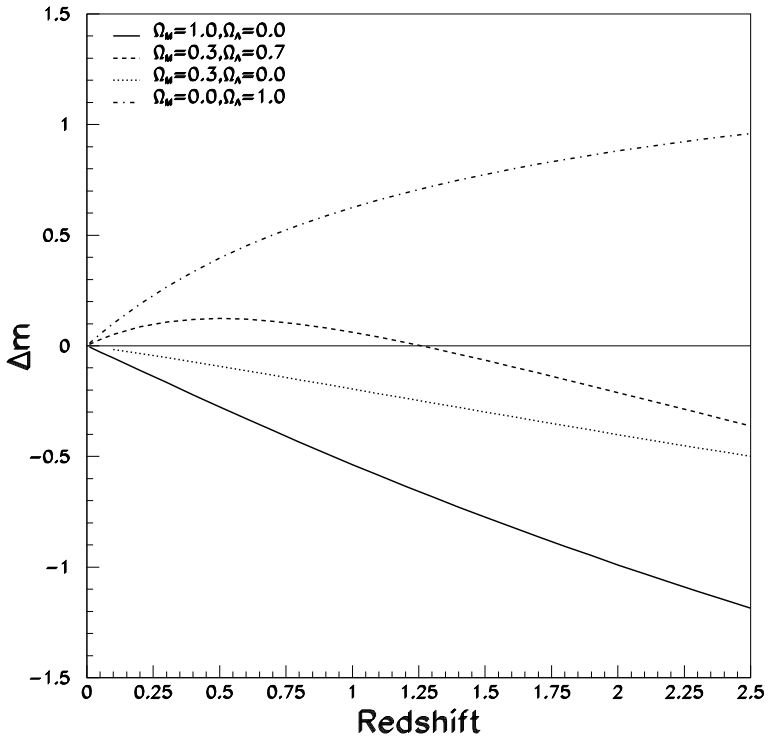

Figure 2.1: The residual Hubble diagrams for a series of cosmological models compared to the case of an empty Universe $(\Omega_M, \Omega_\Lambda) = (0, 0)$. The cases shown correspond to some standard solutions for the cosmological parameters: a flat, matter-only Universe $(\Omega_M, \Omega_\Lambda) = (1, 0)$; an open Universe with no cosmological constant $(\Omega_M, \Omega_\Lambda) = (0.3, 0)$; a flat, Λ-dominated Universe $(\Omega_M, \Omega_\Lambda) = (0.3, 0.7)$; and a flat Universe with only cosmological constant $(\Omega_M, \Omega_\Lambda) = (0, 1)$.

$$\Omega_\Lambda > 2\Omega_M. \tag{2.37}$$

Dark Energy

Nothing prevents us from modifying the cosmological constant term in Einstein's equations by changing the form of its equation of state. This unknown form of energy, called *dark energy*, can be given a general equation of state

$$p_X = w_X \rho_X, \tag{2.38}$$

with w_X not necessarily equal to -1. In the most general case, w_X can depend on the cosmological time t. Reproducing the analysis that leads to Eqn. 2.35, we can see that the condition for an accelerated expansion is (at any time t)

$$\rho_M + \rho_X(1 + 3w_X) < 0. \tag{2.39}$$

In the case of a Universe without matter, this condition reduces to

$$w_X < -\frac{1}{3}. \tag{2.40}$$

For any species with equation of state $p = w\rho$, Einstein's equations yield a general dependence of the density ρ on the scale factor which is

$$\rho \propto a^{-3(1+w)}. \tag{2.41}$$

Using Eqn. 2.41 and defining the density parameter for dark energy as

$$\Omega_X \equiv \left(\frac{8\pi G_{\rm N}}{3H_0^2}\right)\rho_X(t_0), \tag{2.42}$$

the luminosity distance for the FLRW Universe can be rewritten from Eqn. 2.30, by modifying the expression of $G(z)$ to

$$G(z) = \left[g(z)\Omega_X + (1+z)^3\Omega_M - (1+z)^2(\Omega_0 - 1)\right]^{-\frac{1}{2}}, \tag{2.43}$$

where $\Omega_0 = \Omega_M + \Omega_X$ is the total density parameter at the present time, as in Eqn. 2.14, and $g(z)$ is given by

$$g(z) = \exp\left(3\int_0^z \frac{1 + w_X(z')}{1+z'}dz'\right). \tag{2.44}$$

Assuming that w_X has a simple dependence on z, the luminosity distance can be expressed in terms of the Hubble parameter H_0, the density parameters Ω_M and Ω_X, and the parameters defining $w_X(z)$. In practice, w_X is usually considered to be constant or to have a linear dependence on z. The modified expression of the luminosity distance can be introduced in the magnitude–redshift relation (Eqn 2.33), and values of the parameters can be solved from the measurement

of the Hubble diagram for some standard candle. Figure 2.2 shows the theoretical Hubble diagrams for different forms of the equation-of-state parameter in the case of a flat Universe with $\Omega_X = 0.7$, compared with an empty Universe $(\Omega_M, w_X) = (0, 0)$. It can be seen from the graph that solving for w_X requires higher precision in the measurements, especially if the possible dependence of w_X on z is to be established. Solving for w_X would lead to a better understanding of the nature of dark energy. The most recent attempts to measure w_X, assumed constant, using type Ia supernovae as standard candles are described in Chapter 3.

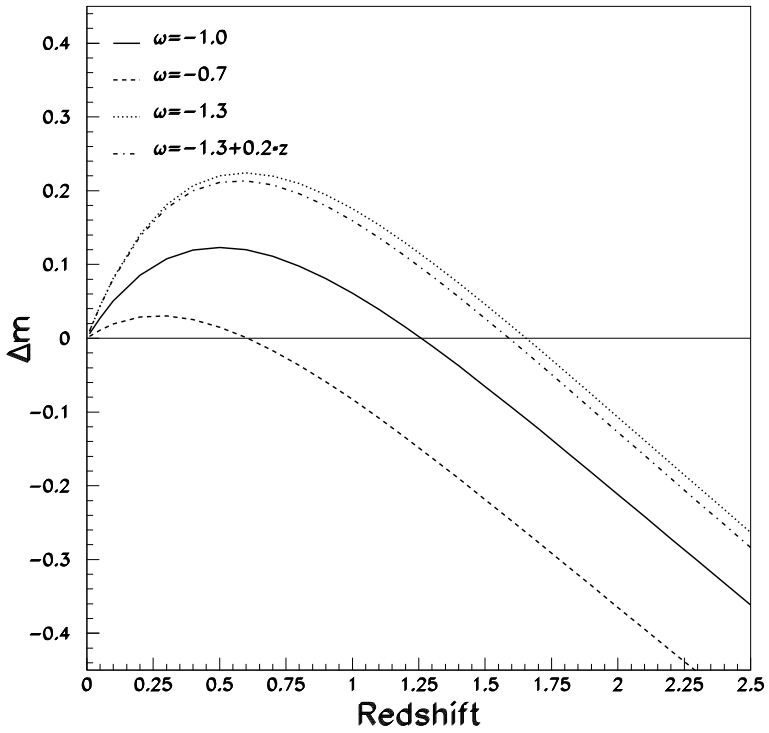

Figure 2.2: The theoretical Hubble diagram for a flat Universe with $(\Omega_M, \Omega_X) = (0.3, 0.7)$ and different values of the equation-of-state parameter w_X, compared to the empty Universe model $(\Omega_M, \Omega_X) = (0, 0)$.

Chapter 3

Cosmological Parameters from Type Ia Supernovae

3.1 Type Ia Supernovae as Standardized Candles

The search for a suitable standard candle to use in the measurement of the expansion history of the Universe has motivated a large amount of effort in the scientific community since the pioneering work by Hubble [31] was published. The characteristics sought for the ideal standard candle to be used in cosmology are the following:

1. Homogeneity. To allow a precise calibration of the luminosity and thus, of the distance measurements.

2. High luminosity. To be observable in the distant Universe.

3. Ubiquity. To be detectable both in the local and distant Universe.

Among the many classes of objects proposed as standard candles, only a few were proven to fulfill the three requirements given above.

The first attempts used the brightest objects known at the time, namely bright galaxies (called "extragalactic nebulae" in the vocabulary of the epoch). The technique was refined with the use of the brightest cluster galaxies (BCG), which could be calibrated to show a dispersion of 0.25 mag in luminosity [69]. However, it was later realized that the evolution in the properties of these objects as a function of redshift posed serious limitations to their use as distance indicators for cosmology (See, e.g., [70]).

During the last decades, supernovae (SNe) have been successfully used as extragalactic distance indicators. Several approaches at the measurement of

distances with SNe of different types have been developed (e.g., see [36]). In the following, the use of type Ia supernovae (SNe Ia) in particular will be treated. A short description of the classification of SNe in different types is therefore needed.

Classification of Supernovae

The classification of SNe has evolved parallel to our knowledge about these objects. The first stages in the development of the classification were based on observational characteristics. An understanding of the physical processes involved in SN events came much later. As a consequence, the classification currently used suffers from a certain degree of incompleteness, and, from a physical point of view, the nomenclature is confusing. The definition of SN types is mainly based on the properties of optical spectra at early stages in the evolution and, to some extent, on lightcurve characteristics.

It was Minkowski in 1941 [46] who first identified two distinct SN families, based on the presence or absence of hydrogen features in the spectra. He defined SNe of type I (SN I) as those which show no H lines, as opposed to SNe of type II (SN II), which clearly show H lines (in particular, H_α and H_β are very noticeable in optical spectra of SNe II). SNe I were recognized instead by a strong absorption at ~6150 Å, later identified as Si II λ6355, at a velocity of ~10000 km/s.

Through the years, a growing amount of "peculiar" SNe I, which did not show Si II λ6355, was discovered. In the mid-1980s it was realized that those SNe I formed a distinct family. Then, "normal" SNe I were renamed as type Ia, and the "peculiar" SNe I were divided into type Ib, which show He I lines, and type Ic, which lack He I. These two subtypes are less clearly distinguishable and are also referred to as SNe Ib/c. At the same time, a physical interpretation of the differences among the SN types began to appear. Both SNe Ib/c and SNe II are massive stars that undergo core collapse [81] (for SNe Ib/c, this happens after the H-rich envelopes are lost), whereas SNe Ia are the result of a thermonuclear explosion of a white dwarf star in a binary system [80, 47, 32, 54]. Figure 3.1 shows the typical spectra of SNe of types Ia, Ib, Ic and II, observed around maximum light, three weeks after, and one year after. The most prominent spectral features are marked. The following is a diagram of the spectroscopy-based classification of the four main SN types:

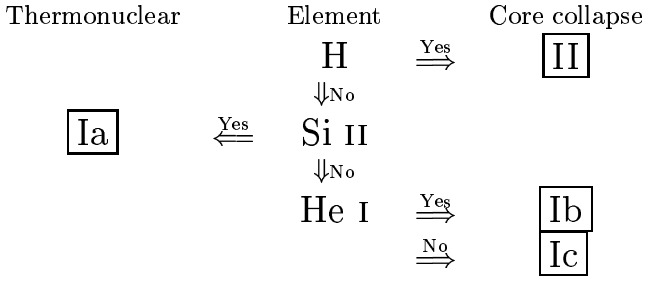

The classification of SNe II was also refined, according to the lightcurve properties, giving rise to type IIP and type IIL SNe. Other spectroscopically peculiar SNe II were also grouped in type IIn and type IIb.

Based on spectral characteristics, two subtypes of peculiar SNe Ia were identified. These are grouped according to their prototypes `SN 1991T` and `SN 1991bg`. Before maximum light, the spectra of `1991T`-like SNe show weak Si II λ6355 and other intermediate-mass element lines. After maximum light, these peculiarities become progressively less noticeable. The group of `1991bg`-like SNe show strong Ti II lines which persist long after maximum light. The latter SNe are found to be $\sim$2 to 3 magnitudes fainter and significantly redder than the average SNe Ia. Spectroscopically normal SNe Ia are also called "Branch normal", in reference to the work of Branch et al. [12]. Figure 3.2 shows the near-maximum light spectra of the normal `SN 1989B` and the peculiar prototypes `SN 1991T` and `SN 1991bg`, with the ions responsible for the most prominent features marked. Chapter 5 is dedicated to the detailed study of SN Ia spectroscopic properties.

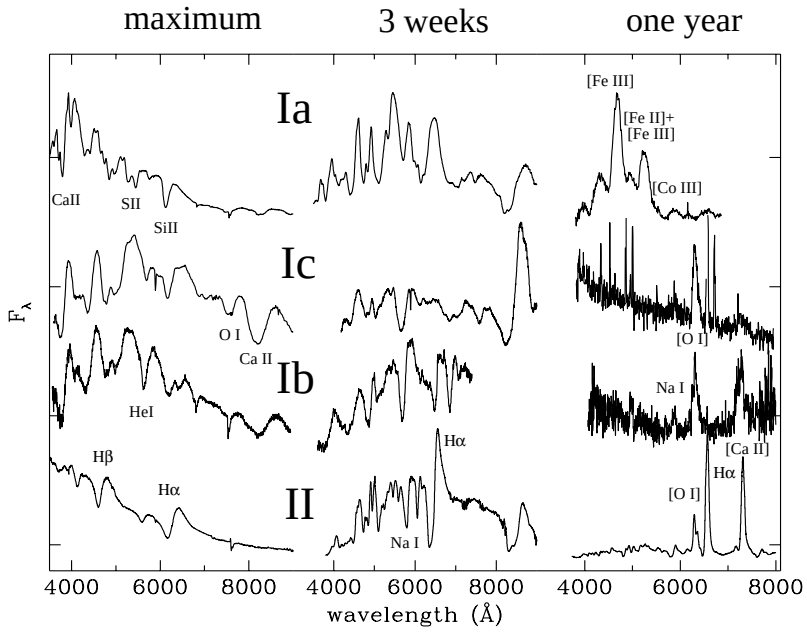

Figure 3.1: Spectra of supernovae of the four main types. On the left-hand side, the spectra at maximum light are most commonly used for classification. Also shown are examples of spectra obtained three weeks (middle), and around one year after maximum light (right-hand side). The ions responsible for the most prominent features are marked. Credit [77].

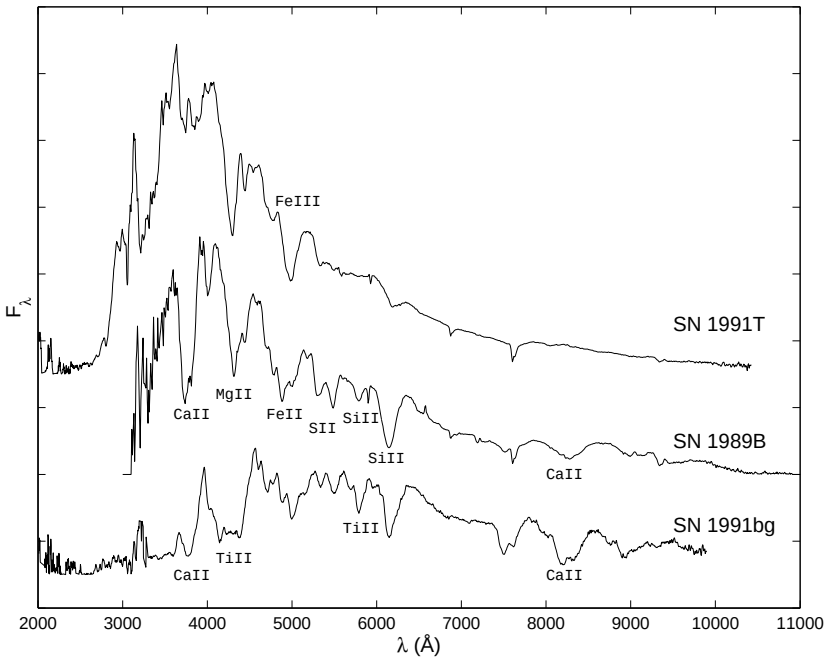

Figure 3.2: Spectra at maximum light of a normal SN Ia (`SN 1989B`, middle) and two SNe that define the main peculiar subtypes (`SN 1991T`, top, and `SN 1991bg`, bottom). The ions responsible for the most prominent features in each subtype are marked.

The Lightcurve Shape – Luminosity Relation

Among all the types, SNe Ia were found to show remarkably similar lightcurve and spectral properties, and small dispersion in absolute magnitude at maximum light ($\sigma < 0.4$ mag) [45, 37]. A further step forward in the use of SNe Ia as distance indicators was possible from the analysis of a large set of SNe in the *Hubble flow* [23, 65], i.e., in the range $0.01 < z < 0.1$, where the Hubble diagram is well approximated by a linear law through the Hubble parameter ($d_L = H_0^{-1} z$), and the peculiar velocities of galaxies are negligible when compared to the recession velocities. Through this analysis, it was found that the dispersion in peak magnitudes could be reduced by a correction based on the shape of the lightcurves, as described below. This finding added support to the case of using SNe Ia as *standardized candles* (i.e. after the correction is applied) for cosmology. Apart from the standardization of the peak magnitudes, the use of SNe Ia as distance indicators requires the adequate treatment of extinction corrections (in particular, the contribution from extragalactic extinction). This latter point was also addressed through the study of lightcurves from SNe Ia in the Hubble flow.

The standardization of SNe Ia luminosities is based on the observation that brighter SNe show *slower* time-evolution (i.e., *broader* lightcurves) and vice-versa. Several methods for parameterizing this relation have been developed. Phillips [61] defined the parameter $\Delta m_{15}(B)$ as the amount in magnitudes of the decrease of the B-band lightcurve between maximum light and 15 days after. A tight correlation was found between $\Delta m_{15}(B)$ and peak luminosity ($\sigma \sim 0.1$ mag) [62], after a correction for extinction based on the evolution of colors [41] is performed. The strength of this parameterization lies on the simplicity with which $\Delta m_{15}(B)$ can be obtained.

The success of the $\Delta m_{15}(B)$ parameter motivated the search for other parameterizations. Riess et al. [66] introduced the *multi-color lightcurve shape method* (MLCS), a sophisticated method to fit the relation between lightcurve shapes and peak absolute magnitudes for several colors simultaneously, allowing to include the extinction correction in the process. An alternative simpler method is based on the capability of reproducing the range of observed lightcurve shapes by stretching or contracting the time axis of a template lightcurve by a *stretch* factor s [59]. Figure 3.3 shows the power of this parameterization in standardizing SN Ia lightcurves.

These empirical correlations may be explained by a theoretical model parameterized by the mass of ^{56}Ni synthesized in the explosion. The radioactive decay of this isotope to ^{56}Co and then to stable ^{56}Fe is the main source of energy that powers the lightcurve around maximum light. The amount of ^{56}Ni determines the peak luminosity and the rate of change of the lightcurve [28].

The distances obtained from the three standardization methods are comparable in precision. A dispersion of $\sigma \sim 0.18$ around an inverse square law is found for current measurements of SNe Ia in the Hubble flow. Once photometric

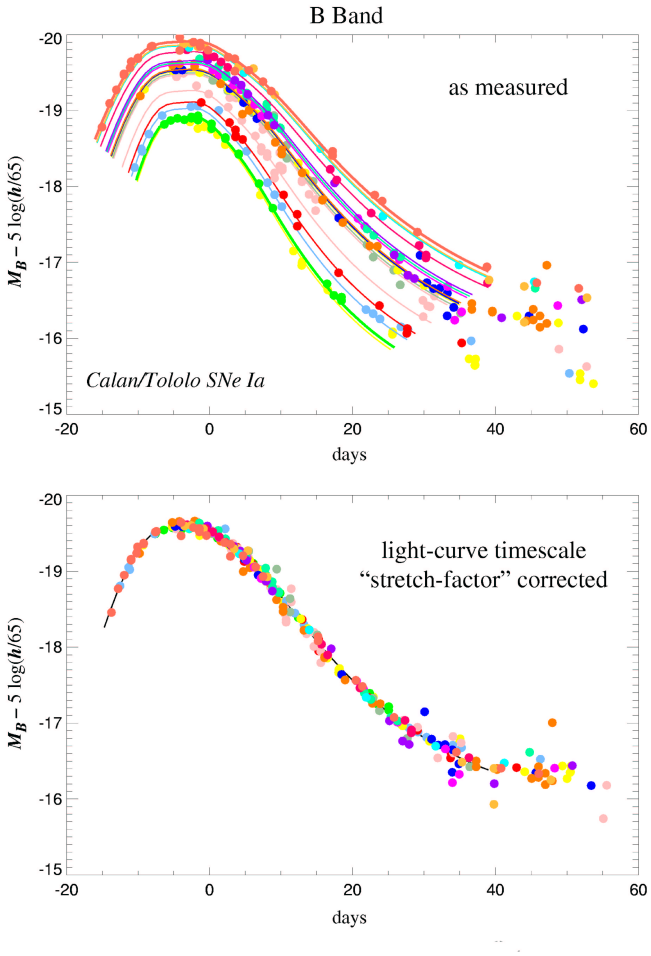

Figure 3.3: *Top*: Intrinsic spread in SN Ia B-band lightcurves. Note that SNe with slowly evolving lightcurves are brighter than average, and vice-versa. *Bottom*: The same lightcurves after a correction for stretch s is applied. The dispersion in peak magnitude is significantly reduced. Credit: [56].

uncertainties and errors in the redshift due to peculiar velocities (∼300 km/s) are removed, an intrinsic precision of ∼0.12 (6% in the distance) is obtained for SNe Ia.

Figure 3.4 shows an example of the use of $\Delta m_{15}(B)$ to correct SNe Ia measurements in the local Hubble diagram. In order to determine the value of H_0, the absolute distance scale needs to be determined with an external luminosity calibration. The uncertainty in this calibration poses a serious limitation to the measurement of H_0 with SNe Ia. The external calibration is based on the distances to some SNe Ia host galaxies, measured using different methods. For example, the period-luminosity correlation for Cepheid stars has been used by two different teams to calibrate the luminosity of SNe Ia and determine the value of H_0. The results from the two teams are divergent: Saha et al. [68] find $H_0 = 59 \pm 6$, while Freedman et al. [16] find $H_0 = 71 \pm 2(\pm 6$ systematic).

It should be noted, on the other hand, that the determination of the cosmological parameters Ω_M and Ω_Λ *does not* depend on the external calibration of SN Ia luminosities. As will be explained in Section 3.3, H_0 can be separated from Ω_M and Ω_Λ in Eqn. 2.33 and fitted together with the absolute magnitude M. In other words, Ω_M and Ω_Λ are determined from the *relative* brightness of SNe Ia at different redshifts.

3.2 Supernova Searches

In the previous sections, it was explained how SNe Ia can be identified and parameterized to become very precise distance indicators. Therefore, considered as standardized candles, SNe Ia fulfill items 1 and 2 in the requirements for the best distance indicators: they are extremely luminous, and very homogeneous, after a correction from the lightcurve shape. The third point in the list needs to be addressed: their ubiquity. Determining the values of the cosmological parameters Ω_M and Ω_Λ require the measurement of SNe Ia both in the local and the distant Universe. The question of detecting SNe Ia thus arises.

SNe Ia are unpredictable events. Also, they are transient: it takes approximately 20 days to reach maximum light, and they fade by about 2 magnitudes in the same interval of time after maximum light. This poses a problem since the standardization of the peak magnitude measurement requires a good coverage of the lightcurve, including measurements before or around maximum light. Furthermore, SNe Ia events are very rare on the time scales of a human life (one event every several hundred years in a normal galaxy). Therefore, an effective SN search should monitor a large amount of galaxies to improve the chances of discovery.

With the use of modern CCD mosaics, which cover relatively large fields of view (∼1 square degree), the problem of SN detection can be solved. For example, observing 1/3 of a square degree with a 4-meter class telescope using the R filter, an exposure of 10 minutes reaches 24th magnitude, thus allowing

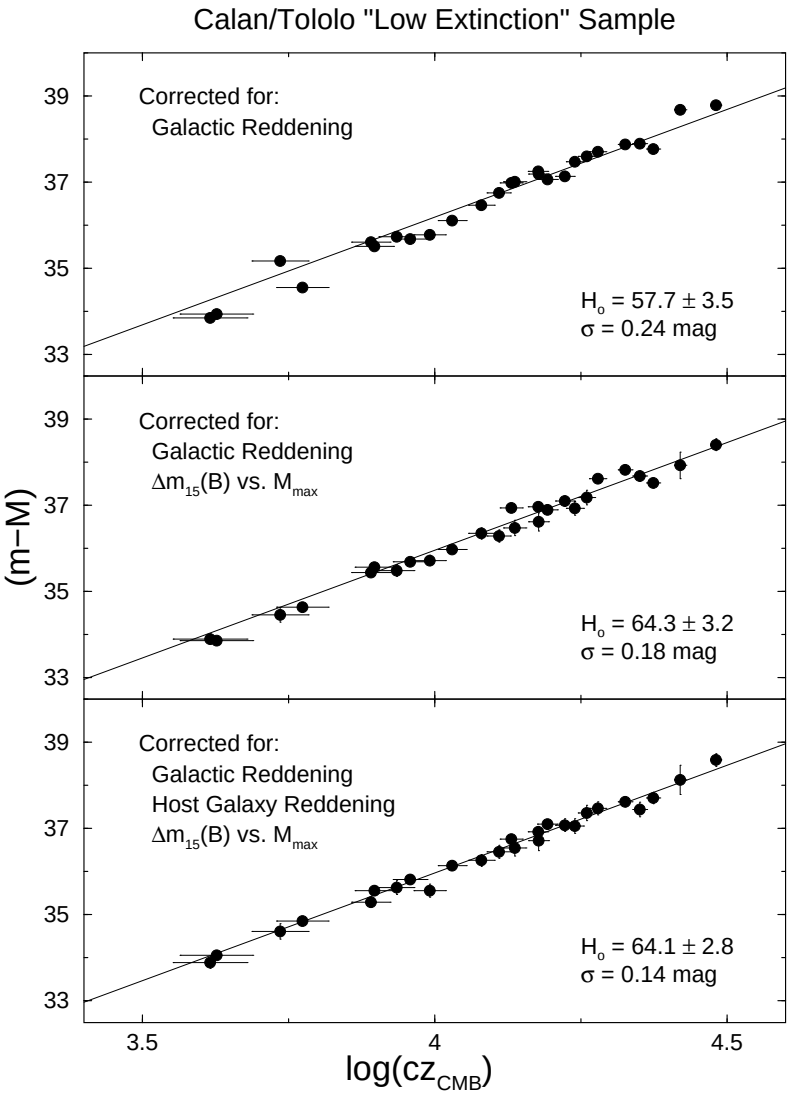

Figure 3.4: The local Hubble diagram for SNe Ia before (*upper panel*) and after *middle panel*) a correction to the magnitudes is done using $\Delta m_{15}(B)$. The *lower panel* shows the effect of correcting for host-galaxy extinction. Credit: [62].

to search around a million galaxies up to $z = 0.5$ in one night (~50 to 100 fields) [60]. The chances of discovery at high redshift are enhanced by the larger volumes covered, though the SNe are fainter. An additional complication of detecting SNe at high redshifts is that they are usually unresolved from their host galaxies. As a consequence, a secure discovery requires a method for subtracting the background from the newly found object. Finally, the success of the whole experiment depends on the confirmation of the SN type (done with spectroscopy) and on the follow-up photometric observation to build the lightcurves and correct for extinction. These observations require much more time at larger telescopes for high-redshift SNe than for nearby ones. How to obtain that precious telescope time to observe objects that have not been discovered yet?

In the 1990s, the SCP answered that question by developing a search method which proved to be successful in finding "batches" of high-redshift SNe Ia, all around maximum light, on a predetermined date. This allowed to schedule the confirmation and follow-up observations in advance. The method consists on taking two sets of observations of a certain field with an interval of three weeks, typically using one or two filters. The first observations are taken right after new Moon, to reduce the sky background of the images from both sets. In a process that requires great computing power, the images from the two sets are aligned, convolved (to account for differences in seeing), and scaled. The images from the first epoch are subtracted from those of the second epoch. The results are scanned for possitive residuals which would indicate an object that has brightened. The separation of three weeks between observations optimizes the discovery of SNe on the rising phase (at $z = 0.5$, this interval corresponds to two weeks in the SN rest frame).

The success of this search method, and the growing interest in SNe Ia observations, has opened the possibility for a new search strategy, called *rolling search*. In this case, large blocks of observing time at a single telescope are used to image the same fields repeatedly every few days, using multiple filters, for several months. In this manner, the same block of observations serves to perform the searches and automatically assures the follow up of the objects found. The only additional observations required are those for spectroscopic confirmation. Several projects have adopted the rolling search mode: the SCP, the *High-Z Supernova Search* (HZSNS), the *Supernova Legacy Search* (SNLS), the *Equation of State: SupErNovae trace Cosmic Expansion* (ESSENCE), etc.

3.3 Results: The Accelerating Universe

Once SNe Ia at low and high redshift are found and their magnitudes computed (normalized with a lightcurve shape – luminosity correlation), they can be placed in the Hubble diagram and the values of the cosmological parameters can be solved from Eqn. 2.33. In practice, this implies the measurement of the standardized candles through a certain filter in order to compare suitably

defined peak magnitudes. In the optical range, there is a series of passbands defined by their associated filters ($UBVRI$). These passbands are shown in Figure 3.5, together with the spectrum of a SN Ia at maximum light. The choice of the B-band as the most commonly used in cosmology with SNe Ia is based on higher brightness of these objects on that wavelength region at maximum light, and on the availability of better constrained standardization from the B-band lightcurves.

Now, when observing SNe at ever higher redshifts, the light emited in the range of the B filter arrives at Earth at longer wavelengths. Therefore, comparing the *observed* magnitudes in B (m_B) of SNe at different redshifts would produce an erroneous result, since the values would not correspond to the same measure of the "standardized candle". In order to correct the observed magnitudes with a certain filter as the emited flux is redshifted, a correction term has been introduced: the *K-correction*.

K-Corrections

The effect of redshift on luminosity distances, the K-correction, was first studied and measured for the observation of galaxies [52]. When observing through a certain filter i, the magnitude of a object a redshift z in that filter would be

$$m_i(z) = m_i(z = 0) + K_i(z), \tag{3.1}$$

where $K_i(z)$ is the redshift-dependent K-correction that applies to that redshift. For an object of flux $F(\lambda)$ observed through a filter of transmission function $T_i(\lambda)$, it can be seen that

$$K_i(z) = 2.5 \log \left((1+z) \frac{\int F(\lambda) T_i(\lambda) d\lambda}{\int F(\lambda/(1+z)) T_i(\lambda) d\lambda} \right). \tag{3.2}$$

An additional complication in the case of SN Ia observations, as opposed to the case of galaxies, is that SN Ia spectra evolve with time. The evolution is particularly rapid around maximum light, which produces rapid changes in the values of K_i as a function of time. Therefore, it is not possible to use a single SN Ia spectrum to compute the K-corrections at all times. Spectral time series are needed to compute the corrections. The observed homogeneity in the spectra of SNe Ia allows the use of time series of template spectra to compute K-corrections for any SN with small uncertainties.

In addition to the difficulties caused by the change of the spectra with time, when reaching $z \sim 0.5$, a K-correction for the B filter requires information of the U part of the spectrum. This information is observationally difficult to obtain with the majority of the instruments available. Moreover, beacuse of line blanketing, the evolution of the SN Ia spectrum blueward of 4000 Å is particularly rapid. Kim et al. [35] introduced a different observational approach for the case of SNe Ia. They demonstrated that, by observing high-redshift SNe

in the R-band and defining a cross-filter K-correction, the uncertainties could be substantially reduced, because at $z \sim 0.5$ the R filter is very similar to a rest frame B filter. In general, the modified K-correction that translates from the observed filter i to a filter j at $z = 0$ is

$$K_{ij}(z) = 2.5 \log \left((1+z) \frac{\int F(\lambda) T_i(\lambda) d\lambda}{\int F(\lambda/(1+z)) T_j(\lambda) d\lambda} \right) + C_j - C_i, \tag{3.3}$$

where C_i and C_j are constants that define the zero point of the magnitude system for each filter. The observed magnitudes in filter j are therefore corrected by

$$m_j(z) = m_i(z=0) + K_{ij}. \tag{3.4}$$

A further effort in reducing the uncertainties of the K-corrections was attempted by the HZSNS team. They defined a set of filters designed so that they would match the B and V filters at $z = 0.35$ and $z = 0.45$ [72]. With this strategy, the systematic uncertainties in the calculation of K-corrections for $0.25 < z < 0.55$ were reduced, at the expense of having to define a calibration system for the new filters. This practice has the additional difficulty of determining the optimal filter to use when the redshift of the SN is still unknown.

The Ω_M–Ω_Λ Plane

The treatment of SNe Ia measurements described above leads to the use of an *effective magnitude* as the measure of the standardized candle which allows to solve for the cosmological parameters by comparing low- and high-redshift measurements. This effective magnitude is given by the choice of a filter i in which the measurements at low-redshift are done. For the high-redshift SNe, the effective magnitude is

$$m_i^{eff} = m_j + \Delta_{corr} - K_{ij} - A_i - A_j, \tag{3.5}$$

where Δ_{corr} is a correction term given by the lightcurve shape–luminosity relation (Sec. 3.1), K_{ij} is the cross-filter K-correction from Eqn. 3.3, A_i is a correction for extinction in the host galaxy (assuming all the extragalactic extinction is produced in the host galaxy), and A_j is the corresponding Galactic extinction in the observed filter. The way each term on the right-hand side of Eqn. 3.5 is treated, in particular Δ_{corr} and A_i, varies among the different teams. The difficulties in the determination of A_i have given rise to a variety of approaches which will be discussed below.

As seen above, the B filter is usually chosen because of the higher brightness of SNe Ia in that band at maximum light, and because of the better standardization of peak magnitudes. The B filter has the additional advantage of being reproducible with optical filters up to $z \sim 1$.

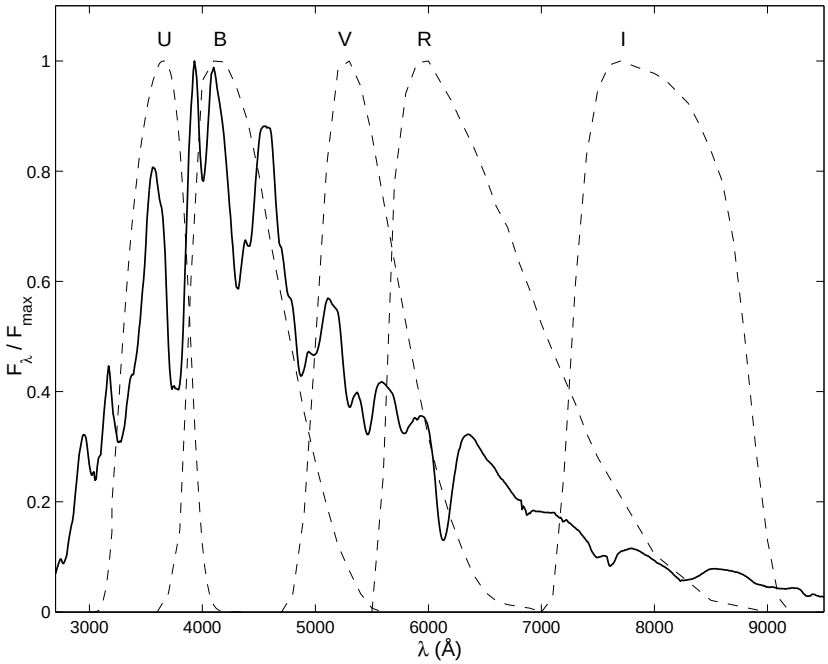

Figure 3.5: A SN Ia spectrum at maximum light with the optical photometric passbands $UBVRI$ superimposed. The wavelength λ is given in the rest frame.

These definitions, introduced in Eqn. 2.33, would allow to perform a fit of the cosmological parameters H_0, Ω_M and Ω_Λ by solving

$$m_B^{eff} = M_B + 5\log d_L(z; H_0, \Omega_M, \Omega_\Lambda) + 25, \tag{3.6}$$

given a value of the absolute peak magnitude in the B-band. However, as we have seen, the calibration of M_B is not certain. Instead, the measurements of SNe Ia are used to determine only Ω_M and Ω_Λ from the *relative* brightnesses. The Hubble constant is therefore factorized out from d_L and fitted together with M_B as a nuisance parameter.

An important feature of Eqn. 3.6 is the manner that measurement uncertainties are propagated into the Ω_M–Ω_Λ plane. Assuming M_B and H_0 are known, the measurement of m_B^{eff} for SNe at a fixed z would yield a relation between Ω_M and Ω_Λ. Measurement uncertainties would thus produce a band-shaped confidence region in the Ω_M–Ω_Λ plane. By repeating this exercise at different values of z, different relations between Ω_M and Ω_Λ are obtained, with associated confidence bands of varying shape, as pointed out by Goobar and Perlmutter [20]. Figure 3.6 from [18] shows a realization of this exercise with simulated measurements of SNe Ia ($\sigma_m = 0.02$ mag). The left-hand panel shows the series of 1σ bands at different redshifts (between $z = 0.2$ and $z = 1.8$, at intervals of 0.2). The experiment of building the Hubble diagram with measurements of SNe Ia at different redshifts can be represented by the combination of the confidence bands for each redshift, as shown on the right-hand panel of Fig. 3.6. The advantage of increasing the range of z is that the combined confidence contours in the Ω_M–Ω_Λ plane are dramatically reduced because of the geometry implied by Eqn. 3.6.

Measurements of SNe Ia not only involve uncertainties in the magnitudes, but also in the redshift. The latter uncertainties are usually neglected when performing cosmology fits. For completeness, we study their effect on the precision of Ω_M and Ω_Λ. A cosmology fit that considers the uncertainties in both coordinates (m_B and z) can be done using the *effective variance method* (EVM) [53], which is a modification of the least-squares or maximum likelihood methods by introducing an additional term in the uncertainties.

Suppose the measurements of N SNe ($i = 1, \ldots, N$) are m_i and z_i, with uncertainties σ_{m_i} and σ_{z_i}, and the cosmological model to be fitted (the right-hand side of Eqn. 3.6) is written as $f(z_i; \Omega_M, \Omega_\Lambda)$. The *negative logarithmic likelihood function*, $\mathcal{L}(\Omega_M, \Omega_\Lambda)$, considering only errors in m_i is

$$\mathcal{L}(\Omega_M, \Omega_\Lambda) = -\frac{1}{2}\sum_{i=1}^{N}\left(\frac{m_i - f(z_i; \Omega_M, \Omega_\Lambda)}{\sigma_{m_i}}\right)^2. \tag{3.7}$$

Under the assumption that $\left(\frac{\partial f}{\partial z}\right)\Big|_{z_i}$ is approximately constant over the interval $z_i - \sigma_{z_i} < z < z_i + \sigma_{z_i}$, it can be shown that Eqn. 3.7 holds in the case with uncertainties in m_i and z_i, if $\sigma_{m_i}^2$ in the denominator is replaced by

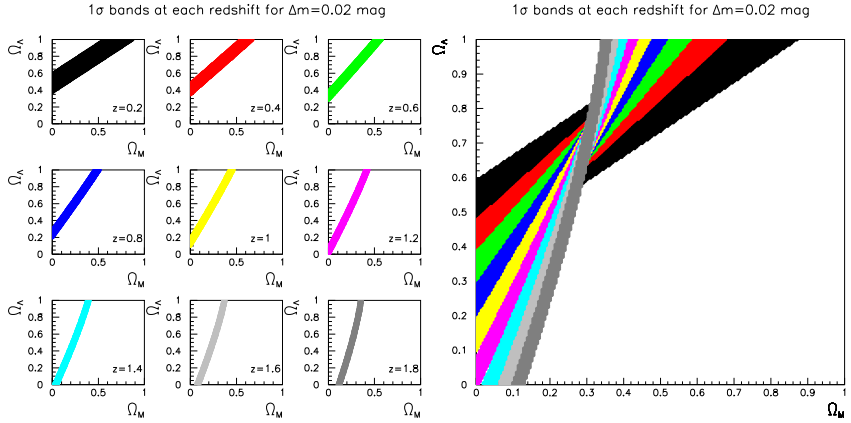

Figure 3.6: *Left-hand panel*: Simulations of the confidence bands in the Ω_M–Ω_Λ plane obtained with SN measurements of precision $\sigma_m = 0.02$ mag at different fixed redshifts, between $z = 0.2$ and $z = 1.8$. Note that the slope of the bands changes with z. *Right-hand panel*: The combination of measurements at different redshifts reduces dramatically the size of the confidence regions in the Ω_M–Ω_Λ plane. Credit: [18].

$$\delta_i^2 = \sigma_{m_i}^2 + \left(\frac{\partial f}{\partial z}\right)\Big|_{z_i}^2 \sigma_{z_i}^2. \tag{3.8}$$

This replacement of the uncertainties is the basis of the EVM.

The importance of the new source of uncertainties introduced depends on the relative weight of the two terms on the right-hand side of Eqn. 3.8. For given σ_{m_i} and σ_{z_i}, this depends on the value of $\left(\frac{\partial f}{\partial z}\right)\Big|_{z_i}$, which is a function of z_i. This function is shown in Figure 3.7 for two different cosmologies. It can be seen that the relative effect of redshift uncertainties is enhanced at low redshifts.

There are three main ways to obtain the value of z, with differing precision. First, the position of narrow lines in the host-galaxy spectrum, if they can be detected, yields redshifts with precision of $\sigma_z \sim 0.001$. Second, the position of SN features, which are largely broadened by the expansion of the ejecta, determine z with uncertainties $\sigma_z \sim 0.01$. Third, when no spectrum is available, a photometric redshift based on the color of the host galaxy can be used, with typical precision of $\sigma_z \sim 0.1$. The latter case is not suitable for cosmology, due to the large uncertainty and because a spectroscopic observation is needed to determine the SN type, as seen above.

Given a value of intrinsic dispersion in m of $\sim$0.1, for uncertainties in z of $\sim$0.01, the contribution of the latter to the total error δ would be significant

at $z \lesssim 0.2$. This would enlarge the confidence contours in the Ω_M–Ω_Λ plane. Uncertainties of $\sigma_z \sim 0.001$ are not expected to significantly affect the precision of Ω_M and Ω_Λ.

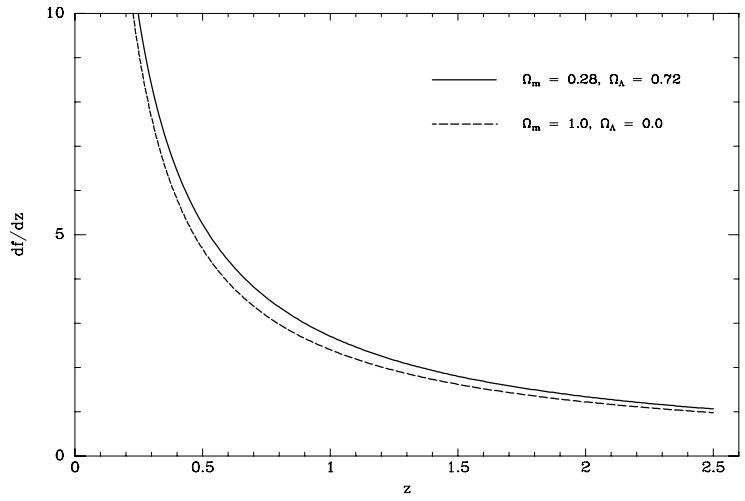

Figure 3.7: The derivative $\left(\frac{\partial f}{\partial z}\right)$ of the model for m_B^{eff} (Eqn. 3.6) with respect to z. Note that for low values of z, the uncertainties in z would have a greater impact on the precision of cosmological parameters.

Cosmology Fits

In the following, we focus on the latest results by the SCP, presented in **Paper A**. The paper presents the cosmology fit done using data from 11 newly analyzed high-redshift SNe ($0.36 < z < 0.86$) observed with the *Hubble Space Telescope* (HST), in addition to other 27 high-redshift SNe ($0.17 < z < 0.83$) from Perlmutter et al. [57], and 26 low-redshift SNe ($0.01 < z < 0.13$) from Hamuy et al. [21], Riess et al. [65] . In this case, the standardization of the peak magnitudes is based on the stretch parameter s. The mild dependence of the peak magnitude on s is represented by a slope parameter α, such that

$$\Delta_{corr} = \alpha(s - 1). \tag{3.9}$$

Instead of fitting the value of α from the measurements of SNe in te Hubble flow, this parameter is included in the overall cosmology fit. In sum, the expression of Eqn. 3.6 is rewritten as

$$m_B = \mathcal{M}_B + 5\log \mathcal{D}_L(z;\Omega_M,\Omega_\Lambda) - \alpha(s-1). \tag{3.10}$$

Here, m_B is the Galactic extinction and K-corrected peak magnitude in rest-frame B-band. The correction for host-galaxy extinction is addressed separately, as described below. $\mathcal{D}_L \equiv H_0 d_L$ is the "Hubble constant-free" luminosity distance, and $\mathcal{M}_B \equiv M_B - 5\log H_0 + 25$ is the "Hubble constant-free" B-band peak absolute magnitude of a SN Ia with $s = 1$ and true peak absolute magnitude M_B. The measurements of m_B, z and s from the SN Ia sample mentioned above are used to fit Ω_M and Ω_Λ, together with the two nuisance parameters $\mathcal{M}_B$ and α.

Host-Galaxy Extinction. Host-galaxy extinction corrections are determined from color index measurements. A *color excess* is defined as the difference between a measured color index and the intrinsic color index of the object. For example, a measured $(B-V)$ color of an object with intrinsic $(B-V)_0$ corresponds to a color excess of

$$E(B-V) \equiv (B-V) - (B-V)_0. \tag{3.11}$$

The extinction A in a certain band is proportional to the color excess. For example,

$$A_B \equiv R_B E(B-V), \tag{3.12}$$

which introduces the definition of the *total-to-selective absorption coefficient* in the B-band, R_B, (a typical value for a SN spectrum is $R_B = 4.1$, from the extinction law of O'Donnell [50]).

Obtaining color excesses for high-redshift SNe Ia is a difficult task which involves large measurement uncertainties and the dispersion in intrinsic SN Ia color, which is determined from the measurement of nearby SNe. These uncertainties are even greater when $(U-B)$ colors have to be considered (this is the best match rest-frame color for observed $(R-I)$ at $0.7 < z < 1$).

In **Paper A**, two strategies to cope with the problem of host galaxy extinction are taken. First, following Perlmutter et al. [57], the most reddened SNe are rejected from the sample and the rest are not corrected. Second, the measured color excesses are used to correct for extinction. In both cases, the intrinsic colors in rest-frame $(B-V)_0$, $(V-R)_0$ and $(R-I)_0$ were computed at each epoch using the low-z data. A smooth curve was fitted to the measured colors versus date relative to maximum light. The host-galaxy extinction for these nearby SN color measurements was handled by applying a blue-sided ridgeline fit, by which all points lying more than 1σ to the red of the fit were considered as being exactly 1σ away.

Through the first approach, objects with $E(B-V) > 0.1$ and more than 2σ above zero are discarded from the sample. The distribution of color excesses for

the remaining SNe is compared with that of the low-z sample, taking into account the measurement uncertainties. The only requirement for obtaining an unbiased fit is that the distributions are statistically identical —it is *not* necessary that both distributions are consistent with zero extinction. Figure 3.8 shows that the distributions at low- and high-redshifts are compatible. The use of magnitudes uncorrected for extinction requires the addition of the intrinsic dispersion in the magnitudes (taken from the low-z sample, as 0.17 mag [23]).

The Hubble diagram built through this approach is shown in Figure 3.9 where, for clarity, points corresponding to SNe within $\Delta z < 0.01$ from each other have been combined using a weighed average. The fit resulting from the measurements (using individual measurements and not the averages shown in the plot) yields $(\Omega_M, \Omega_\Lambda) = (0.25^{+0.07}_{-0.06}, 0.75^{+0.06}_{-0.07})$, assuming a flat Universe. This fit is shown with a solid curve in Figure 3.9. The lower panel shows the residuals from an empty Universe (as plotted in Fig. 2.1) to emphasize the differences among the models. The confidence contours of the fit are shown in Figure 3.10. A non-zero cosmological constant is required with a probability >99%. Moreover, from Eqn. 2.37, the result obtained means that the expansion of the Universe is presently *accelerated*. This result is also supported with a probability >99% (see Fig. 3.10).

The second approach to correct for host-galaxy extinction in **Paper A** is to directly use the measurements of $E(B-V)$. The high-precision color-index measurements available for the 11 HST SNe ($\sigma < 0.08$) allows a direct estimation of the host-galaxy extinction using Eqn. 3.11, without the need of any assumption about the intrinsic extinction distribution (see the HZSNS approach below). A less stringent cut on the color excess is used (rejecting objects with $E(B-V) > 0.25$ and more than 3σ above zero) because it has been found in studies of low-redshift SNe, that these very reddened SNe appear to be over-corrected for extinction when using a standard reddening law [62]. Figure 3.11 shows the effect of this correction for the 11 HST SNe of **Paper A**. The uncertainties of ground-based color measurements from Perlmutter et al. [57] are larger (compare the last two panels in Figure 3.8), which would introduce larger uncertainties in the results of the fit. The top and bottom panels of Figure 3.12 shows this difference. The fits to the extinction-corrected data are done adding an intrinsic uncertainty in m_B of 0.11 mag [62]. The results of the cosmology fits using direct extinction corrections on the whole data set of **Paper A** are $(\Omega_M, \Omega_\Lambda) = (0.28^{+0.11}_{-0.10}, 0.72^{+0.10}_{-0.11})$, assuming a flat Universe. The case of $\Omega_\Lambda > 0$ is still favored with probability >99%.

A different approach to treat host-galaxy extinction from the two used in **Paper A** is to assume an asymmetric prior on the color excesses, as done by the HZSNS. By this assumption, negative values of $E(B-V)$ are given zero probability, and possitive values would have a sharp peak at $E(B-V) \sim 0$, with an exponential decline. It should be noted that, if colors are measured with different precision at low- and high-redshift, such a prior would introduce a bias on the result of the fit, depending on the exact shape of the prior distribution.

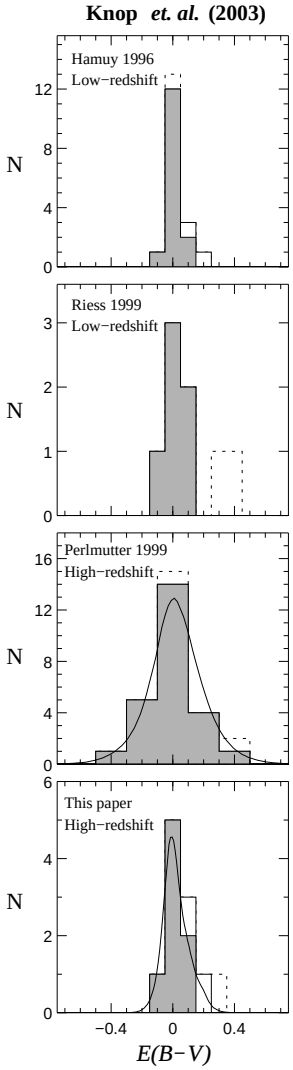

Figure 3.8: Histograms of measured $E(B-V)$ for the four SN samples analysed in **Paper A**. The shaded histograms represent the SNe used in the first approach to treat host-galaxy extinction (see text). The open boxes represent SNe in the complete sample sample used in the second approach of extinction correction, and the dotted boxes correspond to rejected SNe (see **Paper A** for details). The solid lines in the two bottom panels represent the distribution of color excesses observed at low redshifts, considering the different measurement precisions. The distribution for high-z SNe is consistent with that of low-z SNe.

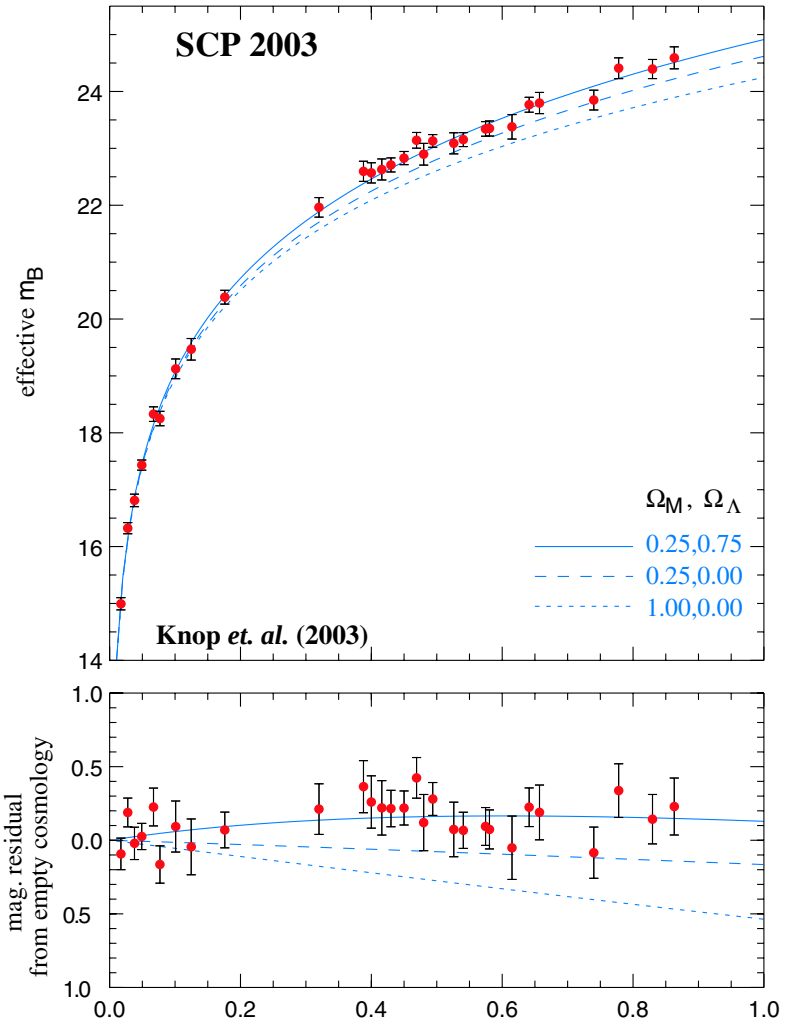

Figure 3.9: *Upper panel*: Averaged Hubble diagram from **Paper A** (treating the exticntion corrections through the first approach, see text). For clarity, points within $\Delta z < 0.01$ from each other have been averaged. The best-fit cosmology $(\Omega_M, \Omega_\Lambda) = (0.25, 0.75)$ is represented by a solid curve. For comparison, other two cosmologies are shown: $(\Omega_M, \Omega_\Lambda) = (0.25, 0)$ and $(\Omega_M, \Omega_\Lambda) = (1, 0)$. *Lower panel*: Residual Hubble diagrams, compared to the case of an empty Universe $(\Omega_M, \Omega_\Lambda) = (0, 0)$. The significance of the detection of dark energy is stressed in this panel.

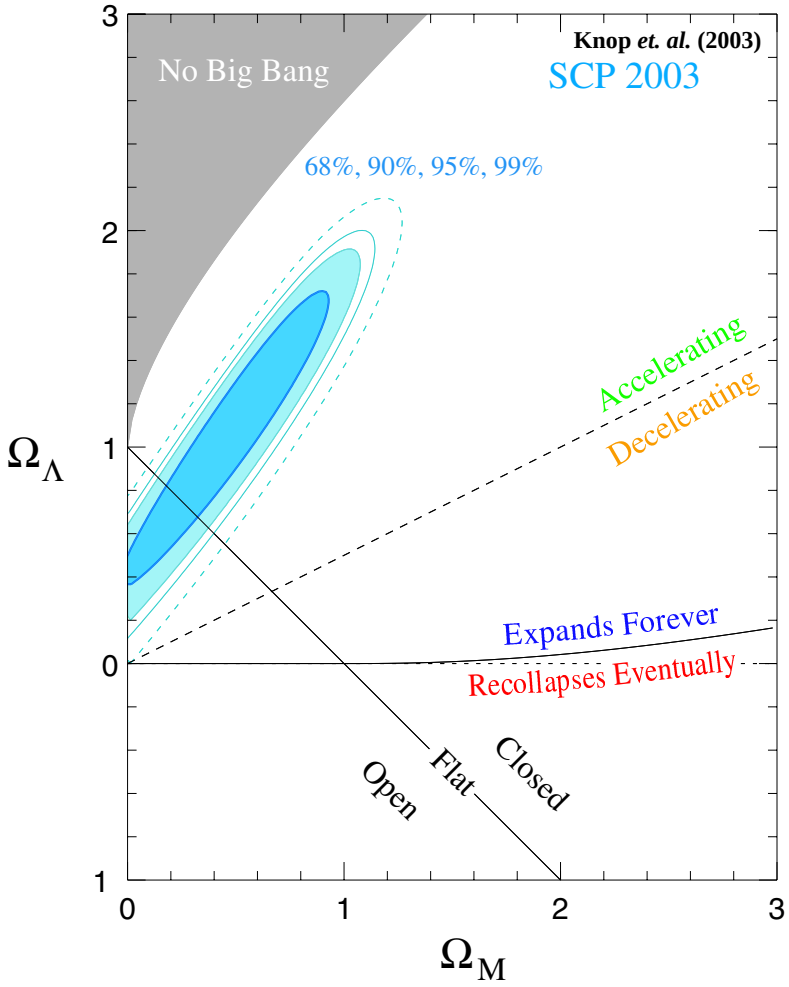

Figure 3.10: Confidence regions in the Ω_M–Ω_Λ plane from **Paper A** (treating the exticntion corrections through the first approach, see text).

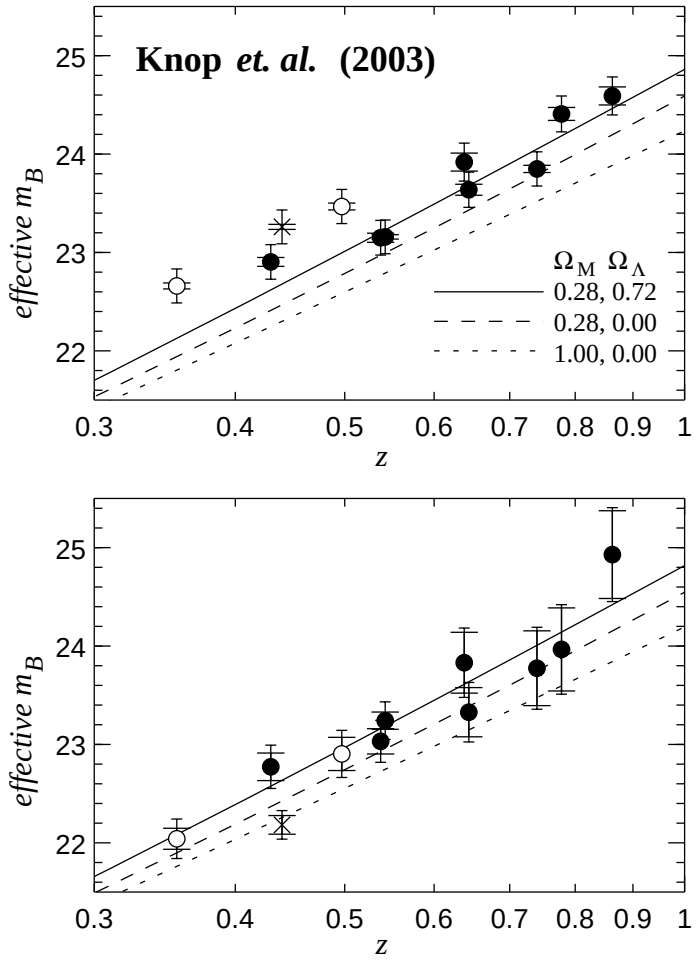

Figure 3.11: Hubble diagram of effective K- and stretch corrected m_B versus z for the 11 SNe observed with the HST in **Paper A** . Open circles represent the SNe rejected in the first approach for treating host-galaxy extinction. The cross corresponds to a SN which was rejected from all fits for being too reddened. The lines correspond to three example cosmologies indicated in the graph. The solid line is the best-fit cosmology when full extinction corrections are applied. *Upper panel*: No host-galaxy correction applied. Inner error-bars show measurement uncertainties. Outer error-bars include 0.17 mag of intrinsic dispersion. *Lower panel*: Additional host-galaxy correction was applied using the measured $E(B-V)$ values. The inner error-bars (measurement uncertainties) are now larger. Outer error-bars add 0.11 of intrinsic dispersion.

While the use of a sharp enough peak at low extinctions introduces little bias, its effect is to almost completely eliminate the contribution of errors on $E(B-V)$ to the Ω_M–Ω_Λ confidence contours. This is shown in the middle panels of Figure 3.12 for different SN samples, including the results of the HZSNS team [63]. The choice of a sharply peaked prior is similar to rejecting the most extincted SNe and assuming no extinction for the rest (the first approach in **Paper A**), but without testing this assumption.

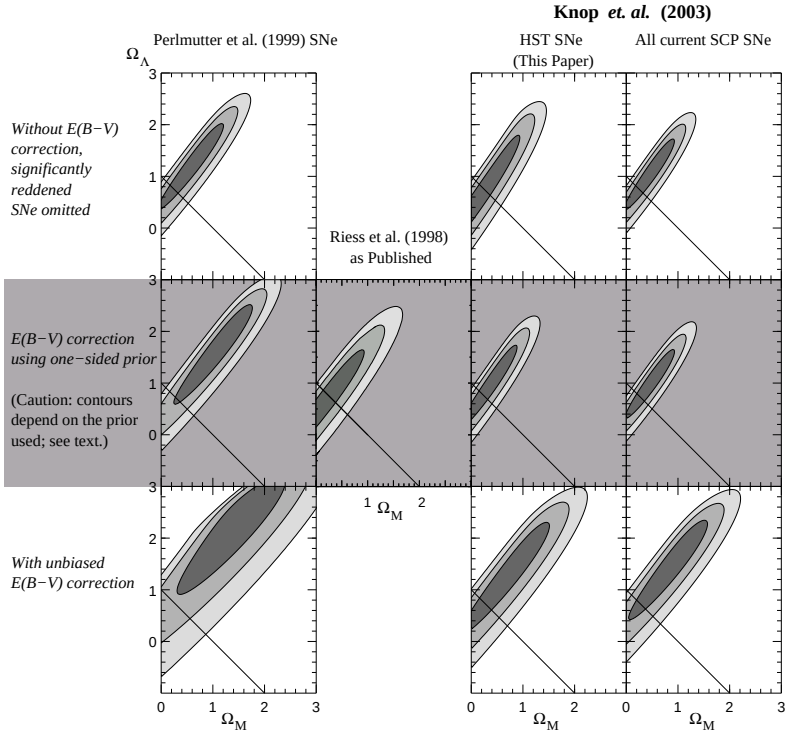

Figure 3.12: Confidence regions in the Ω_M–Ω_Λ plane for different data subsets and methods to treat host-galaxy extinction used in **Paper A**. *Upper panels*: First approach described in the text, omitting significantly reddened SNe. *Middle panels*: Third approach described in the text, using a one-sided extinction prior. *Upper panels*: Second approach presented in the text, where extinction corrections are applied without any prior. Note that the fits in the middle row can either yield results similar to those in the upper row, or biased results. Also note the precision obtained when correcting for extinction with the HST color measurements (lower-right panel).

Finally, Figure 3.13 shows the results of Ω_M and Ω_Λ for a combination of

the SCP measurements from **Paper A** and a subsample of well-measured high-redshift SNe Ia from the HZSNS team [63]. Under the assumption of a flat Universe, the combination yields $(\Omega_M, \Omega_\Lambda) = (0.26^{+0.07}_{-0.06}, 0.74^{+0.06}_{-0.07})$. Recently published data from ground-based observations of 8 new high-redshift SNe Ia yield consistent results [76].

3.4 Measurements of Dark Energy

The Cosmological Constant Problem

The results of a Universe with non-vanishing cosmological constant and in a current phase of accelerated expansion are of enormous importance for our understanding of the dynamics of the cosmic fluid. Even more exciting are the fundamental questions raised by these results. The measurement of $\Omega_\Lambda \sim 1$ at present time is one of the most puzzling results in modern theoretical physics. If vacuum energy is to be explained by a quantum theory of gravitation, its fundamental mass scale would be set by the Planck mass, $m_{Pl} = 1.2 \times 10^{19}$ GeV (in natural units). The energy density would be of the order of $\rho \sim m_{Pl}^4 \sim 10^{76}$ GeV^4. However, the measured value of $\Omega_\Lambda \sim 1$ corresponds to $\rho_\Lambda \sim 10^{-46}$ GeV, i.e. 122 orders of magnitude smaller. Certainly, this severe discrepancy requires a correct theoretical explanation of the nature of vacuum energy, conceivably in relation with the development of a theory of quantum gravity.

The Equation-of-State Parameter

We consider now the non-matter component of the total energy density to have a general equation of state $p = w\rho$, instead of a constant density, as discussed in Section 2.4. This component, called *dark energy*, would have an associated density parameter Ω_X (Eqn. 2.42).

In **Paper A**, the Hubble diagram for SNe Ia was used to obtain the equation-of-state parameter for dark energy, w, assumed to be constant with z, together with Ω_M and Ω_X. Given the limitations of the data available to fit those parameters (and the nuisance parameters $\mathcal{M}$ and α), the additional assumption of a flat Universe ($\Omega_M + \Omega_X = 1$) was taken. The results of the fit, represented in the w–Ω_M plane are shown in Figure 3.14. The treatment of host-galaxy extinction corrections was done, as above, by selecting the least extinguished SNe (left-hand panels), and by correcting with the measured $E(B-V)$ values (right-hand panels). The SN Ia data alone (top panels) set a limit of $w < -0.64$ with probability of 99%. The middle panels of Figure 3.14 show the results from SNe Ia overlayed on the results of two independent experiments: the Two-Degree Field Galaxy Redshift Survey (2dFGRS, [27, 79], and the Wilkinson Microwave Anisotropy Probe (WMAP) and other CMBR measurements [6, 73]. Since these other experiments yield confidence contours with different orientations as those of SNe, the combined measurements (bottom panels) provide much stronger constraints

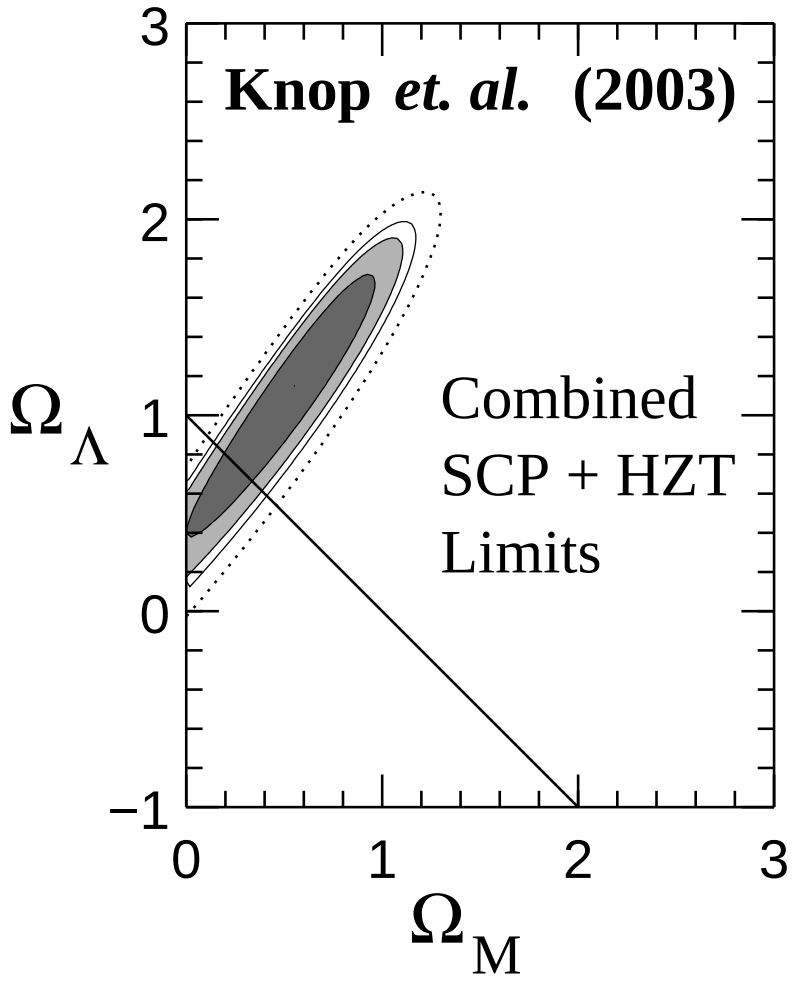

Figure 3.13: Confidence regions in the Ω_M–Ω_Λ plane (68%, 90%, 95% and 99%) combining the data from the SCP (**Paper A** and [57]) and the HZSNS team [63].

on both Ω_M and w. When marginalizing the results over Ω_M, the measurement of the equation-of-state parameter is $w = -1.05^{+0.15}_{-0.20}$ (using the subsample of SNe with low extinctions), or $w = -1.02^{+0.19}_{-0.24}$ (using the SN data corrected for host-galaxy extinction). These results are consistent with a low-density Universe dominated by vacuum energy (with $w = -1$), although the nature of the dark energy is not well constrained.

3.5 Systematic Uncertainties

The results of the cosmological parameters presented above are based on the comparison of luminosity distances for low- and high-redshift SNe Ia, under the assumption that the brightness measurements correspond to the same measure of the standardized candle. A number of systematic effects can introduce a bias in the brightness as a function of redshift. These effects may arise from differences in the measurement techniques, from differing SN sample selections, or from more fundamental variations in the properties of the standardized candles or their environment. If the effects are large and not well constrained or corrected, they would hamper the accuracy on the determination of the cosmological parameters.

The following presents a brief description of the main possible sources of systematic error and their estimated effects on the current SN Ia measurements.

SN Samples

It is important that, after a lightcurve-shape correction, the peak magnitudes of SNe Ia at different redshifts provide an unbiased measure of the luminosity distances. This requires the correct identification of SN types, the control of selection effects, and the understanding of how physical properties of SNe Ia may depend on z (in particular, whether such dependence can be accounted for by the lightcurve-shape correction which is defined at low-z).

Type Contamination. The measurements should be done on type Ia supernovae, which are standardized candles. The lightcurve data is not sufficient to distinguish the different types of SNe, especially between SNe Ia and Ib/c. Spectroscopic data is needed to secure the classification. **Paper A** uses only SNe for which these data are available. However, the classification of high-redshift SNe can be less secure due to higher noise or host-galaxy contamination in the spectra, and because the most prominent spectral feature defining SNe Ia (Si II λ6355) is redshifted out of the optical range for $z > 0.5$. The identification of higher-redshift SNe Ia relies on other, weaker spectral features on the blue part of the rest-frame spectrum.

In **Paper A**, the cosmology fit was repeated using only the securely classified SNe Ia. Its comparison with the fit using the complete sample produces an

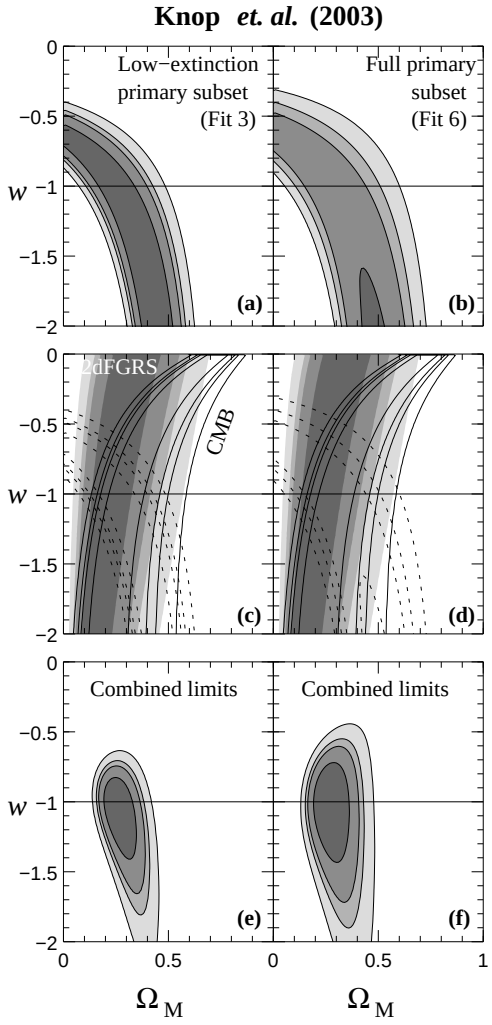

Figure 3.14: Confidence regions in the Ω_M–w plane for $\Omega_M + \Omega_X = 1$ and non-varying w. The regions correspond to 68%, 90%, 95% and 99% confidence levels. The left-hand panels show the results of the first approach of host-galaxy extinction treatment (see text) presented in **Paper A**. The right-hand panels show the results of the second approach in which extinction is directly corrected. The upper panels show the results from SNe alone. The middle panels have these contours (*dotted lines*) with the results of 2dFGRS (*filled contours*; [27]) and CMBR measurements (*solid lines*; [73]). The lower panels show the combination of the three experiments.

estimate of the systematic uncertainty on Ω_M for a flat Universe of 0.03.

Malmquist Bias. There are several selection effects that might be introduced from the way SNe are discovered and chosen for further follow-up. The most important of such effects is the *Malmquist bias* [42, 43]. This effect leads to a bias toward brighter objects among the SNe discovered through magnitude limited searches (such as the ones described in Section 3.2), near the redshift limit of the searches. The effect is not present in the case of SNe discovered through galaxy surveys. The size of the effect is proportional to the square of the intrinsic dispersion of the distance indicator and further depends on the phase of the lightcurve when the SNe are discovered (since a discovery near maximum light at a certain magnitude would put the SN closer to the distance limit).

As noted for the extinction corrections, the overall effect of the Malmquist bias on the cosmology fit arises from the *difference* of its effect at low and high redshift. In **Paper A**, the origin of all the SN samples used is studied in detail and a difference of 0.01 mag is found between low- and high-redshift SNe. A propagation of the estimated biases to the cosmology fit results in an estimate of the systematic effect on Ω_M in a flat Universe of only 0.01.

Evolution. Any possible change of the physical properties as a function of redshift may introduce systematic effects in the relative luminosity distances of low- and high-redshift SNe. We have seen that observational differences among low-z SNe can be used to correct differences in absolute magnitude, in particular through lightcurve shape–luminosity relations, which are explained by variations in some physical propertie of the SN (e.g., the amount of ^{56}Ni synthesized in the explosion). A dependence of such property on redshift would not introduce any bias in the measurements if the lightcurve shape–luminosity relation used to correct the magnitudes accounts for the whole range of the physical property at high redshift also. A first test for this effect is to compare the distribution of lightcurve-shape parameters for SNe at low and high redshifts. In **Paper A**, the values of the stretch parameter s are compared. All the values of s found at high redshift have their counterparts at low redshift. Also, Goldhaber et al. [17] find no dependence of the strectch parameter on z.

Additional tests based on comparisons of observational properties can be done. For instance, the lightcurve rise time, which is believed to be an indicator of the energetics of the explosion [49, 29], were first suggested to vary with redshift [64], although a more recent work finds good agreement for low- and high-redshift SNe [2]. Of ultimate importance are spectral studies, due to the amount and variety of information about SN physics that can be obtained from spectral properties. Also, the spectra can be used to define alternative ways of calibrating SN Ia luminosities, independently from lightcurve shapes, as presented in **Paper II** (see Section 5.2). The resemblance between spectra of low-

and high-redshift SNe [55, 14, 5, 67, 8] support the similarity of the physical processes in the two cases. A quantitative analysis of spectroscopic parameters comparing low- and high-redshift SNe, presented in **Paper IV**, shows no discrepancies between the samples (see Section 5.3).

The effects of population age and metallicity drifts with redshift may also cause changes in the luminosities. These effects can be tested in the local Universe by studying the possible dependence of SN Ia properties on host-galaxy type. Such dependence was indeed found [22] although it is fully accounted for by the lightcurve shape–luminosity relation. **Paper B** presents a direct test for a possible bias in the cosmology fit depending on the host-galaxy type, as a surrogate for progenitor age and metallicity. The results of that test show no significant difference in the cosmology fits based on SNe residing in early-type and late-type galaxies. This provides strong evidence that, even if the intrinsic brightness of SNe Ia may depend on metallicity or age, the lightcurve shape correction can account for such dependence.

K-Corrections and Colors

In Section 3.3, we have seen that the computation of the K-correction term in Eqn 3.5 presents some difficulties. Its calculation requires accurate SN spectrophotometry and calibration of the filter system used (which determines the zero points C_i and C_j in Eqn. 3.3). More importantly, it requires the use of an adequate SN spectrum template for the corresponding epoch of the observation to be corrected. Although the spectra of SNe Ia are relatively homogeneous, the study of possible peculiarities that might introduce differences in the K-corrections is important. Analyses such as the one presented in **Paper III** for `SN 1999aa`, in **Paper H** for `SN 1999ac`, or in **Paper D** for `SN 2002bo`, allow a more detailed knowledge of spectral differences and the choice of the appropriate subset of template SN spectra.

The uncertainties are enhanced when the observations involve the rest-frame U-band, where the amount of data from nearby SNe is significantly lower than in other bands. In **Paper A**, a test is done to determine the effect on the K-corrections, and therefore on the cosmology fit, of varying the $(U-B)$ color of the templates. The effect is found to be very mild, with negligible variations on Ω_M for a flat Universe.

However, differences in the adopted intrinsic $(U-B)$ color have a much greater effect on the computed color excesses. This affects the cosmology fits done with direct host-galaxy extinction corrections. The effect is estimated in **Paper A** to produce an uncertainty of 0.07 in Ω_M for a flat Universe.

Light Propagation

Even if SNe Ia are proven to be accurate distance indicators (as standardized candles), the possibility remains that, in its way to the Earth, the radiation they

emit suffers the effect of some intervening agent not considered in the correction of the observed magnitudes. Again it should be noted that a bias would be introduced in the cosmology fit only if the effect were redshift-dependent. The following considers two possible sources of systematic errors originated in the host-galaxy medium and in the intergalactic medium (IGM). These are the possible evolution of dust properties and the effect of gravitational lensing. Other possible agents suggested to mimic the the effect of an accelerated expansion on the measured magnitudes are "gray" dust (i.e., a homogeneously distributed absorbing component in the IGM with weak dependence on wavelength), and axions (through axion-photon oscillations in the IGM), although they are believed to introduce an insignificant bias.

Dust Properties. The possibility that the dust properties evolve with redshift may introduce systematic changes in the extinction law (in particular, in the value of the total-to-selective extinction coefficient, e.g., R_B). This effect would produce a variation in the cosmology fit only when extinction corrections are applied. The effect of varying R_B with z is simulated in **Paper A** and an uncertainty of 0.04 is found for Ω_M in a flat Universe. The use of I-band lightcurves to build the Hubble diagram may prove more convenient since extinction is less significant at those wavelengths. Such an attempt is presented in **Paper F**.

Gravitational Lensing. As light travels from the SN to the Earth, it is subject to be gravitationally lensed due to fluctuations in the distribution of matter. Most commonly, the light path traverses under-dense regions and the SN is therefore de-magnified. Occasionally, an over-dense region is encountered and the object appears magnified. The distribution of observed brightnesses is thus skewed, with a vast majority of objects appearing fainter than than in the case of homogeneous gravitational potential, and a few objects being highly magnified. In sum, the modal brightness is decreased, the dispersion is increased, and the mean is unchanged. For a limited sample of SNe, the distribution may not be well reproduced, and a bias may occur. The size of the effect depends on the fraction of compact objects acting as lenses, as modeled by Amanullah et al. [4]. The potential bias introduced in the cosmology fit increases with the redshift of the SNe in the sample. For the data set presented in **Paper A**, this effect was simulated using the `SNOC` package [19], and found to introduce an uncertainty of 0.01 in the value of Ω_M for a flat Universe.

Chapter 4

Observation of Type Ia Supernova Spectra

4.1 The Spring 1999 Nearby Supernova Campaign

Why Going Back for Nearby SNe

Chapter 3 presents the exciting result of an accelerated expansion of the Universe, supported by type Ia supernova (SN Ia) measurements. The observation of distant SNe Ia ($z > 0.3$) is essential to distinguish among the different cosmological models (See Figure 3.6 and its discussion in Section 3.3). However, the whole technique relies on our knowledge of nearby SNe. As seen in Section 3.1, the use of SNe Ia as standardized candles is based on the correlation between lightcurve shape properties and peak luminosity, which was found using data of SNe in the Hubble flow ($0.01 < z < 0.1$). The precision with which Ω_M and Ω_Λ can be determined depends in part on the calibration of the low-z SNe through the precision in the fitted nuisance parameter $\mathcal{M}$. Furthermore, as described in Section 3.5, a number of systematic effects may play an important role in the uncertainties of Ω_M and Ω_Λ, especially as SN Ia data begin to accumulate and statistical uncertainties are reduced. Our knowledge of the nature of SN Ia progenitors and explosion mechanism is still limited. Therefore, the study of systematic effects is to a great extent dependent on observational data. Nearby SNe are easier to observe and explore in detail as they brighten and fade. Both the empirical calibration of SN Ia luminosity and the understanding of the physics involved in SN explosions require the best possible and most complete set of data. Finally, these studies need to be carried out on the sample of high-z SNe Ia in order to fully assess the importance of possible systematic effects in the estimation of the cosmological parameters.

With the purpose of addressing these issues, during the Spring of 1999, the Supernova Cosmology Project (SCP) coordinated an observing campaign in which 19 low-z SNe Ia were discovered and followed up [1, 48]. Both photometry and spectroscopy observations were carried out to obtain $UBVRI$ lightcurves and spectral time series. The importance of this new data-set lies on the large amount of SN Ia spectra, obtained with a systematic and quite homogeneous observational technique. A large fraction of the work for this thesis is related to the observation, reduction and analysis of these spectra. The study of the spectroscopic data was done with the twofold aim of addressing the homogeneity of SN Ia properties in detail, and exploring new means of standardizing SN Ia distance measurements through the correlation of spectral parameters with peak luminosity. Also of interest is the use of these low-z SN Ia data to improve the accuracy with which K-corrections can be computed. The photometry data collected would also serve to study certain SN Ia properties which may be related to environmental or evolutionary effects, such as lightcurve rise times, U-band lightcurve properties, color indices and their relation to extinction estimation, dependence on host-galaxy type, etc. Part of this data-set was used to determine the rate of SN Ia explosions in the local Universe ($z \sim 0.1$), as presented in **Paper C**.

Observations

The observations of the Spring 1999 Nearby Supernova Campaign (for short, the "Spring '99" campaign) can be divided in three parts: the *search*, the *follow-up* and the *reference* observations.

The search for SNe involved the collaboration of several observing teams, with the coordination of the SCP: the EROS, the MOSAIC/CTIO Team, the SpaceWatch, the NEAT, the QUEST and the El Roble Supernova Search. Each of these search teams worked with different scientific goals, including SN discovery and asteroid tracking, but used similar search techniques. In short, the search consisted of repeated observations of certain fields of the sky and subtraction of subsequent images to find residuals due to variable objects. The size and location of the search fields, the instrumentation used and the frequency of the observations varied among the teams. Typically, the size of the fields covered by each team ranged from a few to several hundred square degrees. A total of more than 1300 square degrees of the sky were monitored during three months. The search was done on fields lying outside the Galactic plane in order to reduce the contamination from nearby objects and avoid regions of high Galactic extinction. The SN candidates were chosen among the brightening objects in order to preselect those discovered at early phases. Figure 4.1 shows an image of one of the discovered SNe; the SN is clearly seen on one side of its host galaxy, located at a redshift of 0.05. The proper motion of the objects found was checked in order to discard possible asteroid detections. The amount of the brightening and the position of the object with respect to its possible host galaxy were considered in

order to discard active galaxy nuclei and other undesired variable objects. Finally, the preselected discoveries were screened with spectroscopic observations in order to secure their identification. The spectra allowed the classification of the SNe found and thus were crucial for the planning of follow-up observations.

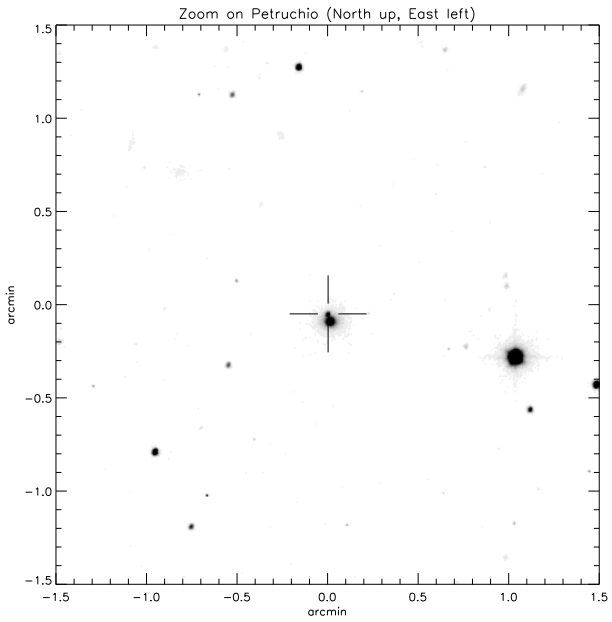

Figure 4.1: Image of the discovery of `SN 1999av` at $z = 0.05$. North is up and East is to the left. The SN, marked with a cross, is clearly seen on one side of its host galaxy.

The search delivered 19 SNe Ia at $z < 0.2$ discovered before or around maximum light, which were finally followed, and a similar amount of all types, including SNe Ia that were already in the fading phase and were therefore not useful for the purposes of the campaign. The discoveries were made public to the astronomical community through a number of circulars to the IAU: 7109, 7117, 7122, 7125, 7128, 7130, 7131, 7133, 7134, 7136, and 7138.

The selected SNe Ia were extensively followed with optical direct imaging and spectroscopy. The direct imaging observations consisted of $UBVRI$ photome-

try obtained at 12 different telescopes in a three month period. The resulting sampling of the lightcurves ranged from ∼3 days to ∼1 week, depending on the brightness of the SNe. During the same period, the spectroscopy observations were obtained in more than 30 observing nights at 9 different telescopes. This added to the classification spectra a time series of varying coverage, depending on the brightness of the SNe.

The final stage of the campaign, the reference part, was accomplished approximately one year after the search was done. At this stage, new images and spectra were taken at the locations where the SNe had been discovered. By that time, the SNe had faded enough for the new observations to show only the background host galaxy signal. Both direct images and spectra were used to subtract the contribution of the host-galaxy flux from the follow-up observations. This procedure is of outmost importance for achieving accurate lightcurves and spectra, especially in the cases of the most distant SNe in the sample which could not be spatially resolved from their host galaxies. Furthermore, the reference observations provided information about the environment in which each SN went off. This information can be used in the study of possible progenitor age, mass or metallicity effects on SN properties. This part of the campaign required less observational effort because only one data point per SN (both in photometry and spectroscopy) was sufficient. Also, the objects observed at this stage were no longer variable, which made the scheduling of observing time easier and the chances of success less subject to technical or weather conditions.

The following sections refer to the spectroscopy part of the campaign, to which I dedicated great part of my work as a graduate student. The set of spectra obtained was used to carry out a series of studies which are presented in Chapter 5.

Spectra Reduction

The vast amount of spectra obtained during the Spring '99 campaign, involving several telescopes and different observers, made their reduction a long-term task which justified the development of a thorough data treatment method which is described in **Paper I**. This method aims at the preparation of SN spectra in particular but also addresses some general issues of spectroscopy observation and reduction. The final results are fully calibrated spectra with associated statistical and systematic uncertainties. The method was developed after the Spring '99 data had been taken and thus encountered some limitations in its applicability. Even though the observations were coordinated and planned to follow certain common prescriptions, there was some degree of heterogeneity arising from instrumentation and weather limitations, and from the different level of experience among the observers.

With the purpose of collecting thorough information about the observations and reduction steps, a database was created using `MySQL`. The database also contains a description of every SN observed and instrument used. For each ob-

serving night, a reduction log is available with information about intermediate product images and calibration images. Information about the way each reduction step was done (parameters of fits, their precision, explanatory graphs, etc) is also kept. Figures 4.2 and 4.3 show an example of a reduction log as it appears on an Internet browser. The availability of the database is very helpful in the analysis of the spectra since it allows to track the source of possible problems through the whole reduction process.

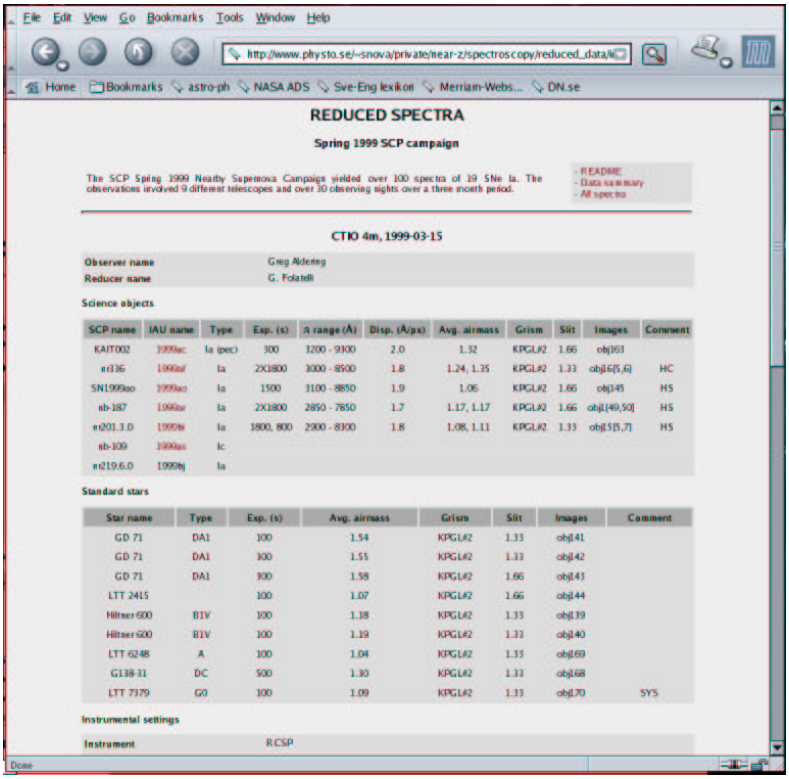

Figure 4.2: A reduction log (*first part*) containing summary tables of the SN and standard star observations. Courtesy: Rahman Amanullah

Table 1 in **Paper I** provides basic information about the instrumental settings used to obtain the follow-up Spring '99 spectra. The following description presents some additional facts of the reduction process. A summary of the main reduction steps is given in Table 4.1. Most of these steps were done using standard routines provided by the image reduction package `IRAF`[1]. The rest of the

[1] `IRAF` is distributed by the National Optical Astronomy Observatories, which are oper-

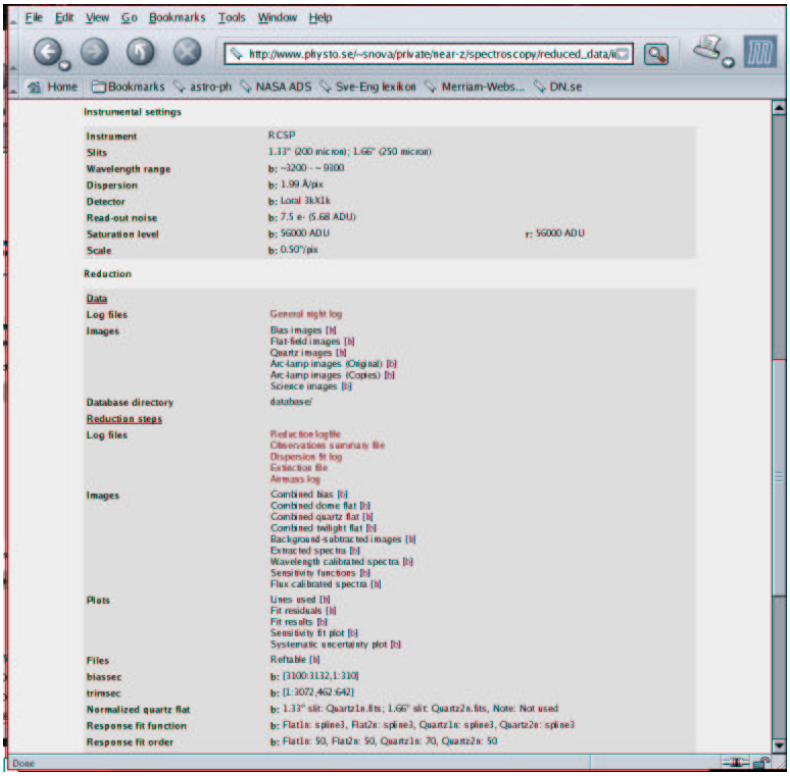

Figure 4.3: A reduction log (*second part*) containing the lists of science and calibrations images, useful reduction information and links to the archived data. Courtesy: Rahman Amanullah

steps were done by self-made routines in the form of `IRAF` or `IDL` scripts, or `FORTRAN` programs.

Background subtraction and spectrum extraction. A series of tests were performed in search for an optimal method of background subtraction and signal extraction from the SN spectra. Several interplaying factors were considered when defining the background level and extraction aperture: the minimization of the host-galaxy contamination, the accuracy of the background fit, the optimization of the signal-to-noise ratio, and the simplicity of the method. Two background subtraction methods, differing in the selection of the fitting range, were compared. The first method (I) based the fit of a low order cubic spline function on the whole spatial range, whereas the second method (II) used the region in the vicinity of the object to fit a low-order polynomial. The accuracy of both subtractions was tested by comparing the background spectrum fit on the location of the SN with a reference background taken from the original image, off the location of the SN[2]. Special attention was put on the removal of fringing patterns and sky lines. In addition, extraction apertures of different size were tested. The results of the tests depended on the relative brightness and apparent location of the SN with respect to the host galaxy. In general, the residual fringes and sky lines were not significant, with the exception of some spectra from the NOT and the Lick 3m telescope.

Figure 4.4 shows three distinct cases which were considered separately. In case **(a)**, the SN is well separated from the core of the host galaxy. Both background subtraction methods produced comparable results. Method I was finally used due to its more straightforward applicability, without the need to select the fitting region in each case. The extraction aperture limits were chosen where the SN signal blended into the background noise to optimize the signal-to-noise ratio. In case **(b)**, the SN is located on the core of the host galaxy though it can be resolved on the extended host-galaxy background. In general, method II produced unreliable galaxy background subtractions due to the variation of the relative brightness between SN and host galaxy as a function of wavelength. Method I was therefore used, which did not subtract the core of the host galaxy. Because of that, the aperture size was reduced to avoid the more contaminated wings of the SN profile. Care was taken so that the trace of the aperture along the dispersion direction, which follows the position of the profile peak, did not "jump" from the SN to the host galaxy, especially on the red part of the spectrum, where the host galaxy usually becomes brighter. The spectra extracted in this way were affected by a certain degree of host-galaxy contamination. The correction of this contamination proved to be reliable at a final stage, with the use of the reference spectra, as described below. A first estimate of the contamination level could be drawn from the relative fluxes of SN and host galaxy

ated by the Association of Universities for Research in Astronomy, Inc., under cooperative agreement with the National Science Foundation. `http://iraf.noao.edu`.

[2] An offset of 4×FWHM was typically used.

Table 4.1: Main spectra reduction steps.

Two-dimensional images	
Reduction Step[a]	Details/ routine used[b]
Average of bias images	`zerocombine`
Overscan subtraction	`ccdproc`
(Dark current correction)	`ccdproc`
Trimming	`ccdproc`
Bias subtraction	`ccdproc`
Flat-field combination	`flatcombine`
Flat-field normalization	`response`
Flat-field division	`ccdproc`
Check of illumination	`implot` on the twilight spectra
(Illumination correction)	`illumination`
Sky background subtraction	`background`
Exrtraction of 1-D spectra	`apall`
One-dimensional images	
Reduction Step[a]	Details/ routine used[b]
Dispersion function fit	`identify`, `reidentify`
Wavelength calibration	`dispcor`
Check of wavelength calibration	`splot` to measure the sky lines
Effective airmass calculation	`setairmass`
Sensitivity function fit	`standard`, `sensfunc`
Atmospheric extinction correction	`sensfunc`, `calibrate`
Flux calibration	`calibrate`
Addition of the background contribution to the sigma spectrum	`IRAF` script
Spectra combination	`IDL` script (See **Paper I**)
Milky Way extinction correction	`FORTRAN` program (See **Paper I**)

[a] The main reduction steps are listed. Entries in parentheses correspond to to procedures that were carried out only when needed and when the suitable calibration data were available.

[b] Routine names correspond to standard `IRAF` routines.

inside the selected aperture. In case **(c)**, corresponding to a more distant SN than in the previous cases, the SN and host-galaxy signals are barely resolved. The background subtraction was done using method I for the same reasons as in case **(a)**. A narrow aperture was used for the extraction in order to reduce the contamination from the host galaxy. A priori, the level of contamination was uncertain in these cases and had to be determined from the subtraction of the reference spectra. The situation worsened as the SN faded with time causing that some of the extracted spectra were dominated by the host galaxy.

In all cases the extractions were done using a variance-weighed algorithm [30] implemented in the routine `apall` of `IRAF`. The weighed extractions allows to reduce the noise by setting lower weights on the wings, and reject bad pixels and cosmic rays. The procedure also produced an estimate of the measurement uncertainties considering Poisson-distributed errors on the signal and instrumental *read-out* noise. Since the background signal was subtracted before the extraction, its contribution to the uncertainties had to be added at this stage.

A limitation of the extraction procedure arises from the use of an aperture of fixed size along the dispersion direction. The dependence of seeing as a function of wavelength, may introduce differential light losses which would affect the overall shape of the extracted spectrum both in the cases of standard star and supernova spectra. This effect has implications on the estimation of systematic uncertainties which is addressed below.

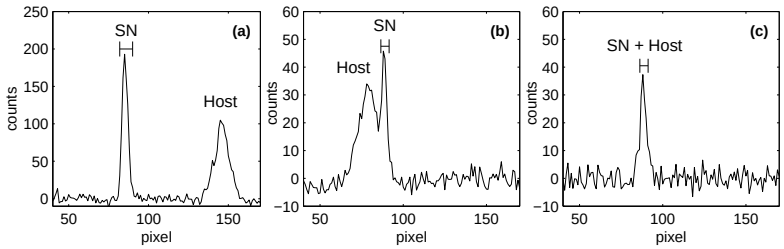

Figure 4.4: Three different cases of background subtraction and extraction. The three panels show the average of 20 lines along the dispersion direction from two dimensional spectra where an overall subtraction of the background level was applied. Case **(a)**: The SN is well separated from the core of the host galaxy. A wide aperture can be used. This image corresponds to a 500 s exposure of `SN 1999aa` ($z = 0.0014$) taken at the CTIO 4m telescope on March 24th 1999 (epoch = 28 d). Case **(b)**: The SN is resolved on its host galaxy. A subtraction of the galaxy background is not reliable. A narrow aperture is used. This image corresponds to a 1800 s exposure of `SN 1999bk` ($z = 0.096$), on the same night as above (epoch = 10 d). Case **(c)**: SN and host are barely resolved. A narrow aperture is used. The image corresponds to a 1800 s exposure of `SN 1999af` ($z = 0.097$), on the same night as above (epoch = 27 d).

Wavelength calibration. The wavelength calibration of the extracted spectra was performed with the use of arc-lamp exposures. An example of a He-Ne-Ar arc-lamp spectrum with the identified lines marked is shown in Figure 4.5. The lines were used to fit a dispersion function that converts from pixel coordinates to wavelength. The results were tested using the position of sky lines on background sky spectra prepared for the purpose. Table 4.2 summarizes the information on the wavelength calibration and their tests for each night and instrumental setting (see the caption of the table for an explanation of the column contents). In the cases where significant systematic deviations were found, a correction to the dispersion solution was applied, in the form of a constant wavelength shift.

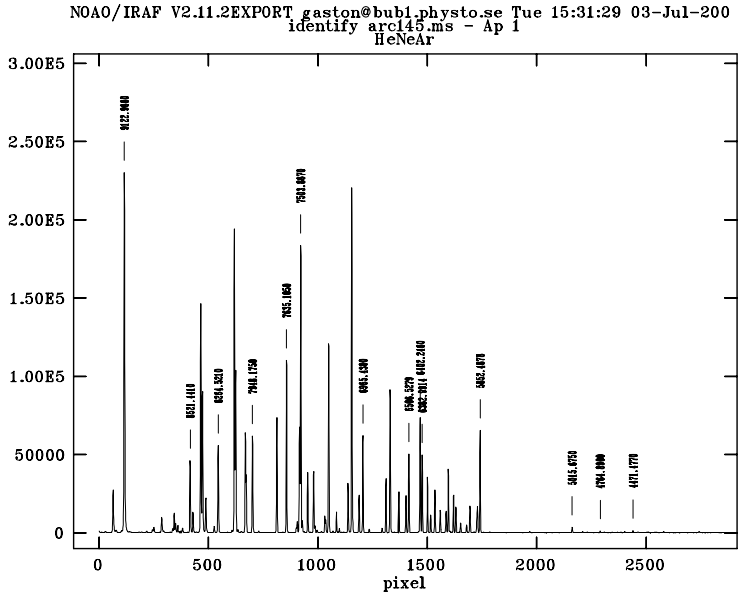

Figure 4.5: An example of a He-Ne-Ar arc-lamp spectrum taken using the CTIO 4m telescope and the R-C spectrograph. The exposure time is 20 s. The wavelength values (in Å) for the identified lines are marked.

Flux calibration. The flux calibration was performed using standard star observations obtained on each night. Table 4.3 shows some details about those observations. The standard stars used were calibrated in [9, 10, 25, 24, 44, 51, 74, 78]. For each telescope and night, the name and spectral type of the standard star is given along with the exposure time, effective airmass (X), and instrumental setup (divided in "blue" and "red" channels). The effective airmass

Table 4.2: Wavelength calibration uncertainties

Telescope (1)	Observing date (2)	Setup (3)	Dispersion (Åpix) (4)	Number of lines (5)	Fit rms (Å) (6)	Deviation of sky lines (Å) (7)
APO 3.5m	1999-02-17	blue	6.25	10	0.53, 0.49	<2
		red	7.0	23	0.33, 0.34	<2
	1999-02-26	blue	6.25	3, 9	0.15	<2
		red	7.0	19, 17	0.24, 0.34	<2
	1999-03-10	blue	6.25	12	0.69	<2
		red	7.0	15	0.30	<2
	1999-04-06	blue	6.25	12, 11	0.42, 0.36	<2
		red	7.0	18, 14	0.18, 0.20	<2
	1999-04-17	blue	6.25	7	0.31	<2
		red	7.0	13	0.20	<2
CTIO 4m	1999-03-15	blue	1.99	33, 17	0.07, 0.09	<1
				16	0.08	<1
	1999-03-17	blue	1.99	36, 39	0.06, 0.07	<1
	1999-03-21	blue	1.99	45	0.087	<1
	1999-03-24	blue	1.98	34, 33	0.123, 0.126	up to 13
		red	2.00	13, 26	0.094, 0.012	up to 15
	1999-03-29	blue	1.99	34	0.112	up to 11
		red	2.00	29	0.086	up to 13
ESO 3.6m	1999-03-13	blue	4.09	7	0.50	<2
	1999-04-10	blue	4.1	13, 13	0.59, 0.56	<2
		red	4.2	14, 14	0.13, 0.14	<2
	1999-04-15	blue	4.09	7	0.45	<2
		red	4.24	14	0.14	<2
	1999-04-18	blue	4.1	13	0.63	<2
	1999-04-21	blue	4.1	13	0.61	<2
		red	4.2	14	0.12	<2
KPNO 4m	1999-04-06	blue	5.5	34, 32	0.26, 0.39	<2
Lick 3m	1999-02-23	blue	1.8	15	0.12	<1
		red	4.6	17	0.26	<1
	1999-04-13	blue	1.85	13, 16	0.09, 0.18	<1
		red	4.6	12, 17	0.16, 0.13	<1
	1999-04-24	blue	1.8	14	0.23	<1
		red	2.3	8, 15	0.13, 0.05	<1
MDM 2.4m	1999-03-01	blue	5.4	0.14	16	<2
	1999-03-02	blue	5.4	0.13	16	<2
	1999-03-04	blue	5.4	16, 7	0.128, 0.211	<2
NOT	1999-02-13	blue	6.0	10	0.69	<2
		red	6.2	15	0.80	<2
	1999-02-21	blue	5.9	9	0.56	up to 15
		red	6.2	13	1.33	up to 10
	1999-03-14	blue	5.95	9	0.2	<2
	1999-03-15	blue	5.93	17	1.2	<2
		red	6.15	16	1.3	<2
	1999-03-23	blue	5.93	17	1.0	<2
		red	6.18	10	1.3	<2

Columns: (1) Telescope name; (2) Observing night; (3) Instrumental setup, divided in "blue" and "red" according to the wavelength range covered; (4) Approximate dispersion on the detector (the typical resolution was <2 to 3 pixels); (5) Number of arc-lamp lines used in the dispersion fit (values for different arc-lamps are separated with commas); (6) Estimated rms of the dispersion fit (values for different arc-lamps are separated with commas); (7) Range of deviations measured on the position of sky lines.

X is computed as the mean over the exposure time of the instantaneous airmass values which are in turn determined by the zenith distance Z ($X(Z) \sim \sec(Z)$ + terms of higher order in $\sec(Z)$). The standard star observations were also used to estimate a systematic uncertainty in the final calibration, as described in **Paper I**. The standard star spectra selected to obtain these estimates are marked in the table.

The flux calibration was applied together with an atmospheric extinction correction. The values of airmass for both standard star and SN spectra, as well as mean extinction coefficients for each observing site were used to perform the correction. Figure 4.6 shows the distribution of effective airmass X for both SN and standard star spectra. These values are to be considered when studying the possible effect of *differential atmospheric refraction* (DAR) which may introduce wavelength-dependent light losses in long-slit spectra, as discussed in **Paper I** and in greater detail in [15]. For large airmasses (beyond $X \sim 1.5$), the effect of DAR can be sizable if care is not taken while performing the observations. The basic prescriptions for avoiding this effect are to align the slit at the parallactic angle (i.e., in the direction to the zenith), which depends on the position of the object in the sky, and to use a wider slit, at the expense of spectral resolution. About 15% of both SN and standard star spectra were taken at $X > 1.5$. In the case of the standard stars, the two prescriptions above were usually followed and thus the effect of DAR is under control. In the case of the SNe, the risk for the spectra with $X > 1.5$ to be affected by DAR are greater since the slit was usually aligned through the SN and the core of its host galaxy or some reference field star. The effect of DAR not only depends on the slit orientation and airmass, but also on the seeing conditions, the atmospheric conditions (pressure and temperature), the width of the slit used, and other technical details such as the pointing and tracking accuracy of the telescope, etc. A full modeling and correction of the effect is beyond the possibilities of this work. Furthermore, other systematic effects introduced, for example, by extracting the spectra with a fixed aperture size might also be present. It is difficult to disentangle the contribution from each of the possible systematic effects with the aim of correcting them separately. Instead, for the present data set, the correction of any inaccuracy in the spectral distribution was done with the use of photometry observations, as described in **Paper I**.

Table 4.3: Standard star observations of the Spring '99 follow-up campaign.

Telescope	Observing date	Standard star[a]	Spectral type	Exposure time (s)	X[b]	Setup[c]
APO 3.5m	1999-02-17	Feige 34	DO	10	1.018	b
		Feige 34	DO	10	1.018	r
		Feige 34⋆	DO	30	1.018	b
		Feige 34	DO	30	1.018	r
		HZ 43†	DA1	120	1.086	b
		HZ 43†	DA1	120	1.086	r
		BD+33d2642	B2IV	20	1.012	b
		BD+33d2642⋆	B2IV	20	1.012	r
		BD+33d2642	B2IV	40	1.011	b

Table 4.3: Standard star observations (continued)

Telescope	Observing date	Standard star[a]	Spectral type	Exposure time (s)	X[b]	Setup[c]
		BD+33d2642	B2IV	40	1.011	r
APO 3.5m	1999-02-26	HZ 43	DA1	120	1.17	b
		HZ 43	DA1	120	1.17	r
		HZ 43⋆	DA1	120	1.18	b
		HZ 43⋆	DA1	120	1.18	r
APO 3.5m	1999-03-10	G191-B2B	DA1	90	1.11	b
		G191-B2B	DA1	90	1.11	r
		G191-B2B⋆†	DA1	90	1.12	b
		G191-B2B⋆†	DA1	90	1.12	r
APO 3.5m	1999-04-06	GD 71⋆	DA1	180	1.22	b
		GD 71⋆	DA1	180	1.22	r
		GD 71	DA1	180	1.24	b
		GD 71	DA1	180	1.24	r
		Hiltner 600	B1V	60	1.26	b
		Hiltner 600	B1V	60	1.26	r
		Hiltner 600	B1V	30	1.27	b
		Hiltner 600	B1V	30	1.27	r
APO 3.5m	1999-04-17	G191-B2B	DA1	60	1.45	b
		G191-B2B	DA1	60	1.45	r
		G191-B2B	DA1	120	1.47	b
		G191-B2B	DA1	120	1.47	r
		GD 71	DA1	210	1.65	b
		GD 71	DA1	210	1.65	r
		Hiltner 600	B1V	30	1.46	b
		Hiltner 600⋆	B1V	30	1.46	r
		Hiltner 600	B1V	90	1.47	b
		Hiltner 600	B1V	90	1.47	r
CTIO 4m	1999-03-15	GD 71	DA1	100	1.54	b
		GD 71	DA1	300	1.55	b
		GD 71	DA1	300	1.58	b
		LTT 2415	–	100	1.07	b
		Hiltner 600	B1V	100	1.18	b
		Hiltner 600	B1V	100	1.19	b
		LTT 6248	A	100	1.04	b
		G138-31	DC	500	1.30	b
		LTT 7379⋆	G0	100	1.09	b
CTIO 4m	1999-03-17	LTT 3218	DA	60	1.06	b
		LTT 3218	DA	300	1.05	b
		LTT 3218	DA	120	1.05	b
		LTT 4364	C2	300	1.65	b
		LTT 4364⋆	C2	60	1.67	b
		LTT 6248	A	120	1.03	b
		LTT 6248	A	120	1.04	b
		LTT 7379	G0	120	1.09	b
		LTT 7379	G0	120	1.09	b
CTIO 4m	1999-03-21	GD 71	DA1	300	1.55	b
		LTT 2415	–	120	1.03	b
		LTT 2415	–	120	1.03	b
		Hiltner 600	B1V	120	1.18	b
		Hiltner 600	B1V	60	1.18	b
		CD-32d9927⋆†	A0	40	1.38	b
		BD+33d2642	B2IV	100	2.32	b
		BD+33d2642	B2IV	100	2.33	b
		BD+33d2642	B2IV	100	2.34	b
		EG 274	DA	120	1.04	b
		EG 274	DA	60	1.04	b
		G138-31	DC	500	1.32	b
		LTT 7379	G0	60	1.06	b
CTIO 4m	1999-03-24	GD 71	DA1	300	1.57	r
		GD 71⋆	DA1	300	1.59	b
		LTT 2415	–	120	1.04	b

Table 4.3: Standard star observations (continued)

Telescope	Observing date	Standard star[a]	Spectral type	Exposure time (s)	X[b]	Setup[c]
		LTT 2415	–	120	1.04	r
		Hiltner 600	B1V	60	1.18	r
		Hiltner 600	B1V	60	1.19	b
		BD+33d2642⋆	B2IV	100	2.42	r
		BD+33d2642	B2IV	100	2.44	b
		EG 274	DA	60	1.04	b
		EG 274	DA	60	1.04	r
		LTT 7379	G0	60	1.06	r
		LTT 7379	G0	60	1.06	b
CTIO 4m	1999-03-29	CD-32d9927	A0	40	1.46	b
		CD-32d9927	A0	40	1.47	b
		BD+33d2642⋆	B2IV	100	2.43	r
		BD+33d2642	B2IV	100	2.45	r
		BD+33d2642⋆	B2IV	75	2.48	b
		BD+33d2642	B2IV	75	2.50	b
		EG 274	DA	60	1.04	b
		EG 274	DA	60	1.04	b
		EG 274	DA	60	1.04	r
		EG 274	DA	60	1.05	r
		LTT 7379	G0	60	1.05	r
		LTT 7379	G0	60	1.05	r
		LTT 7379	G0	60	1.05	b
		LTT 7379	G0	60	1.05	b
ESO 3.6m	1999-03-13	LTT 4816	DA	120	1.28	b
		LTT 4816	DA	120	1.28	b
		EG 274	DA	30	1.03	b
		EG 274	DA	30	1.02	b
		LTT 7379⋆	G0	10	1.12	b
		LTT 7379	G0	10	1.12	b
ESO 3.6m	1999-04-10	LTT 3218⋆	DA	60	1.01	b
		LTT 3218	DA	60	1.01	r
		EG 274	DA	30	1.12	b
		EG 274⋆	DA	30	1.12	r
		LTT 7379	G0	60	1.04	b
		LTT 7379	G0	60	1.04	r
		LDS 749B	DB4	120	1.56	r
		LDS 749B	DB4	120	1.54	b
		LDS 749B	DB4	180	1.47	r
		LDS 749B	DB4	120	1.45	b
ESO 3.6m	1999-04-15	LTT 3218	DA	60	1.01	b
		LTT 3218⋆	DA	60	1.01	r
		CD-32d9927	A0	15	1.65	b
		CD-32d9927	A0	15	1.66	r
		LTT 6248	A	45	1.24	b
		LTT 6248	A	45	1.25	r
		EG 274	DA	60	1.08	b
		EG 274	DA	60	1.09	r
		G138-31⋆	DC	300	1.37	b
		G138-31	DC	300	1.38	r
		NGC 7293	V.Hot	180	1.62	b
		NGC 7293	V.Hot	300	1.58	r
ESO 3.6m	1999-04-18	LTT 3218⋆	DA	60	1.00	b
		LTT 4364	C2	60	1.35	b
ESO 3.6m	1999-04-21	LTT 3218	DA	60	1.00	r
		LTT 3218	DA	60	1.00	b
		LTT 4816	DA	120	1.09	b
		LTT 4816	DA	120	1.10	r
		CD-32d9927	A0	15	1.83	b
		CD-32d9927⋆	A0	15	1.84	r
		LTT 6248	A	45	1.35	b
		LTT 6248	A	60	1.36	r

Table 4.3: Standard star observations (continued)

Telescope	Observing date	Standard star[a]	Spectral type	Exposure time (s)	X[b]	Setup[c]
		EG 274	DA	60	1.13	b
		EG 274	DA	30	1.14	b
		EG 274	DA	60	1.14	r
		G138-31⋆	DC	300	1.43	b
		G138-31	DC	300	1.46	r
		NGC 7293	V.Hot	180	1.44	b
		NGC 7293	V.Hot	300	1.41	r
KPNO 4m	1999-04-06	GD 71	DA1	180	1.29	b
		Hiltner 600⋆	B1V	60	1.25	b
		BD+33d2642	B2IV	20	1.08	b
		BD+33d2642†	B2IV	20	1.08	r
		G138-31	DC	300	1.15	b
		BD+28d4211	Op	120	1.51	b
		BD+25d4655	O	60	1.57	b
Lick 3m	1999-02-23	GD 71	DA1	120	1.08	b
		GD 71	DA1	120	1.08	r
Lick 3m	1999-04-13	Hiltner 600	B1V	120	1.48	b
		Hiltner 600	B1V	120	1.48	r
		Hiltner 600	B1V	120	1.50	b
		Hiltner 600	B1V	120	1.50	r
		GD 108⋆	sdB	300	1.44	b
		GD 108	sdB	300	1.44	r
		BD+33d2642	B2IV	200	1.04	b
		BD+33d2642	B2IV	200	1.04	r
		G138-31	DC	900	1.16	b
		G138-31	DC	900	1.16	r
Lick 3m	1999-04-24	Hiltner 600	B1V	200	1.67	b
		Hiltner 600	B1V	200	1.67	r
		GD 108	sdB	500	1.41	b
		GD 108	sdB	500	1.41	r
		BD+33d2642	B2IV	200	1.13	b
		BD+33d2642	B2IV	200	1.13	r
		BD+28d4211	Op	200	1.41	b
		BD+28d4211	Op	200	1.41	r
MDM 2.4m	1999-03-01	GD 71⋆	DA1	300	1.10	b
		Hiltner 600	B1V	120	1.15	b
MDM 2.4m	1999-03-02	G191-B2B⋆	DA1	300	1.11	b
		GD 71	DA1	300	1.04	b
		Hiltner 600	B1V	120	1.17	b
		GD 153	DA1	300	1.02	b
MDM 2.4m	1999-03-04	GD 71†	DA1	200	1.00	b
		BD+33d2642⋆	B2IV	120	1.02	b
NOT	1999-02-13	GD 71⋆	DA1	60	1.06	b
		GD 71	DA1	120	1.06	b
		GD 71⋆	DA1	120	1.06	r
		HZ 44	sdO	30	1.01	b
		HZ 44	sdO	60	1.01	b
		HZ 44	sdO	60	1.02	r
NOT	1999-02-14	HZ 44⋆	sdO	30	1.10	b
NOT	1999-02-21	HR 4468	B9.5V	1	1.29	b
		HR 4468	B9.5V	1	1.29	b
NOT	1999-03-15	GD 71	DA1	60	1.07	b
		GD 71⋆	DA1	120	1.07	b
		GD 71⋆	DA1	120	1.08	r
		HZ 43	DA1	120	1.39	b
		HZ 43	DA1	120	1.43	b
		HZ 43	DA1	120	1.40	r
		HZ 43	DA1	120	1.42	r
NOT	1999-03-23	Feige 34⋆	DO	120	1.04	b
		Feige 34⋆	DO	120	1.04	r

Table 4.3: Standard star observations (continued)

Telescope	Observing date	Standard star[a]	Spectral type	Exposure time (s)	X[b]	Setup[c]

[a] Standard stars from [51, 44, 78, 25, 24, 9, 74, 10].
When marked with a "⋆", the spectrum was used to compute the systematic uncertainty of the corresponding night and instrumental setup.
A "†" means that the spectrum was rejected because of some failure (saturation, missed target, etc.).
[b] Effective airmass.
[c] Instrumental setup: "b" covering the blue part of the spectrum; "r" covering the red part.

The Observed Spectra

The information about the 19 SNe Ia of the Spring '99 campaign is summarized in Table 4.4. Figure 4.7 shows the redshift and epoch distribution of the sample. The values of z were obtained, when possible, from narrow host-galaxy features. In those cases, the precision in z can be considered to be of $\Delta z = 0.001$. Otherwise, the SN features were used to determine the redshift. Since the SN features are broadened by the expansion, the uncertainties were generally of $\Delta z = 0.01$. The epochs are expressed in days since the time of maximum B light. Preliminary lightcurves, when available, were used to determine the time of maximum light with an accuracy better than 1 day. When the lightcurves were not well constrained, the dating was based on spectral shape comparisons with well dated SNe. The epochs based on spectral dating are accurate within $\sim$2 to 3 days.

For each observing night, individual exposures of the same SN obtained with a given instrumental setting were combined after reduction. The combination procedure is described in **Paper I**. The combined spectra were corrected for Milky Way extinction, following the extinction law in [13]. A standard value of the total-to-selective absorption coefficient $R_V = 3.1$ was used, and values of A_V in the direction to each SN from [71]. The corresponding color excesses $E(B-V)$ are listed in Table 4.4.

The resulting spectra for the followed-up SNe Ia of the Spring '99 campaign are listed in Table 2 of **Paper I**, with the exception of `SN 1999by` which was observed exclusively at the Lick 1m telescope and the data reduced by the Berkeley group of the SCP. As seen in Table 1 of **Paper I**, in many cases, on a given night, spectra of the same SN were obtained with two different instrumental settings in order to cover the blue and the red ends of the spectrum. At the ESO 3.6m telescope and the NOT, this was done by using different grisms or gratings or by changing their orientation with respect to the detector. At the CTIO 4m telescope, order-blocking filters were used to avoid the effect of second order contamination, yielding spectra with different wavelength coverage. At the APO 3.5m and Lick 3m telescopes, the use of channel splitters allowed to observe the blue and red parts of the spectrum simultaneously. These "blue" and "red" spectra were compared to test the accuracy of the reduction in the overlapping wavelength regions. The size of the overlapping regions varied among the different telescopes, as can be seen in column 12 of Table 2 in **Paper I**. In

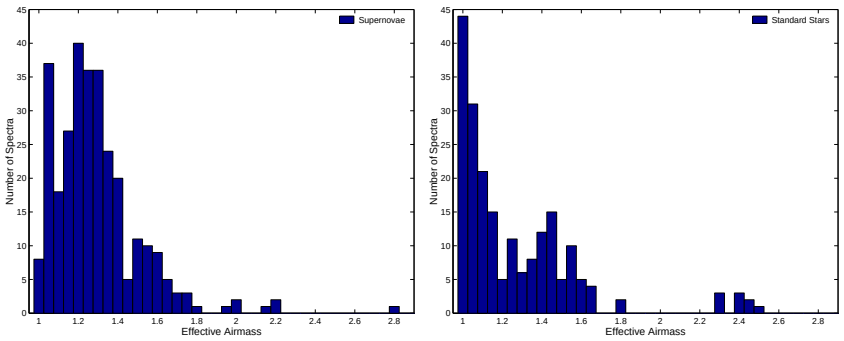

Figure 4.6: The effective airmass (X) distribution for the follow-up Spring '99 spectroscopy campaign. *Left-hand panel*: SN spectra. From a total of 300 exposures, 15% were taken at $X > 1.5$; the median of the distribution is 1.28. *Right-hand panel*: Standard stars. From a total of 203 exposures, 16% were taken at $X > 1.5$; the median of the distribution is 1.17.

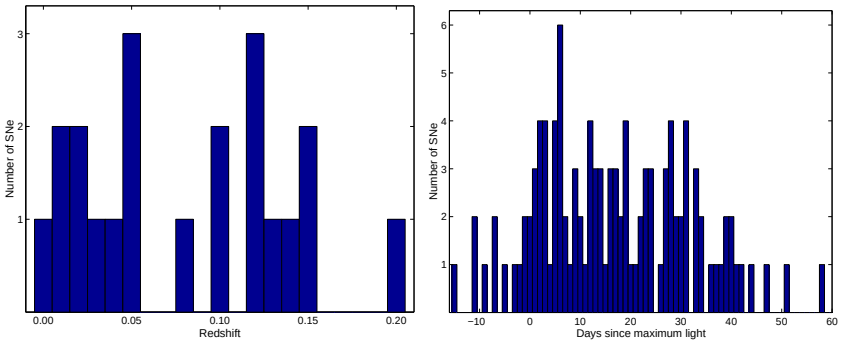

Figure 4.7: *Left-hand panel*: Redshift distribution of the 19 SNe Ia discovered and followed during the Spring '99 campaign. *Right-hand panel*: Epoch distribution of the follow-up spectra corresponding to those SNe Ia.

Table 4.4: The 19 followed-up Spring '99 SNe Ia.

SN Name	z	E($B-V$) (MW)	Date of max.[a]	Host Galaxy	Host Type[b]
1999aa	0.0144	0.040	1999-02-24	NGC 2595	SAB(rs)c
1999ac	0.0095	0.046	1999-03-13	NGC 6063	Scd
1999af	0.097	0.029	1999-02-22	Anon.	Sa/I0pec:
1999ao	0.054	0.065	1999-03-10:	Anon.	Sa:
1999ar	0.15	0.031	1999-03-08	Anon.	Sab:
1999at	0.027	0.029	···	Anon.	E/S0
1999au	0.124	0.032	1999-03-02	Anon.	Sb:
1999av	0.05	0.031	1999-03-08	Anon.	E/S0
1999aw	0.038	0.032	1999-03-12	Anon.	···
1999be	0.019	0.047	1999-03-10:	Anon.	···
1999bf	0.2	0.022	···	Anon.	···
1999bh	0.0172	0.015	···	NGC 3435	Sb
1999bi	0.123	0.027	1999-03-08	Anon.	Sb:
1999bk	0.096	0.027	1999-03-13	Anon.	E/S0
1999bm	0.143	0.024	1999-03-18:	Anon.	Sb:
1999bn	0.129	0.059	1999-03-21	Anon.	Sb:
1999bp	0.077	0.034	1999-03-23	Anon.	Sb:
1999bq	0.149	0.043	1999-03-20	Anon.	E/S0
1999by	0.0021	0.016	1999-05-09	NGC 2841	SA(r)b

[a] Dates followed by a colon are based on spectral dating (uncertainties ~ 2 days).

[b] Hubble type of the host galaxy. Types followed by a colon are based on spectral classification, following [34]. The rest are taken from NED (The NASA/IPAC Extragalactic Database (NED) is operated by the Jet Propulsion Laboratory, California Institute of Technology, under contract with the National Aeronautics and Space Administration).

general, blue and red spectra agreed well, considering the systematic uncertainties determined from the study of the standard star observations (see columns 9 and 11 in the same table).

Host-galaxy subtraction. Some of the spectra showed a certain level of contamination from host-galaxy flux, as expected from the background subtraction and extraction procedures described above. The contamination was noticeable from the overall shape of the continuum and from the presence of narrow features originated in the host galaxy. In order to obtain "clean" SN spectra, the contribution from the host galaxy was subtracted using the set of reference spectra, as described below. The reference spectra used are shown in Figures 4.8 to 4.10. The availability of these spectra of the actual host galaxies made the subtraction process more reliable than the use of template galaxy spectra of different types.

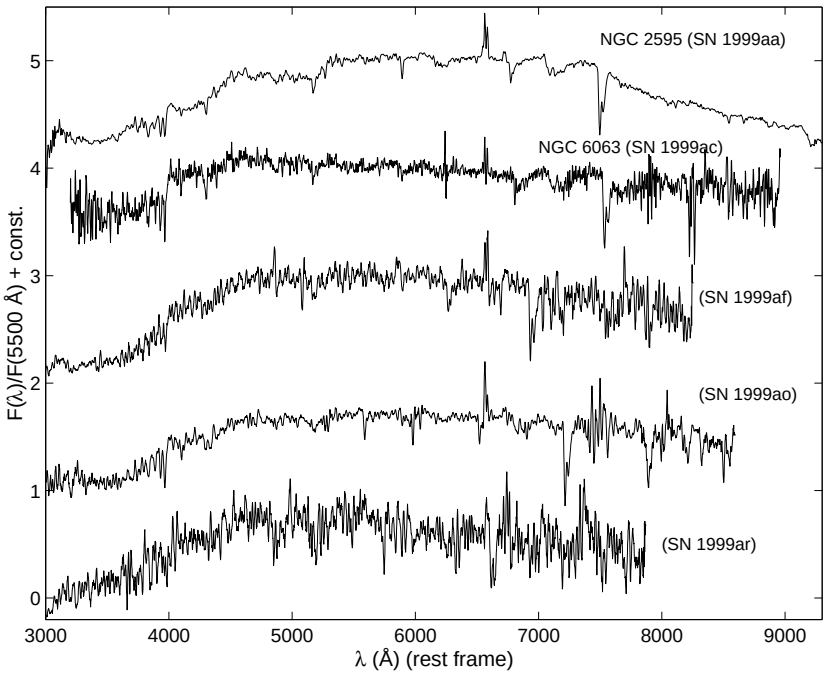

Figure 4.8: Reference spectra of the host galaxies corresponding to the indicated SNe.

As described in Section 4 of **Paper I**, a fitting procedure was used to find the amount of host-galaxy flux to subtract. The subtractions were fitted to high-quality template spectra of non-contaminated SNe at a similar epoch as the spectrum to be corrected. Nearly ninety published spectra of 8 very nearby

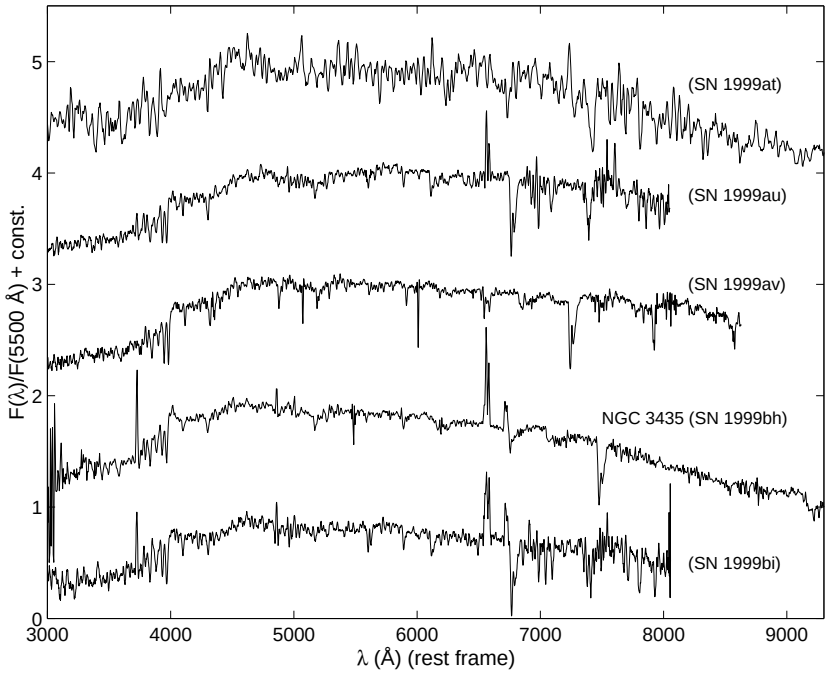

Figure 4.9: Reference spectra of the host galaxies corresponding to the indicated SNe.

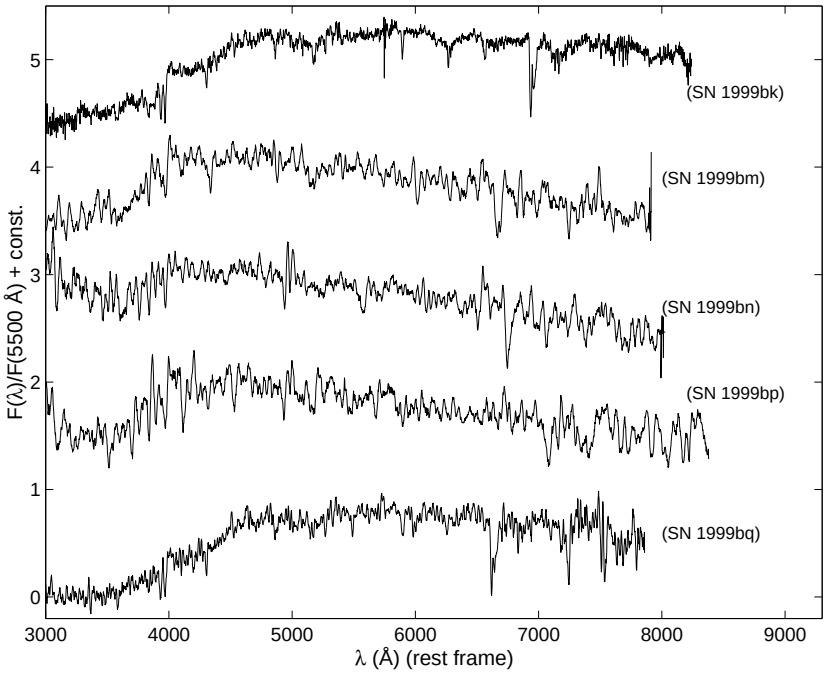

Figure 4.10: Reference spectra of the host galaxies corresponding to the indicated SNe.

SNe Ia, including peculiar objects, were used as templates. These spectra are listed in Table 2 of **Paper II** and correspond to SN 1981B, SN 1986G, SN 1989B, SN 1990N, SN 1991T, SN1991bg, SN 1992A and SN 1994D (see references in **Paper II**). The spectra of SN 1999aa, SN 1999ac, SN 1999aw, SN 1999be, and SN 1999bp from the Spring '99 sample were also used. The spectra used as templates for a given fit were those with epochs within 2 to 5 days from the epoch of the spectrum to be subtracted. At early epochs, given the rapid spectral evolution, the limit of 2 days was used. Beyond 20 days after maximum light, the evolution is slower, allowing to use templates with greater epoch differences. Typically, between 5 and 15 template spectra were used. The fit of the amount of host-galaxy contamination was performed for each template by minimizing the following χ^2 through a Levenberg-Marquardt method:

$$\chi^2(a,b) = \sum_{i=1}^{N} \sigma_i^{-2} \left\{ S_i^T(\lambda_R) - a \left[S_i^O(\lambda_R) - b S_i^G(\lambda_R) \right] \right\}, \qquad (4.1)$$

where, in each wavelength bin $i = 1, \ldots, N$, S_i^T is the template SN flux, S_i^O is the observed flux, S_i^G is the host galaxy flux from the reference spectrum, and σ_i is the uncertainty in the observed flux. The three spectra are first put in the rest frame ($\lambda_R = \lambda_{Obs}/(1+z)$). The parameters a and b were fitted for each template spectrum used. The scaling factor a was taken as a nuisance parameter of the fit. The values of b found for the different template spectra were combined through a weighed average in which values deviating by more than 3σ were rejected. The use of the average $\langle b \rangle$ was preferred to taking the value corresponding to the template that yielded the lowest reduced χ^2 ($\chi^2_\nu \equiv \chi^2/(N-2)$), since it produced more robust results and estimates of the uncertainty in b. The final value obtained for $\langle b \rangle$ was used to subtract the host-galaxy flux and compute the percentage of contamination on the photometric passbands. These contamination levels are given in Table 3 of **Paper I**, and their uncertainties, related to the uncertainty in $\langle b \rangle$, were generally within 1/10th of the level of contamination. The subtraction method was tested on a series of simulated cases and the contamination levels found proved to be accurate within $\sim$5%. Figure 4.11 shows an example of such a test, where a SN spectrum is artificially added a fraction of galaxy flux and the subtraction is compared with the original spectrum.

The final spectra from the Spring '99 campaign are shown in Figures 4.12 through 4.25, sorted by epoch. An additional Figure 4.26 presents the cases of spectra with very low SN signal or large uncorrected contamination from the host galaxy. The graphs show the combination of "blue" and "red" spectra, when two instrumental settings were used. The spectra with high noise levels were smoothed for clarity of the plots. The remarkable coverage of SN Ia spectra from 15 days before maximum to nearly 60 days after maximum can be noticed from those figures. The two brightest SNe, SN 1999aa and SN 1999ac, present 15 high-quality combined spectra each, covering the mentioned epoch range.

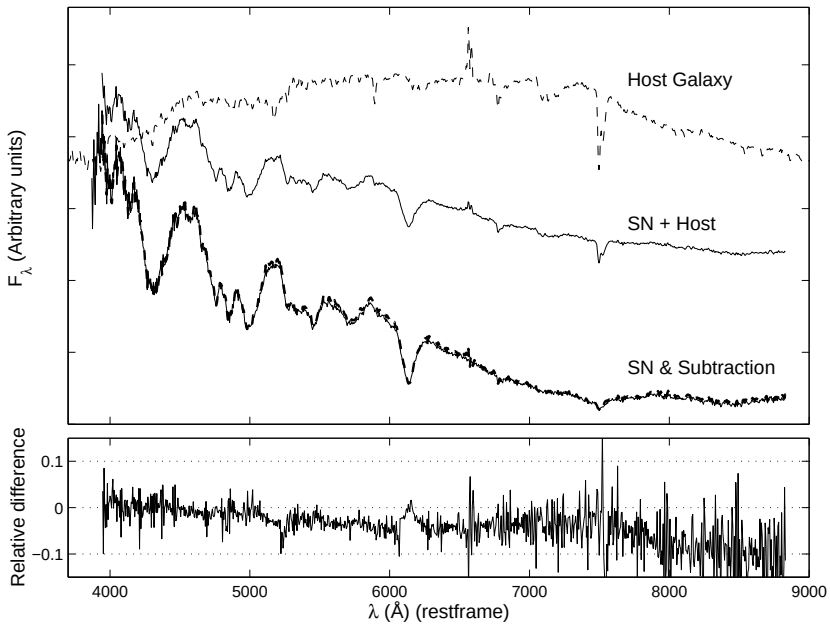

Figure 4.11: An example of a test for host-galaxy subtraction. *Upper panel*: The spectrum on top (dashed line) corresponds to NGC 2595, the host galaxy of `SN 1999aa`. In the middle, a spectrum of `SN 1999aa` at day +5 with its host-galaxy spectrum added (using a scale for the galaxy $b = 1$). The result of the subtraction (dashed line) and the original SN spectrum (solid line) are shown in the bottom of this panel. The fit yielded a value of $b = 0.98 \pm 0.05$. *Lower panel*: The relative residuals of the subtraction with respect to the original SN spectrum, computed as (Subtraction − SN)/SN.

Some peculiarities in the spectra of these SNe make them very interesting and motivated the work presented in **Paper III** and **Paper H**. Other SNe with detected peculiarities are `SN 1999aw` (see [75]) and `SN 1999bp`; eight combined spectra of each of these SNe were obtained. Six spectra of the peculiar `SN 1999by` are shown in the figures. Over 50 additional spectra correspond to the remaining 14 SNe Ia that were followed in the campaign. Every spectrum includes estimates of the statistical and systematic uncertainties, which allows quantitative analyses like those presented in **Paper II** and Section 5.2. Some of these results are also given in **Paper E**.

4.2 High-Redshift Supernova Spectroscopy with the VLT

A Longer Redshift Lever-Arm

As seen in Chapter 3, the current measurements of high-redshift SNe Ia in the approximate range $0.3 < z < 0.9$ exclude the cosmological models with $\Omega_\Lambda = 0$ at a confidence level >99%. However, the result of the fit is degenerate to a linear combination of Ω_M and Ω_Λ (see **Paper A**and Section 3.3). It is only when SN Ia results are combined with at least one measurement of Ω_M or $\Omega_M + \Omega_\Lambda$ from the fluctuations in the cosmic microwave background [6, 73], the properties of massive galaxy clusters [3, 11], or the large-scale structure of galaxies [27, 79] that the cosmological parameters can be disentangled leading to the current picture of a flat Universe dominated by dark energy. However, if the range of redshifts where SNe Ia are measured is increased, especially at $z > 1$, the results from SNe Ia alone can be sufficient to break the degeneracy between Ω_M and Ω_Λ (see [20]).

In order to pursue this aim, in the past few years, the SCP dedicated great effort to discover and follow up a number of SNe Ia at very high redshifts (up to $z \sim 1.2$). Such an attempt poses a challenge for the current observational capabilities. In addition to the increased difficulties of obtaining precise measurements of such distant SNe, the study of possible systematic uncertainties is more intricate.

A total of 8 supernova searches, divided in 4 observing campaigns, were carried out during the Springs of 2000, 2001 and 2002, and the Fall of 2002 (see **Paper G**). The searches were done by repeated imaging of selected fields (with some overlap among the fields of different searches), using 4-meter and 8-meter class telescopes (CTIO 4m, CFHT and Subaru). The imaging was done in the R and I passbands, which approximately cover the rest-frame BV bands at $z \sim 0.5$, and the rest-frame UB bands at $z \sim 1$. In general, the interval between observations ranged between 3 and 4 weeks. The Spring 2002 search at the CFHT was done in a "rolling" mode, in which images were taken once every few days during a two week period and the whole process was repeated

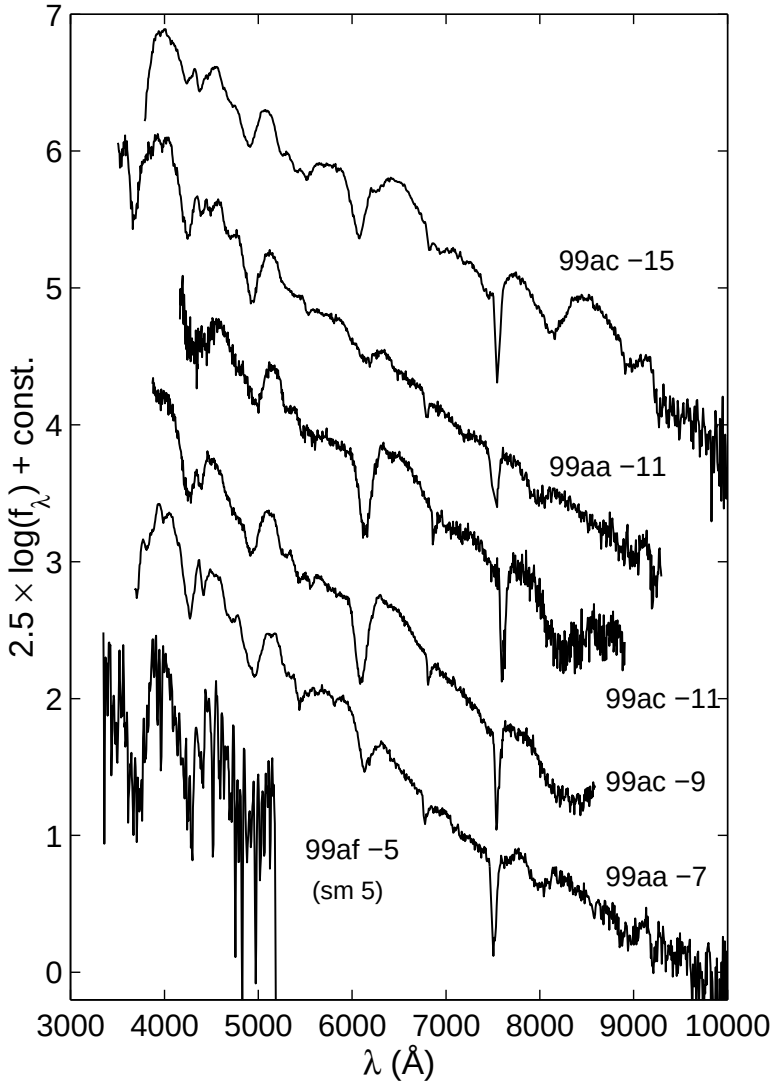

Figure 4.12: Follow-up spectra of the Spring '99 SNe Ia. Series 1: epochs −15 to −5 d. Spectra which have been smoothed are indicated with "(sm x)", where x is the size in pixels of the smoothing box.

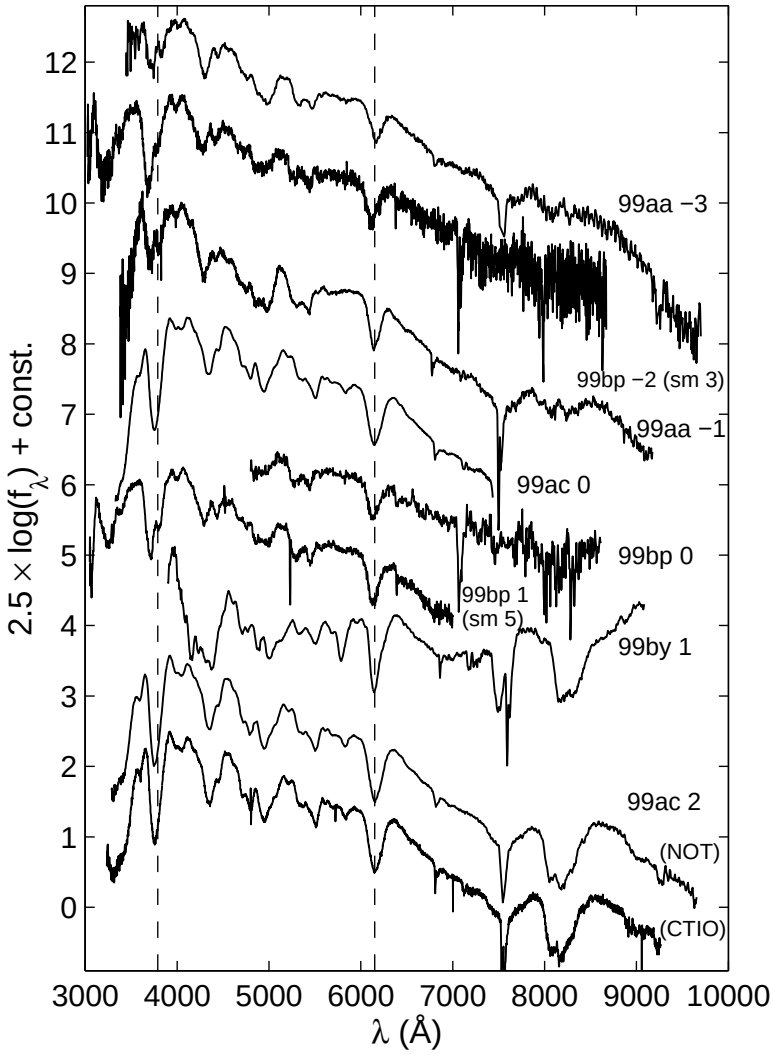

Figure 4.13: Follow-up spectra of the Spring '99 SNe Ia. Series 2: epochs −3 to 2 d. The vertical dashed lines mark the positions of $\lambda = 3790$Å and $\lambda = 6150$ Å. Spectra which have been smoothed are indicated with "(sm x)", where x is the size in pixels of the smoothing box.

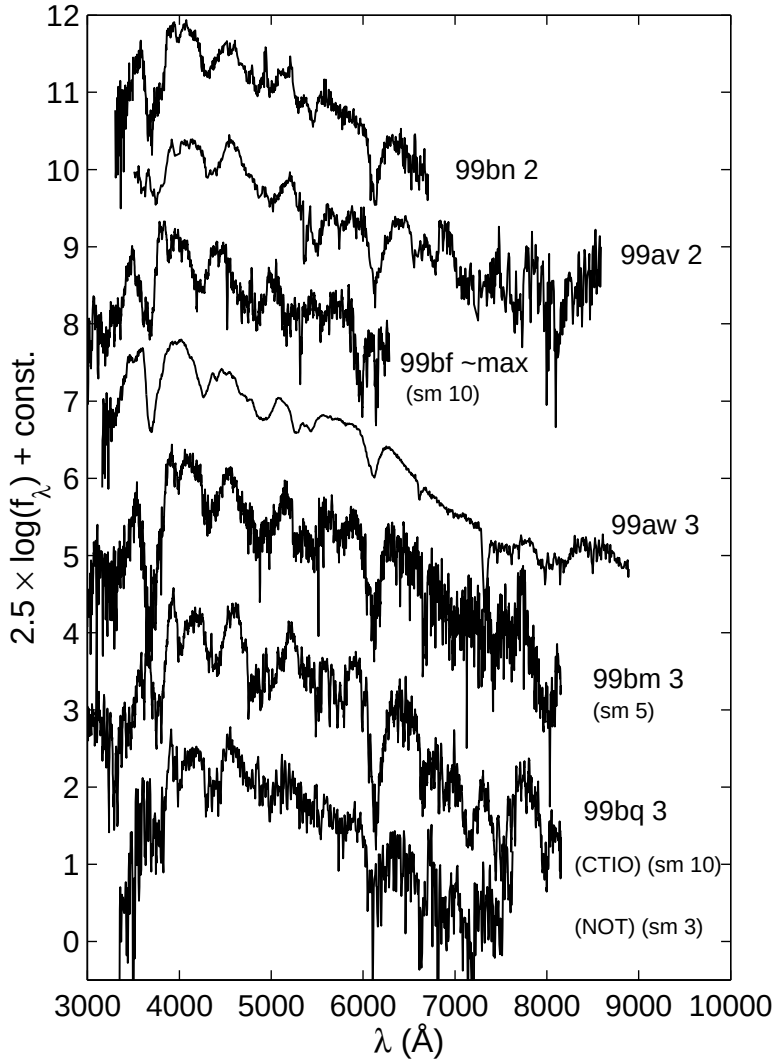

Figure 4.14: Follow-up spectra of the Spring '99 SNe Ia. Series 3: epochs 2 to 3 d. Spectra which have been smoothed are indicated with "(sm x)", where x is the size in pixels of the smoothing box.

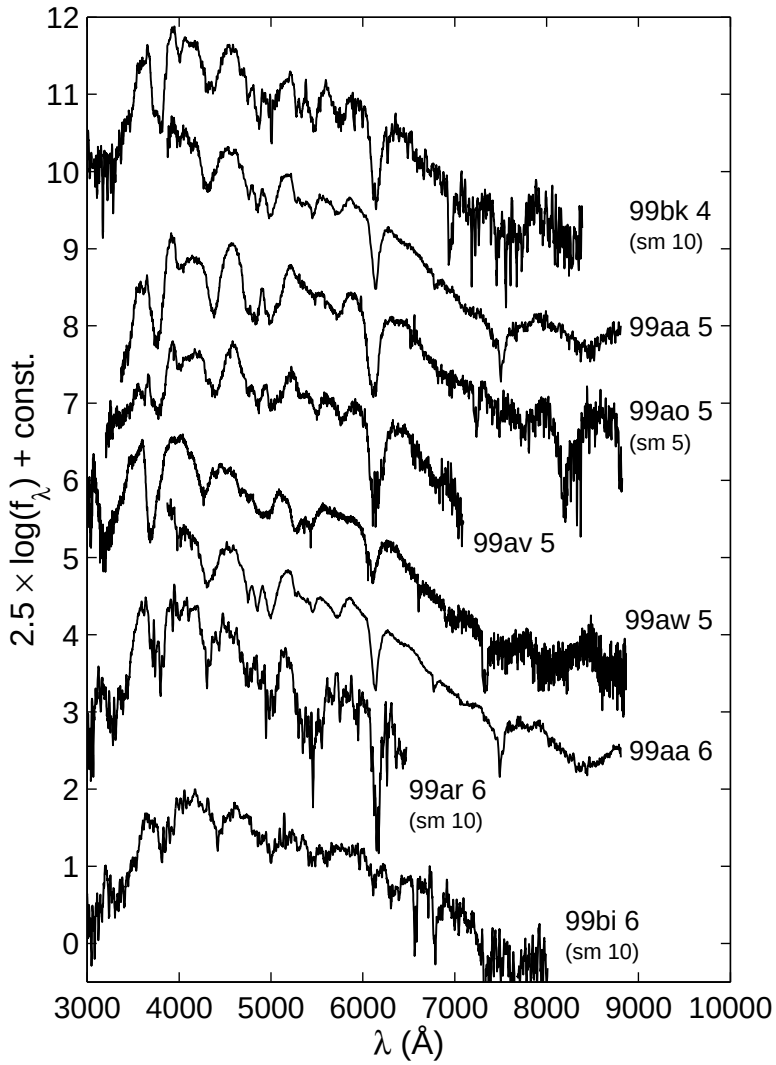

Figure 4.15: Follow-up spectra of the Spring '99 SNe Ia. Series 4: epochs 4 to 6 d. Spectra which have been smoothed are indicated with "(sm x)", where x is the size in pixels of the smoothing box.

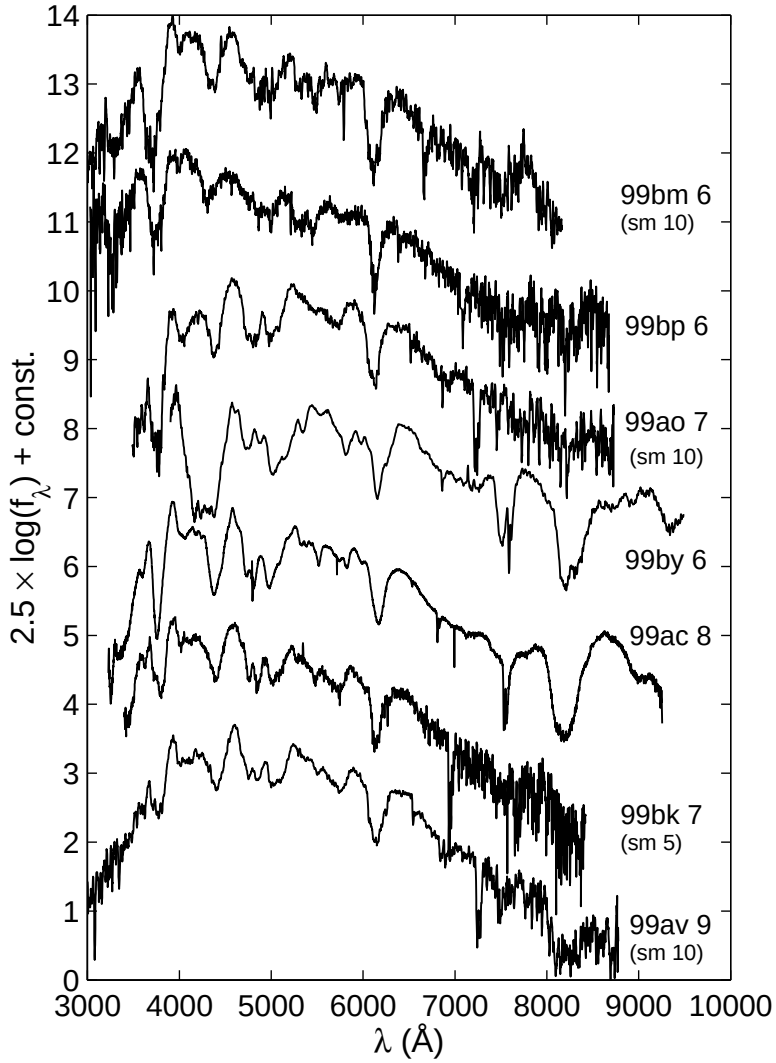

Figure 4.16: Follow-up spectra of the Spring '99 SNe Ia. Series 5: epochs 6 to 9 d. Spectra which have been smoothed are indicated with "(sm x)", where x is the size in pixels of the smoothing box.

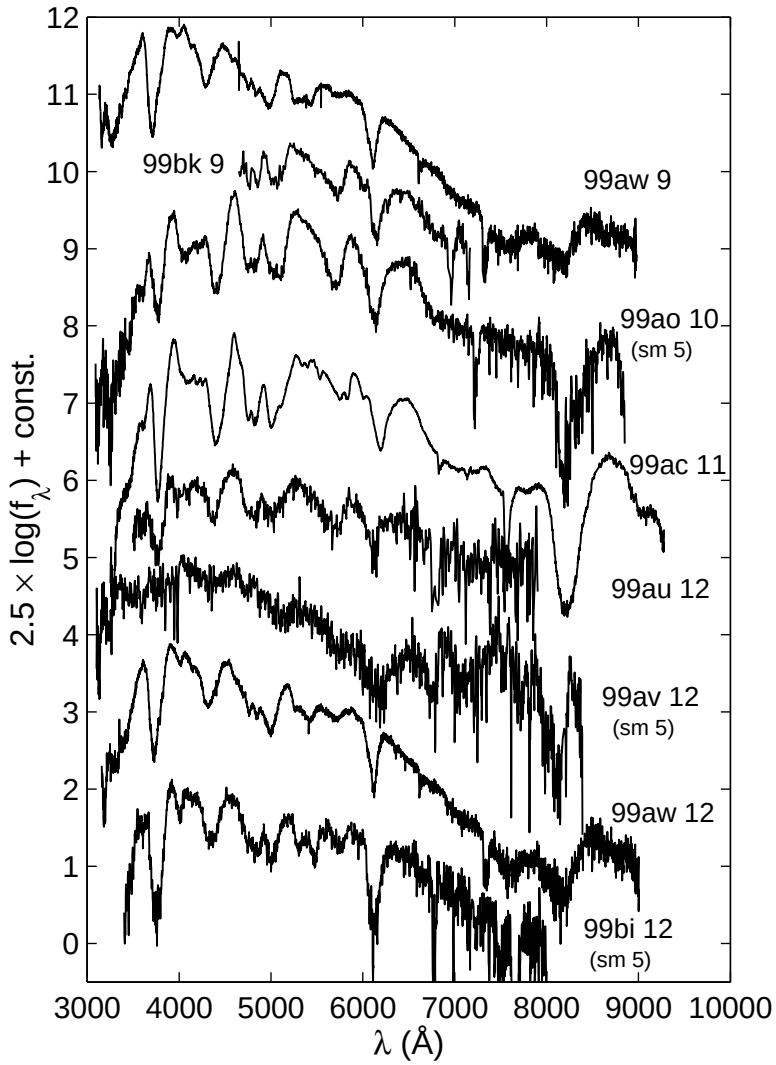

Figure 4.17: Follow-up spectra of the Spring '99 SNe Ia. Series 6: epochs 9 to 12 d. Spectra which have been smoothed are indicated with "(sm x)", where x is the size in pixels of the smoothing box.

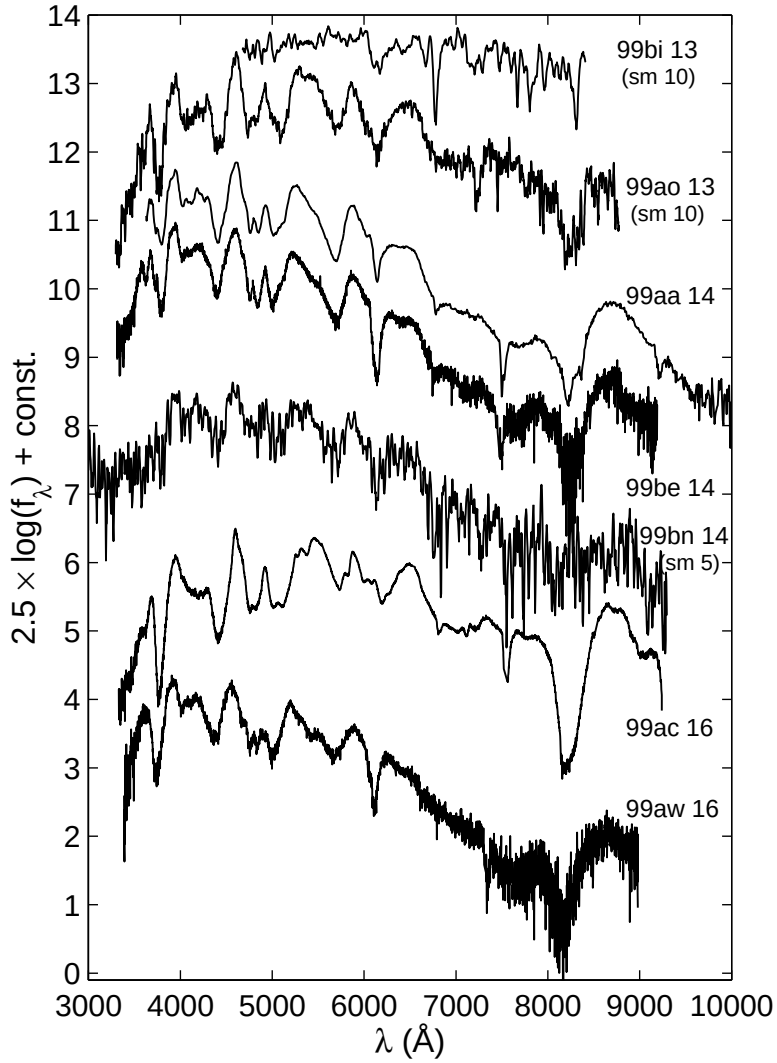

Figure 4.18: Follow-up spectra of the Spring '99 SNe Ia. Series 7: epochs 13 to 16 d. Spectra which have been smoothed are indicated with "(sm x)", where x is the size in pixels of the smoothing box.

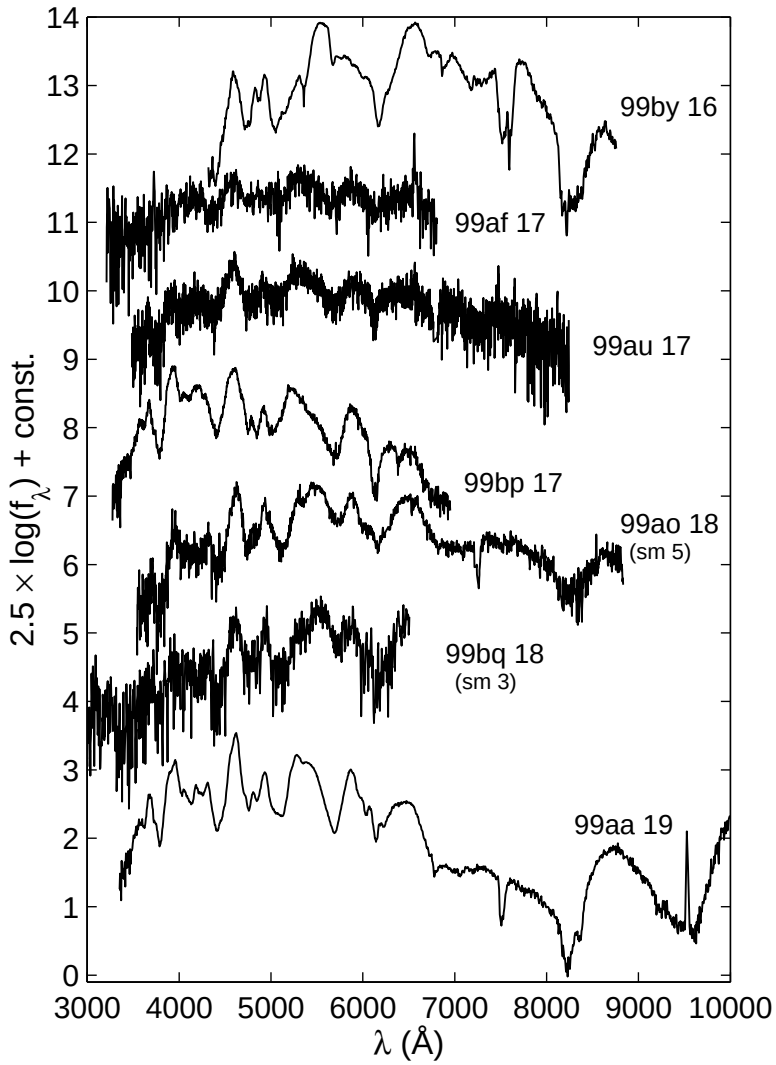

Figure 4.19: Follow-up spectra of the Spring '99 SNe Ia. Series 8: epochs 16 to 19 d. Spectra which have been smoothed are indicated with "(sm x)", where x is the size in pixels of the smoothing box.

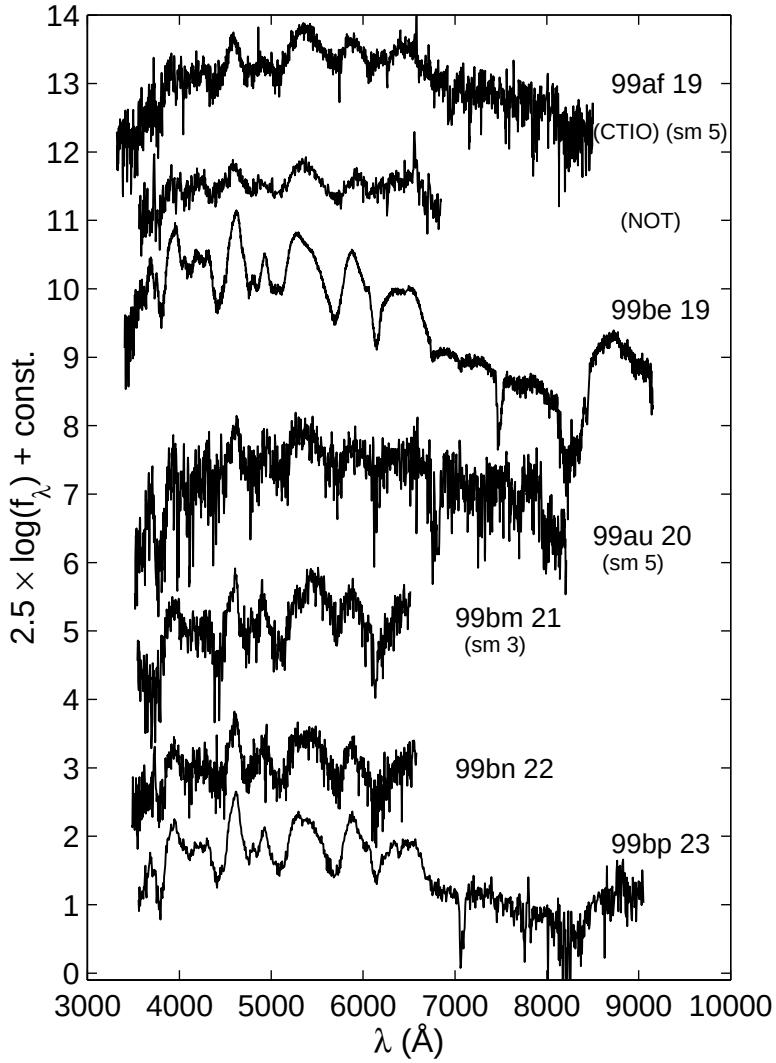

Figure 4.20: Follow-up spectra of the Spring '99 SNe Ia. Series 9: epochs 19 to 23 d. Spectra which have been smoothed are indicated with "(sm x)", where x is the size in pixels of the smoothing box.

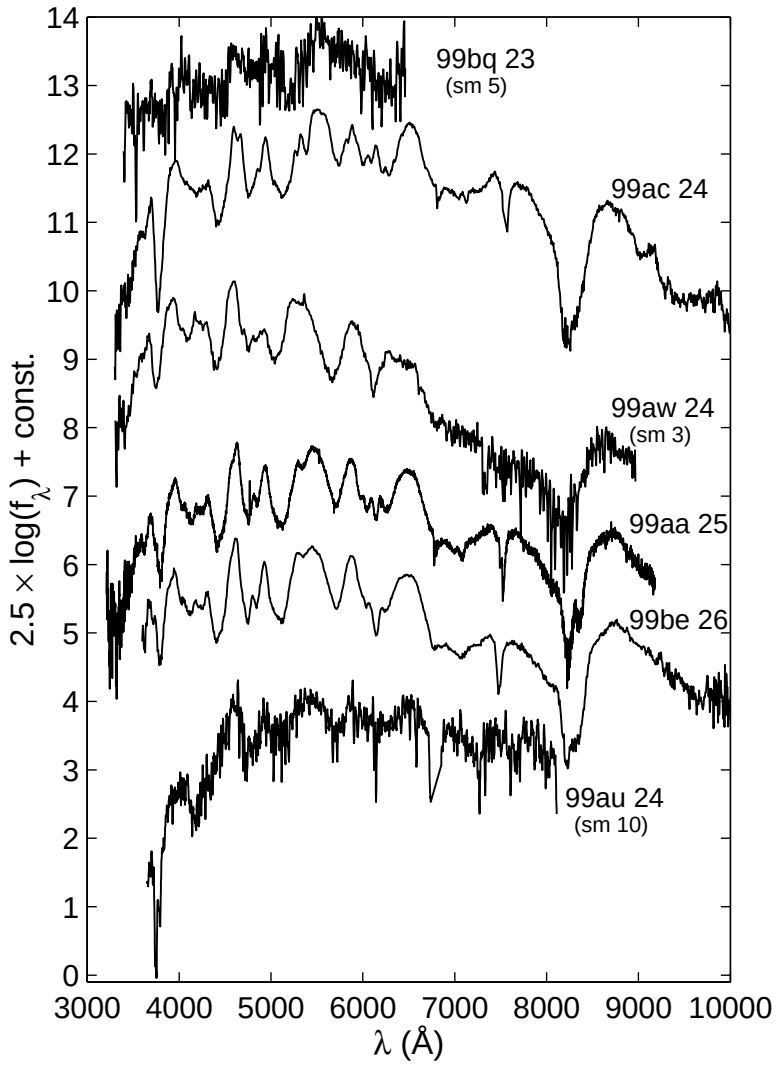

Figure 4.21: Follow-up spectra of the Spring '99 SNe Ia. Series 10: epochs 23 to 26 d. Spectra which have been smoothed are indicated with "(sm x)", where x is the size in pixels of the smoothing box.

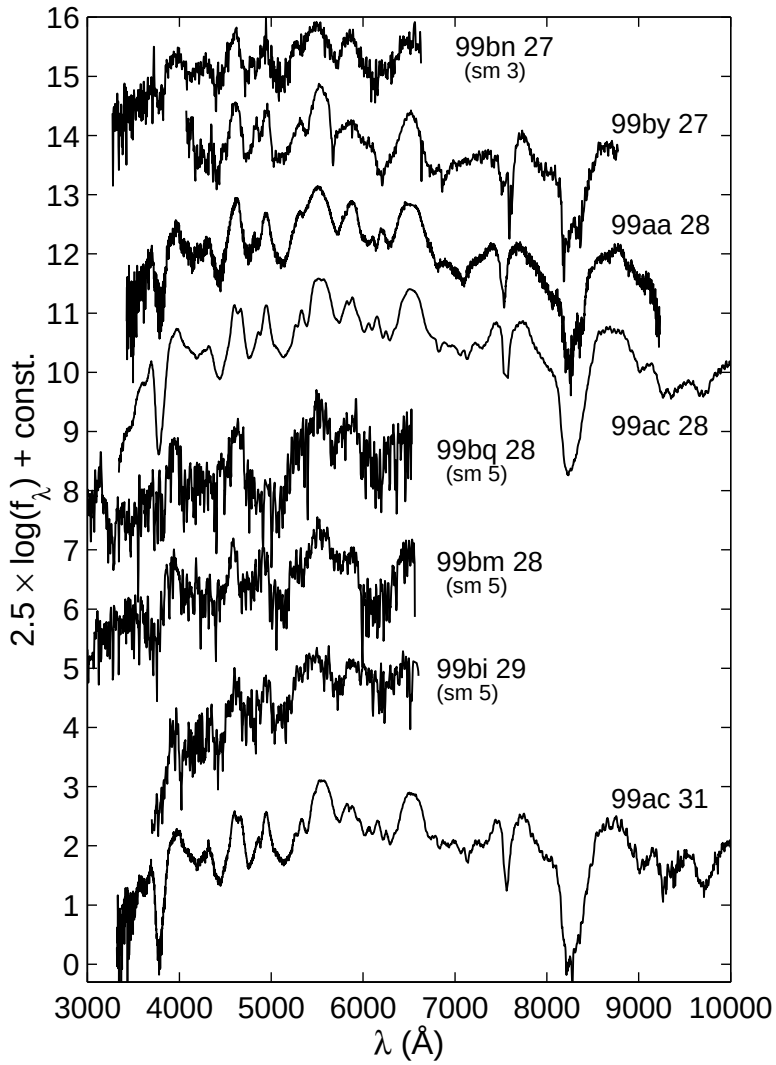

Figure 4.22: Follow-up spectra of the Spring '99 SNe Ia. Series 11: epochs 27 to 31 d. Spectra which have been smoothed are indicated with "(sm x)", where x is the size in pixels of the smoothing box.

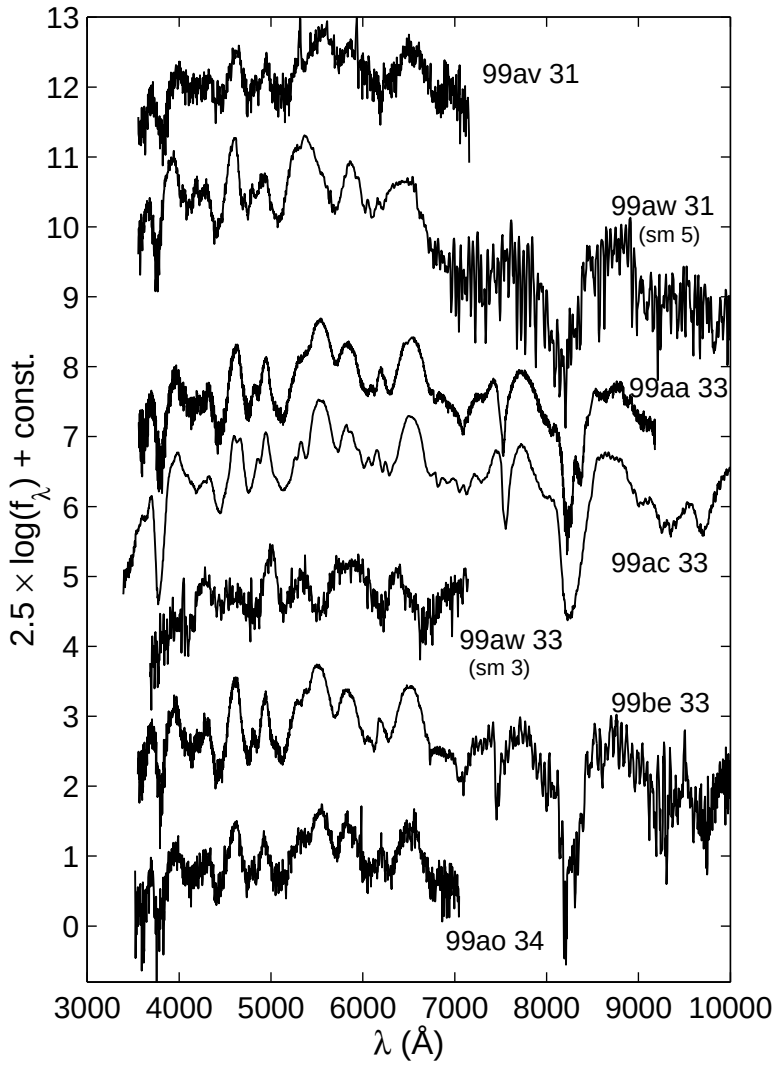

Figure 4.23: Follow-up spectra of the Spring '99 SNe Ia. Series 12: epochs 31 to 34 d. Spectra which have been smoothed are indicated with "(sm x)", where x is the size in pixels of the smoothing box.

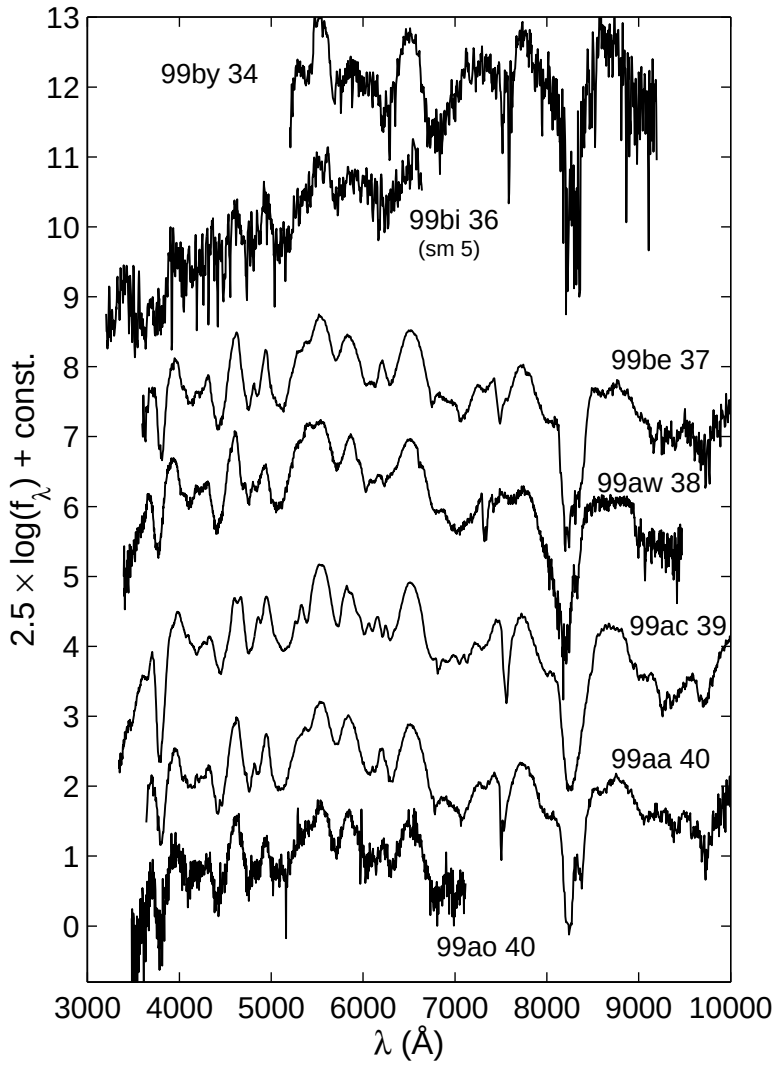

Figure 4.24: Follow-up spectra of the Spring '99 SNe Ia. Series 13: epochs 34 to 40 d. Spectra which have been smoothed are indicated with "(sm x)", where x is the size in pixels of the smoothing box.

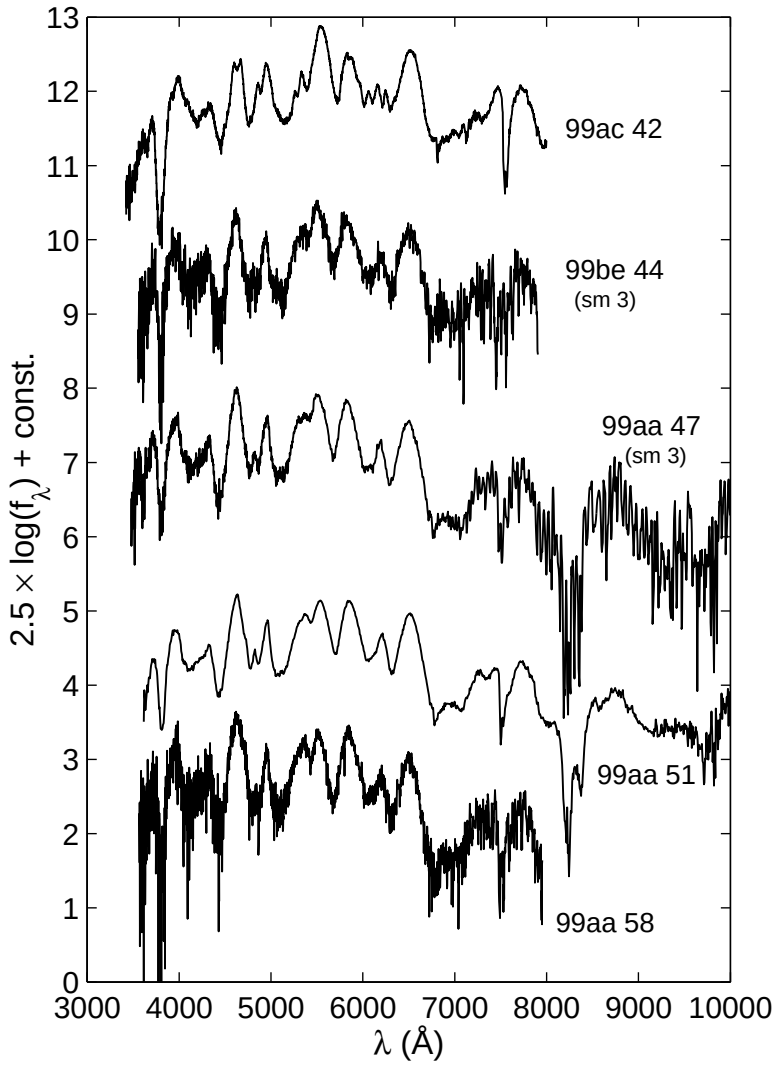

Figure 4.25: Follow-up spectra of the Spring '99 SNe Ia. Series 14: epochs 42 to 58 d. Spectra which have been smoothed are indicated with "(sm x)", where x is the size in pixels of the smoothing box.

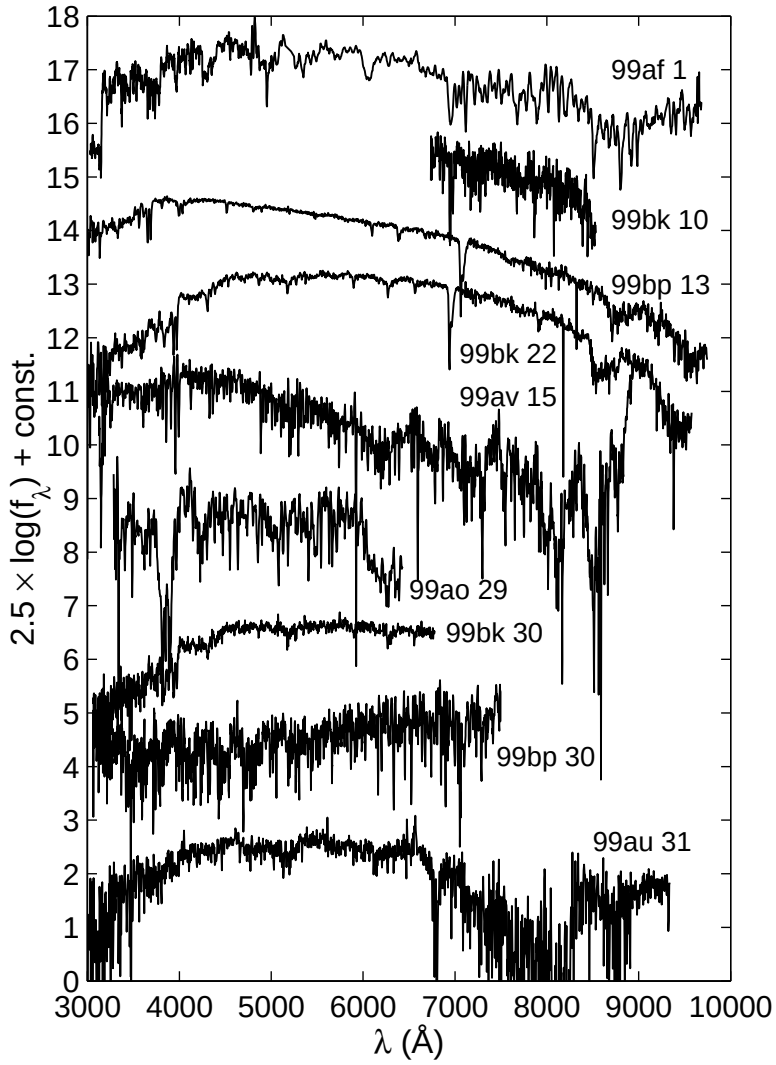

Figure 4.26: Follow-up spectra of the Spring '99 campaign showing too low SN signal and uncorrected host-galaxy contamination.

over three months. This type of search assures the photometric follow-up of the candidates without the need to schedule further observations after confirmation.

The images from the search campaigns were processed in the usual manner in order to find objects that had brightened [58, 59, 57]. These SN candidates were assigned a level of priority according to the amount of brightening, the apparent location on the possible host galaxy, and the apparent magnitude, to optimize the discovery of SNe Ia in the desired redshift range. The candidates were distributed to be confirmed by spectroscopic observations done at 8-meter class telescopes from Keck, Paranal, Gemini and Subaru observatories. The distribution took into account the priority assigned to each candidate, the capability of the instruments and the weather conditions at each observing site. The confirmation spectra were also used to obtain a precise value of the redshift of the SNe. The position of narrow galaxy features, when detected, yielded values of z with a precision of 0.001. In other cases, the shape of the broad SN features was compared with template spectra, and the redshift was obtained with a precision of 0.01.

Since the main purpose of these observations was to obtain a secure classification and a precise redshift for the candidates, the quality of the spectra was usually limited (with signal-to-noise ratios between <1 and ~ 10 per wavelength bin). Only a few of the brightest SNe were targeted more than once. However, the set of SN Ia spectra finally obtained is of remarkable value and justifies its detailed analysis. An important part of the work for this thesis involved the observation, data reduction and analysis of the confirmation spectra obtained for these campaigns at the ESO *Very Large Telescope* (VLT). The description below focuses on the way these spectra were obtained and processed previous to their analysis, which is presented in Chapter 5.

Spectroscopic Observations

A total of 40 candidates from the search campaigns mentioned above were screened with spectroscopic observations done at the ESO VLT. As a result of these observations, 14 candidates were securely classified as SN Ia with redshifts between 0.212 and 1.181. Other 6 candidates were classified as possible SN Ia with redshifts between 0.44 and 1.086 (see IAU circulars, 7763, 7764, 7971, 7977, 7993, 8119, 8120, 8121).

The spectra from the VLT were obtained using the FORS1 and FORS2 instruments in long-slit spectroscopic mode. Before the Spring of 2002, only FORS1 was used. Its CCD presented lower sensitivity at red wavelengths, when compared with detectors available at other observatories involved in the campaign. Therefore, the VLT was generally assigned the observation of the brightest candidates, which were expected to be at lower redshifts, and did not need coverage on the red end of the spectrum in order to obtain a reliable classification. The availability of a mosaic of red-optimized CCDs at FORS2 in the Spring of 2002 made it possible to also use the VLT facilities to confirm also the

faintest candidates discovered.

Three grisms (300V, 300I and 600z) and two slit widths (0.7" and 1.0") were used in the observations. The grisms were chosen according to the expected redshift of each candidate, given the discovery magnitudes. During the Spring 2000 and 2001 campaigns, only grism 300V was used. The slit width was varied according to the seeing. The observing conditions at Paranal are generally very good, with seeing seldom above 1". The grisms were used together with order-blocking filters: grism 300V with filter GC435, and grisms 300I and 600z with filter OG590. The total exposure times varied between 10 minutes and 4 hours, depending on the brightness of the candidates. The observations of each candidate were usually divided in three or more exposures with small offsets along the slit. This facilitated the subtraction of the background and the rejection of cosmic rays. In cases when the data were reduced while the observations were being done (this was possible when observing in *visitor mode*), the total exposure lengths were reviewed according to the results of the first spectra obtained. When the data collected was considered sufficient to allow the classification of the candidate, all further exposures planned were aborted. In cases when a faint candidate was of special interest for the project (e.g., a probable SN Ia at very high redshift), the decision of extending the observations was taken.

Because of the faintness of the candidates, the slit was aligned through a bright reference star in order to assure a correct acquisition. The availability of suitable finding charts for all candidates was essential at this stage. Figure 4.27 shows an example of a finding chart, corresponding to a SN Ia discovered at $z = 0.510$; The very faint SN is marked in the center, as well as some reference stars. In one occasion, two candidates found near to each other were placed in the slit simultaneously to save observing time. The prescription of placing the slit at parallactic angle was therefore not followed. As a consequence, the spectra are subject to wavelength-dependent light loss due to DAR. However, the observations were usually done near culmination, and therefore, with low airmasses, which reduced the effect of DAR.

Spectra Reduction

The reduction of the data was done with the use of standard `IRAF` routines. A quick reduction was done as soon as the spectra were obtained, in order to plan the following observations. A *pipeline* procedure, including bias subtraction, flat-field correction, and wavelength calibration, was developed to speed the process. The spectra were afterward background-subtracted, extracted and calibrated in flux. When observing in *visitor mode*, the reduction of a spectrum was usually done while the next spectrum was being exposed. Due to the hastiness of the process, in some cases, the suitable calibration images were not available for this first reduction. In those cases, calibration images from other nights were used. The stability of the FORS1 and FORS2 instruments allowed acceptable results for the purposes of classification and redshift determination.

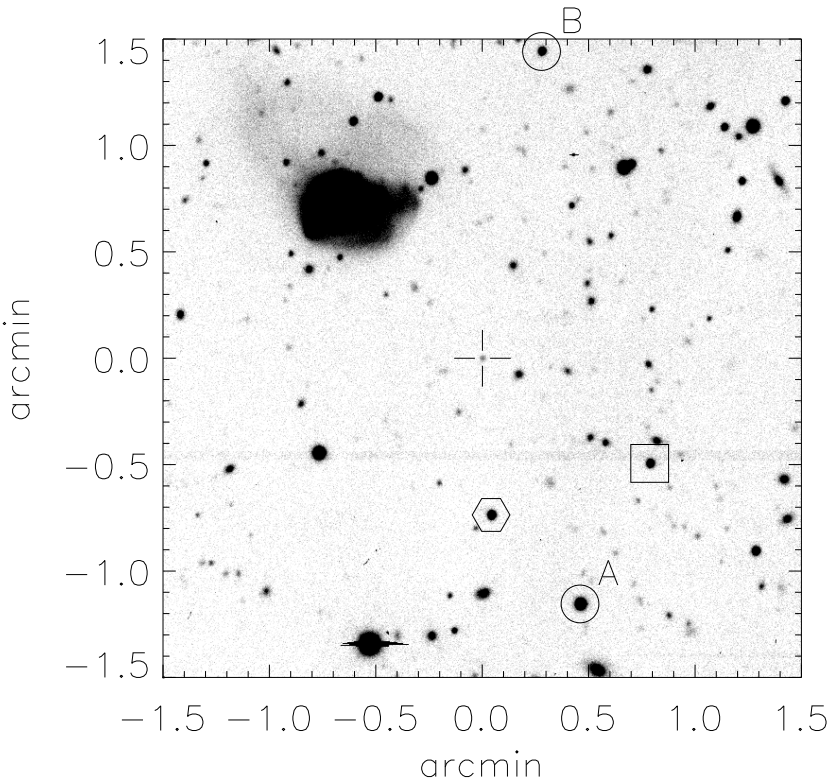

Figure 4.27: Finding chart for `SN 2002gl` at $z = 0.510$. The faint SN is marked with a cross. Several bright objects are marked for reference. The offsets to those objects were used to locate the slit on the SN.

Some of the spectra obtained during these campaigns showed enough quality to merit further analysis. This motivated a second, more thorough reduction, done with greater care in background subtraction, cosmic ray rejection, and uncertainty estimation.

For observations done with grism 300V, the second reduction did not differ in methodology from the first one. The background signal was accurately removed by fitting a smooth function along the spatial direction. This was possible because of the modest effect of fringing and the sparseness of sky lines. The combination of individual spectra and the use of a variance-weighed extraction procedure allowed a suitable rejection of cosmic rays.

In the case of spectra obtained with grisms 300I and 600z, the effect of fringing and sky lines was more significant. The faintness of the SNe with respect to the sky background required a careful treatment of the data in order to reduce the systematic effect of subtraction residuals. A non-standard subtraction of the background was done, following the lines of the usual procedure for near-infrared data reduction. First, a *fringe frame* is created by averaging the spectra obtained using the same instrumental settings (grism and slit width). In the averaging process, the spectra are scaled by the median and the objects are rejected. The rejection of the objects is possible due to the use of offsets between exposures. In the present case, the stability of FORS1 and FORS2 allowed the use of spectra from different nights to build some of the fringe frames. For each exposure of a given object, the fringe frame is scaled by the median and subtracted. The fringe-corrected spectra of each object are finally combined. Since the cosmic-ray rejection algorithm used is based on the signal level, a suitable rejection is accomplished after adding back an average background spectrum to the spectra. This background spectrum is built by averaging the non-subtracted spectrum along the spatial direction. After combination, the background spectrum is removed.

The resulting two-dimensional background-subtracted spectrum is therefore free of fringing and cosmic rays. In summary, this procedure uses the information of the background from other spectra to produce a very clean subtraction of the fringing pattern and sky lines, at the expense of obtaining a slightly lower signal-to-noise ratio, when compared with the standard background subtraction technique. Figure 4.28 shows a comparison of the results from the two techniques.

The two-dimensional spectra obtained in this way were used to extract the signal of the object inside an aperture along the dispersion axis. The extracted one-dimensional spectra were then calibrated in flux with the use of suitable standard star observations.

Beyond Classification

The additional effort of redoing the spectra reduction had the aim of using those spectra for further quantitative analysis. **Paper IV** presents the analysis

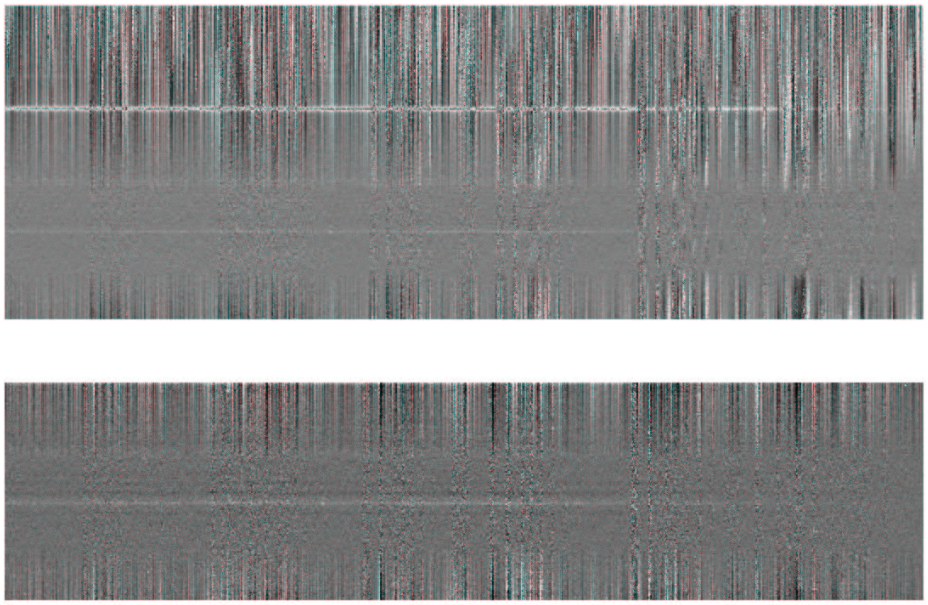

Figure 4.28: A comparison of the two background subtraction techniques applied to the spectrum of `SN 2002ks` at $z = 1.181$ (**Paper G**). The spectrum was taken with FORS2 and grism 300I, on a 3600 s exposure. *Upper panel*: The classical technique fails to accurately remove the fringing pattern. The residuals are noticeable on the red part od the spectrum (to the right of the image). The SN is the fainter trace on the bottom of the image. The trace above it corresponds to the offset star. *Lower panel*: The non-standard technique produces a better subtraction, at the expense of signal-to-noise ratio.

of a subset of 14 spectra corresponding to 12 of the SNe Ia spectroscopically confirmed at the VLT. Figure 4.29 shows the distribution of redshift and epoch (in days from maximum light) of those spectra. More details about the analysis are given in Section 5.3. A final stage in the preparation of the spectra was the subtraction of the contribution from the host galaxy flux.

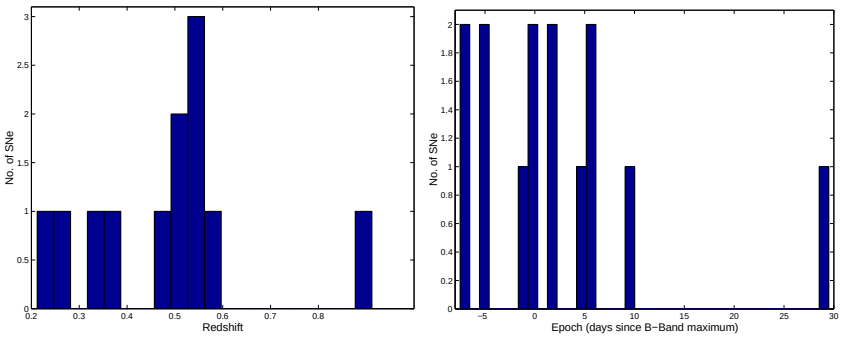

Figure 4.29: *Left-hand panel*: Redshift distribution of the 12 high-z SNe Ia observed at the VLT. *Right-hand panel*: Epoch distribution of the 14 spectra corresponding to those SNe Ia.

In general, the SNe observed in these campaigns could not be resolved from their host galaxies. Therefore, the extracted spectra showed some amount of host-galaxy flux. This contribution did not affect the classification of the SNe discovered. Furthermore, the presence of galaxy features was useful to obtain a precise value of the redshift. However, the use of the spectra for a quantitative analysis of the spectral properties of SNe Ia at high redshifts required the subtraction of the host-galaxy contribution from the observed flux. The method used for this purpose is similar to the one applied to the Spring '99 spectra. An important difference is that the *reference* spectrum of the particular host galaxy was generally not available. Instead, template galaxy spectra were used, with the additional uncertainty of the type of galaxy spectrum to subtract. The fitting procedure therefore tried a grid of galaxy spectra of different types, along with a grid of template SN spectra. In addition, the uncertainties in the dating of the spectra were larger than in the Spring '99 sample. Thus, a wider range of dates was used in the selection of the SN templates. From all the combinations of SN and galaxy templates tried, the one yielding the lowest χ^2 was used to perform the subtraction. The results of these subtractions are given in Table 1 of **Paper IV**. The table lists the percentage of galaxy flux integrated over the whole wavelength range. The method was tested on simulations that reproduced the quality and contamination levels of the data, and proved to be accurate within 10% of contamination. The final subtracted SN spectra are shown in Figures 1 to 3 of **Paper IV**.

Chapter 5

Analysis of Type Ia Supernova Spectra

5.1 Spectra: The Hidden Face of Supernovae

As was described in Chapter 3, it is the spectra that allow to distinguish among the different SN types. Such distinction is required in cosmology measurements to avoid contamination from misclassified non-type Ia SNe. Detailed spectral studies of well observed SNe Ia as they evolve in time are necessary to improve the classification system, and to detect possible peculiarities. This is of special importance when classifying SNe at high-redshift, usually with data of lower quality and covering a limited wavelength range due to redshift. High-quality spectral time series covering all possible pass-bands are also required for obtaining accurate K-corrections, as seen in Section 3.3.

Moreover, spectra provide detailed information about the physical processes that take place in the expansion of the SN ejecta. With the help of computer models, the composition, excitation temperatures and kinematics of the ejecta can be assessed. These studies also provide hints about the explosion mechanisms. The large broadening of spectral lines (corresponding to expansion velocities of $\sim$10000 km/s or higher) and the rapid changes observed in SN Ia spectra, especially at early times, suggests a very violent process involving a large amount of material from the progenitor system. As the ejecta expands and cools, the observations probe deeper regions. These translates into changes of the observed profile and strength of spectral lines and an overall change of the continuum shape. Figure 5.1 is an illustration of the spectrum formation process at different times. The photosphere recedes into the ejecta and the spectral features due to different ions evolve.

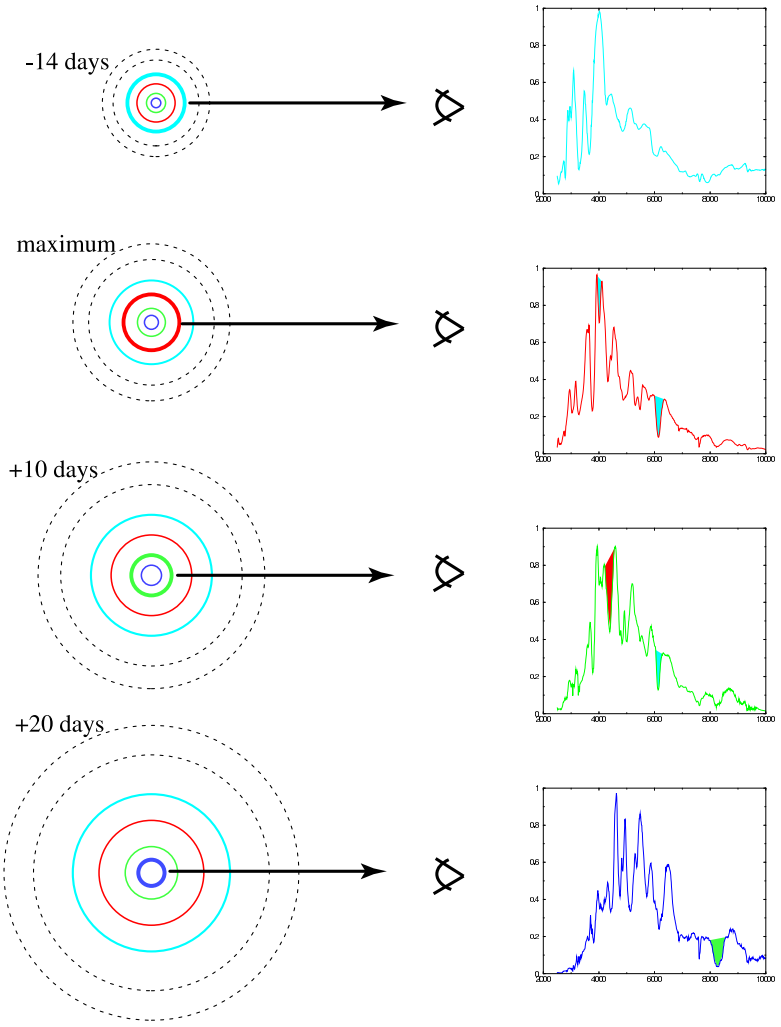

Figure 5.1: A schematic view of the SN spectrum formation process. As the ejecta expands and cools, the continuum and line properties change. The photosphere recedes in the ejecta and lines of different ions appear at different phases.

Models. The use of computer models that solve or simulate the radiation transport and kinematics in the ejecta has provided reliable identifications for most of the features observed. An example of such analysis is given in **Paper III** for the detailed study of SN 1999aa, observed during the SCP Spring 1999 Nearby Supernova Campaign (see Sec. 4.1). A similar analysis for SN 1999ac is presented in **Paper H**. The code used for these studies is called SYNOW [33]. The code does not solve the equations of radiative transport nor the rate equations. Instead, line scattering is taken into account to compute the transfer in the Sobolev approximation, given an input list of ions with certain optical depths and velocity ranges in the ejecta. The Sobolev approximation, i.e., that the physical conditions except for the velocity are constant in the region where the resonance absorption is produced, is a good approximation for SN ejecta. The expansion velocities are much greater than the thermal velocities, which assures that the photons are in resonance with a certain transition in a small region. Spherical symmetry, homologous expansion, and a sharp photosphere that emits a blackbody spectrum are also assumed. The results are not fits to the data but *comparisons* where the user "tunes" the parameters by trial and error. Figure 5.2 shows an example of a SYNOW model extracted from **Paper III**. SYNOW provides a fast method to identify spectral lines and the regions of the ejecta, in velocity space, where each ion is found. Due to the approximations involved, the exact line profiles are generally not reproduced, nor is the overall continuum shape. Furthermore, because line identifications are done with SYNOW through trial and error, further confirmation is required. For instance, multiple line matches for a given ion provides strong evidence for a reliable identification. Alternatively, the use of other, more sophisticated computer models can provide with a confirmation.

Spectral evolution. Before and around maximum light, the optical spectra of SNe Ia generally show a blue continuum with a superposition of broad P Cygni lines of neutral and singly ionized intermediate-mass elements (mainly O, Mg, Si, S and Ca), and a smaller contribution from iron-peak elements (Fe, Co). Three Si II lines are characteristic of SNe Ia: Si II $\lambda\lambda$4130, 5972, and 6355. The latter is very prominent, as well as the blend of Ca II H&K $\lambda\lambda$ 3934 and 3968.

About one week after maximum light, iron-peak element lines begin to dominate, although Si II λ6355 and Ca II H&K are still strong, and the feature due to the Ca II infrared triplet becomes stronger. Also, an absorption feature attributed to Na I begins to develop. The P Cygni profiles start to show increasing emission components. The SN gradually enters the nebular phase after one month from maximum light. The continuum keeps decreasing while emission lines (including some forbidden lines) dominate. The absorption components of Ca II H&K and the IR triplet remain visible several months after maximum light.

The prototypes of normal SNe Ia are SN 1972E, SN 1981B, SN 1989B, SN 1992A. Peculiar SNe Ia are identified spectroscopically through significant dif-

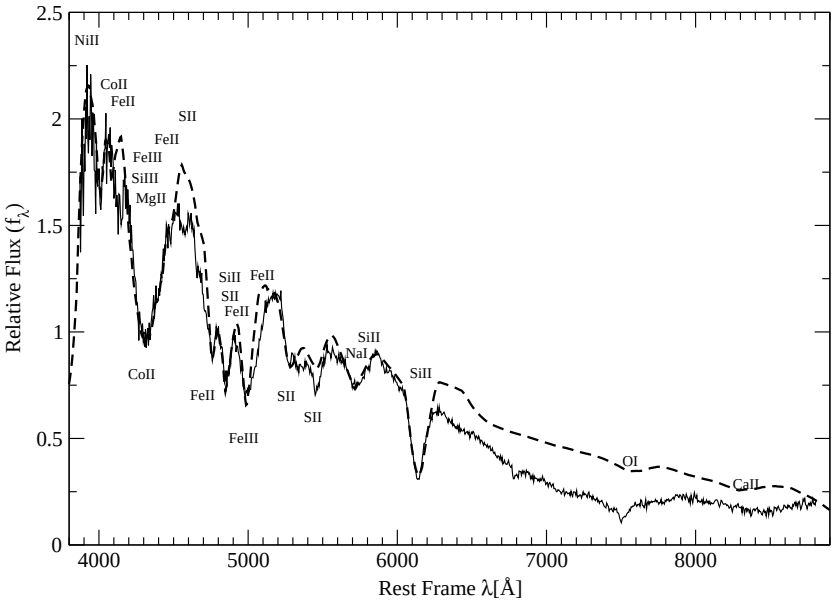

Figure 5.2: A `SYNOW` synthetic spectrum (*dashed line*) reproducing the main features of spectrum of `SN 1999aa` at +5 d (*solid line*). The main ions input in the code are shown. Note that the overall shape of the continuum cannot be reproduced with this relatively simple code.

ferences in the shape and strength of some features. Two main subtypes have been identified, according to two well-observed prototypes: SN 1991T and SN 1991bg (see Figure 3.2). Before maximum light, 1991T-like SNe show weak absorptions due to intermediate-mass elements, but strong Fe III lines. The differences become less evident after maximum light. SNe of this kind present slowly evolving lightcurves and are slightly more luminous than normal SNe Ia (by $\sim$0.3 mag). The group of 1991bg-like SNe, on the contrary, show very strong absorption features attributed to Ti II, which remain well after maximum light. These SNe are sub-luminous compared to normal SNe Ia (by $\sim$2 mag) and show rapidly declining lightcurves. Some other peculiar SNe have been discovered that do not correspond to any of these two cases (e.g., SN 2000cx [39] and SN 2002cx [38]).

Figure 5.3 shows the spectral sequence of the peculiar type Ia SN 1999aa. The data cover from very early stages to almost two months after maximum light. As described in **Paper III**, the slight peculiarities of this SN, mainly the weakness of Si II and Ca II lines, are evident in the pre-maximum spectra. After one week from maximum light, the spectra resemble more closely those of prototypical "normal" SNe Ia (or "Branch normal"). As discussed in the paper, SN 1999aa may show an intermediate case between 1991T-like and normal SNe Ia, suggesting a continuous change in the physical properties from normal to 1991T-like SNe (see also [40]). A good time coverage, starting well before maximum light, is therefore crucial to detect these peculiarities and to improve our knowledge on SNe.

Spectral Parameters

Several empirical parameters that can be measured on the spectra of SNe Ia have been introduced to help interpret the observations and to provide a connection to the models. These parameters are complementary to those related to lightcurve properties and may prove useful in the calibration of SNe Ia as distance indicators. The most commonly used spectral parameters have to do with measurements of Doppler shifts and intensities of certain lines. The measurements allow statistically robust comparisons among SNe and with predictions from models.

Velocities. The Doppler shift of the absorption minimum in the P Cygni profile of an unblended line provides a measure of the expansion velocity. In general, SN spectra present high expansion velocities ($\sim$10000 km/s), which produces line broadening and therefore, a large degree of line blending. The lines that can be considered to be fairly isolated are Si II λ6355, Ca II H&K, and S II λ5640. If the line is weak, the velocity measured in this manner corresponds to the photospheric velocity. At very early stages, the photosphere is located at large radii and the lines are formed close to it. Therefore, weaker lines like Si II λ6355 and S II λ5640 track the photospheric velocities in a very steep decline. After

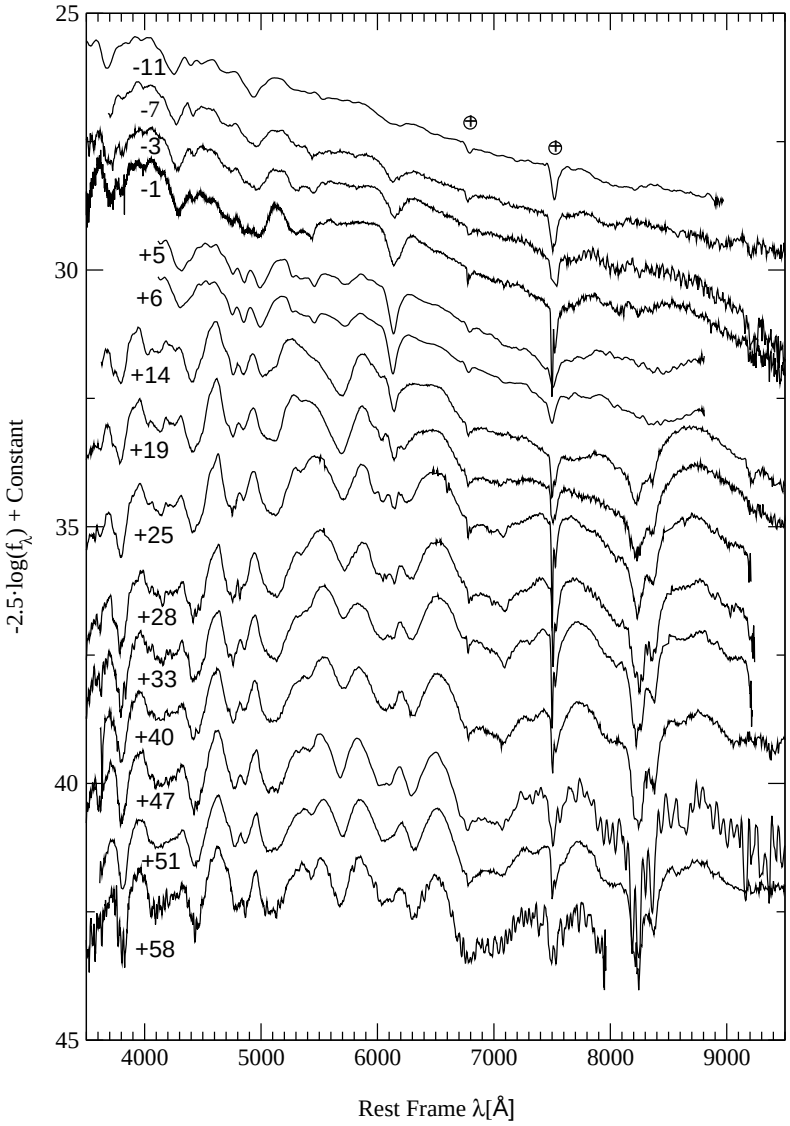

Figure 5.3: Spectral time series of SN 1999aa observed during the SCP Spring '99 campaign. The remarkable age coverage and quality of the spectra allowed to identify certain peculiarities for this SN, as described in **Paper III**.

maximum light, the photosphere recedes into denser regions and the weak-line approximation is not valid any more. While models indicate that the photospheric velocity continues decreasing at a rather constant rate, the velocities measured on spectral lines level out at higher values. Ca II H&K is a much stronger line for which the velocities are larger than the photospheric ones, even at very early stages (i.e., about 2 weeks before maximum light). Even if these velocities are not useful to determine the photospheric velocities at all times, they are very important for studying the structure of the ejecta and comparing the cases of different SNe.

Figure 5.4 reproduces the Si II λ6355 and Ca II H&K velocity measurements of `SN 1999aa` from **Paper III**. The measurements are compared to those of other SNe Ia. The behavior of Ca II H&K is similar to the one found for normal SNe Ia, with a fast decline before maximum light and a slower decline after two weeks from maximum light. The spectra at three and one day before maximum light show a double absorption profile, which was taken as a whole to fit a single Gaussian profile. The Si II λ6355 velocities are peculiar in the case of `SN 1999aa`. As in the case of other peculiar objects, namely `SN 1991T` and `SN 2000cx`, the velocities do not show the usual decrease with time but remain constant well after maximum light. This is believed to be a consequence of the line being formed in a layer separated from the photosphere (above a certain point in velocity space). It is noted in both panels that SNe with fast-declining lightcurves (namely, `SN 1991bg` and `SN 1999by`) show lower expansion velocities than normal, especially in Si II λ6355.

Si II ratios. The ratio, $\mathcal{R}$(Si II), of the depth of Si II λ5972 to that of Si II λ6355 in near-maximum spectra was defined by Nugent et al. [49] as a spectral parameter which correlates with absolute peak magnitude —and therefore, with the decline rate of the lightcurve. The authors were able to reproduce this correlation by modeling a spectral sequence of synthesized spectra parameterized by the effective temperature. $\mathcal{R}$(Si II) (or *silicon ratio*) is a measure of the strength of the event. For SNe with slowly declining lightcurves (more powerful), $\mathcal{R}$(Si II) is smaller. In the case of fast-declining SNe, the silicon ratios are larger, with the extreme case of `1991bg`-like SNe. In fact, for these peculiar SNe, the absorption seen at $\sim$5800 Å is due to a strong component of Ti II instead of the usually weaker Si II. Figure 5.5 shows the measurement of $\mathcal{R}$(Si II) for several SNe Ia plotted versus the lightcurve-shape parameter $\Delta m_{15}(B)$, as presented in **Paper D**. The correlation mentioned above can be seen clearly from the plot.

Heterogeneity. As seen above, the heterogeneities in peak luminosities of SNe Ia (including peculiar objects) can be accounted for with the $\mathcal{R}$(Si II) parameter, in a similar manner as with the lightcurve-shape parameters. However, other heterogeneities found in SN Ia spectra that have to do with expansion velocities, do not respond to the same correlation. A standard measure of expan-

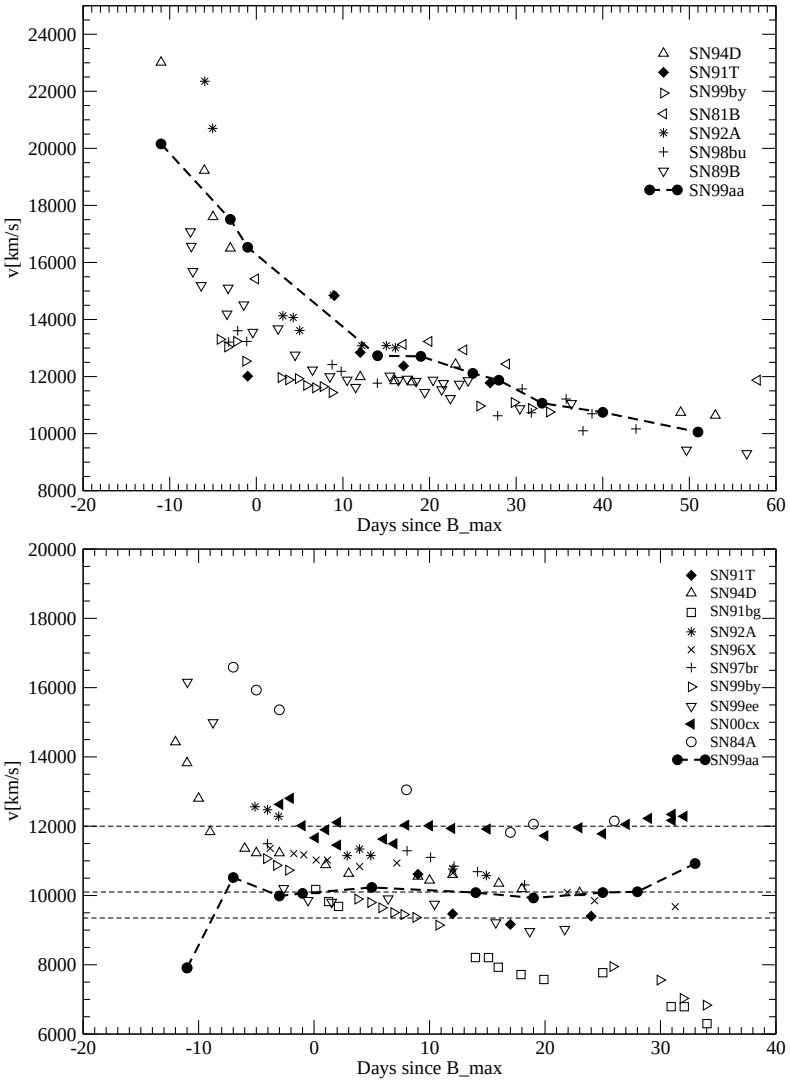

Figure 5.4: Velocities corresponding to the Doppler shifts of the absorption minima of Ca II H&K (*upper panel*) and Si II λ6355 (*lower panel*). The measurements for `SN 1999aa` are compared with those of other low-z SNe Ia. The behavior of Ca II H&K is similar to that of normal SNe. Instead, the velocity of Si II λ6355 for `SN 1999aa` maintains a constant level from maximum light to 20 days after, similarly to the peculiar `SN 1991T` and `SN 2000cx`. (See references in **Paper III**).

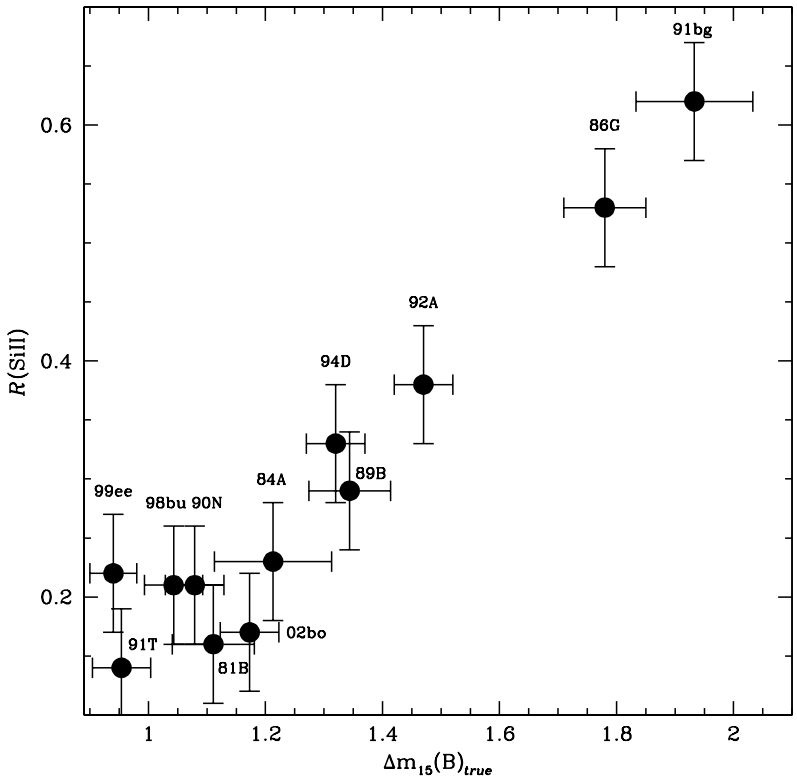

Figure 5.5: Silicon ratios $\mathcal{R}$(Si II) [49] measured at maximum light versus the lightcurve parameter $\Delta m_{15}(B)$, as shown in **Paper D**. A correlation between the two parameters is seen.

sion velocities is the parameter v_{10}(Si II), defined as the velocity corresponding to the minimum of Si II λ6355 measured 10 days after maximum light. Hatano et al. [26] show that there is no evident correlation between $\mathcal{R}$(Si II) and v_{10}(Si II) (see Figure 5.6). Even discarding the peculiar SNe (marked with arrows in the plot), there is a wide range of velocities for SNe with the same value of the silicon ratio. This means that the spectral diversity of SNe Ia cannot be accounted for with a one-parameter sequence. The authors suggest that this may be an indication of the coexistence of different explosion mechanisms giving rise to SNe Ia.

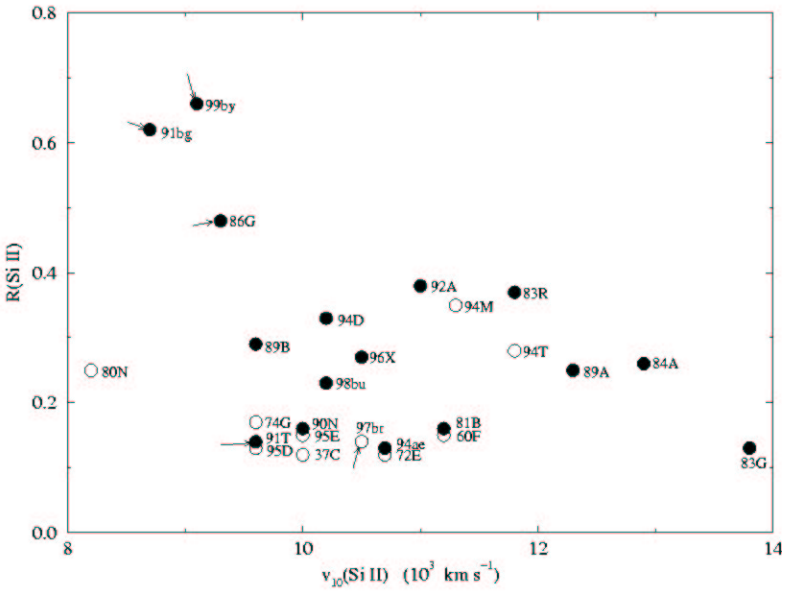

Figure 5.6: The parameters $\mathcal{R}$(Si II) and v_{10}(Si II) show no evident correlation. The arrows mark peculiar SNe Ia. The open circles correspond to values of $\mathcal{R}$(Si II) obtained through a relation between $\Delta m_{15}(B)$ and $\mathcal{R}$(Si II). Credit: [26].

5.2 Newly Defined Spectral Measurements (EW)

Based on the observation that different subtypes of SNe Ia generally show absorption features of different strengths, a set of measurements similar to equivalent withs (EW) have been defined as a way to quantify these strengths. **Paper II** presents the study of these EW measurements applied to a large set of spectra

from the SCP Spring '99 campaign (see Section 4.1) and other published data. The present Section is concerned with the topics of that paper. Some of the results are also given in **Paper E**.

The measurements are used to quantify both the spectral evolution with phase and the degree of homogeneity among SNe Ia, and to search for correlations between spectral properties and peak luminosities that may further refine the calibration of the standard candle.

Measurement description

The definition of the eight spectral features where the EW measurements are done is given in Section 3 of **Paper II**. The features are defined based on the strongest absorption troughs present in near-maximum SN Ia spectra. As the spectrum evolves from the earliest stages to about two months after maximum light, the wavelength range covered by each feature changes according to the definitions given in the paper. Figure 5.7 shows an example of the change in the definitions at three different epochs. The inset graph shows the differences seen in the region of features #2 and #3 for near-maximum spectra of the peculiar `SN 1991T` and `SN 1991bg`, and the normal `SN 1989B`.

In order to measure the EW, a *pseudo-continuum* is traced between the feature limits. A region around each of the limits is selected to do the fit of a straight line which represents the pseudo-continuum. Figure 5.8 shows an example of such fit. The spectrum is divided by the pseudo-continuum and the EW is computed as the area (in units of Å) between unity and the result of the division. As a consequence of the division by the pseudo-continuum, the EW measurements are distance-independent and can thus be directly used to compare different SNe.

These calculations have been implemented through a `FORTRAN` program which can alternatively be run in an interactive mode. The program computes statistical uncertainties by error propagation. Also, uncertainties introduced by the choice of the pseudo-continuum fitting regions on each side of the feature are taken into account. This is done by randomly shifting the two fitting regions and computing the r.m.s. of the resulting EW measurements. The size of the shifts is determined by the width of the fitting regions. Based on the second moment of a uniform distribution of width l, a maximum shift of $l/\sqrt{12}$ was taken in this simulation. These uncertainties were added quadratically to the statistical uncertainties of a single measurement. The uncertainties derived from the position of the pseudo-continuum fitting regions were dominant in the cases of high signal-to-noise ratio spectra.

Other implementations. The code additionally allows to measure the flux, intensity and centroid of lines. Also, it can be used to fit simple line profiles (e.g., Gaussian) and perform line *deblends* by simultaneous profile fits on a complex feature. Figure 5.9 shows the implementation of the program to deblend a

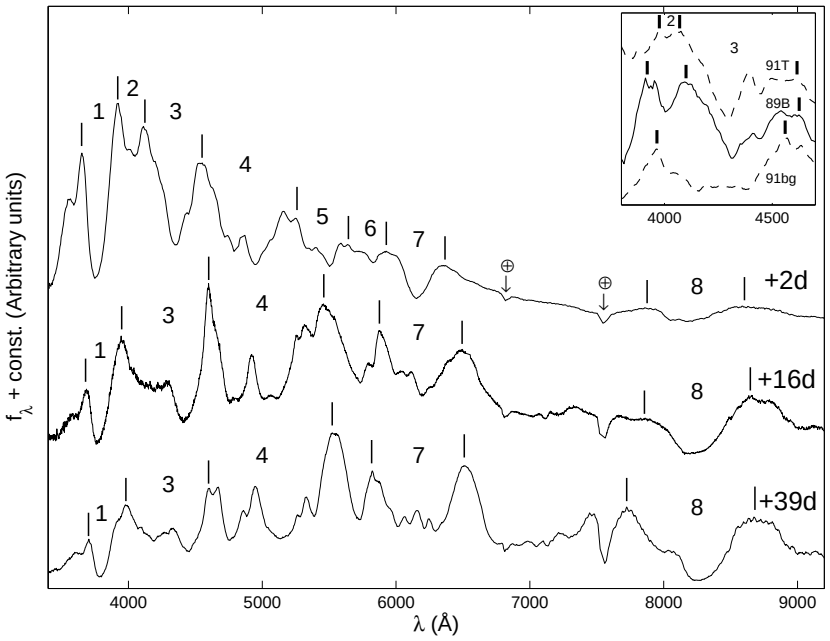

Figure 5.7: SNe Ia spectral evolution and feature definitions, as given in **Paper II**, for three epochs: 2, 16 and 39 days after maximum light. Numerical labels correspond to the following adopted feature names: **1**- "Ca II H&K"; **2**- "Si II 4000"; **3**- "Mg II 4300"; **4**- "Fe II 4800"; **5**- "S II W"; **6**- "Si II 5800"; **7**- "Si II 6150"; and **8**- "Ca II IR". Short vertical lines show the approximate positions where the pseudo-continuum is taken in each case. Feature ranges change with time and, due to blending, some weaker features are not considered at later epochs. Note that, as the SNe leave the photospheric phase, pseudo-continuum points correspond to emission peaks. *Inset panel*: the region of features #2 and #3 for near-maximum spectra of `SN 1991T` (top), `SN 1989B` (middle), and `SN 1991bg` (bottom). Feature #2 is not defined in the case of 1991bg-like SNe. Adopted feature limits are marked with vertical lines.

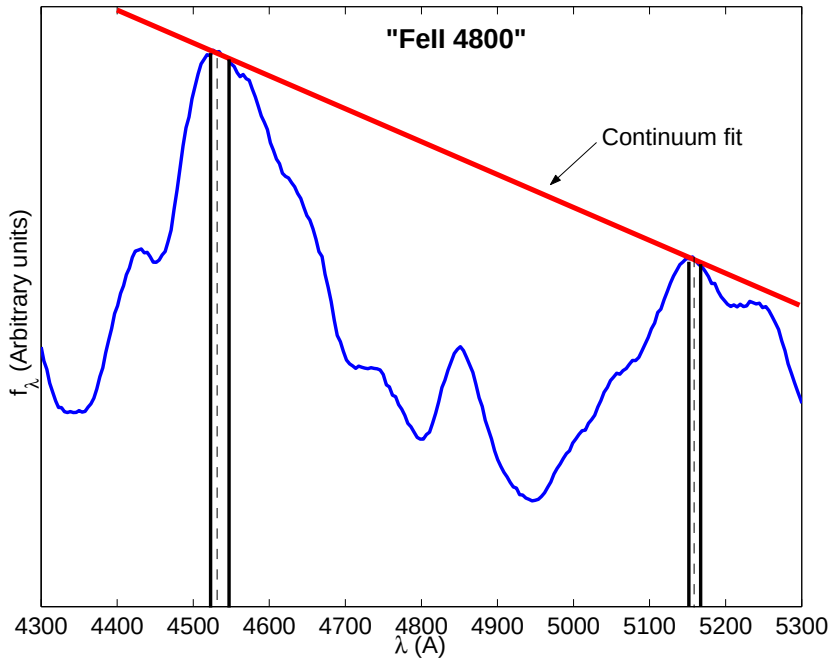

Figure 5.8: Example of an EW measurement. The pseudo-continuum is fitted as a straight line passing through the points inside the two regions marked by the vertical solid line. The dashed vertical lines show the feature limits for this case.

feature in 5 Gaussian absorption profiles. It should be noted, though, that single lines in SN spectra usually present P Cygni profiles and cannot be modeled in the presented manner. The measurements of deblended lines, considered as empirical, can be used in future analysis.

Tests for systematic effects. In addition to the variation of the pseudo-continuum fitting regions, a number of possible systematic effects related to the data quality were tested, as described in Section 3.3 of **Paper II**. The effect of varying resolutions, signal-to-noise ratios and uncorrected reddening were simulated in turn. Figure 5.10 shows examples of the tests performed. Within the ranges of resolution and signal-to-noise ratio of the present data, the effects were found to be negligible. The top panels in Figure 5.10 show the effect of changing resolution on the EW measurements (for cases with dispersions of 2, 6 and 10 Å/pix). A slight decrease in EW is found, but the differences are not statistically significant even for this high signal-to-noise spectrum. Due to the large line broadening of SN spectra, the available resolutions are adequate to obtain accurate measurements. An example of a test for the effect of noise is shown in the middle panels of Figure 5.10. Again, no significant differences were found for a range of signal-to-noise ratios between ∼1 and several hundred. The same was true for a range of reddening corresponding to $0 < A_V < 1.0$ and using the extinction law from Cardelli et al. [13]. The bottom panels in Figure 5.10 show that reddening introduces a slight reduction in EW, although the differences are not statistically significant.

The systematic effect produced by residual host-galaxy contamination was also tested. In general, a positive residual contamination (because of an under-estimation of the host-galaxy level) would decrease the measured value of EW. For a given fraction of host-galaxy flux in the total integrated flux (also negative values can be considered due to over-subtraction), the size of the effect for each feature depends on the phase of the SN spectrum and on the Hubble type of the host galaxy. For each measurement, the effect can therefore be simulated with an estimate of the host-galaxy contamination and the knowledge of the galaxy type, and an uncertainty can be given. It was found that, for residual contamination levels of ∼5%, the size of the effect on the EW is <8%. Figure 5.11 shows an example of the effect of contamination by the host galaxy on the relatively weak feature #2 (called "Si II 4000") near maximum light, for different types of galaxies.

Spectral Homogeneity

Section 4 of **Paper II** presents the EW measurements as a function of phase for each of the eight features defined, as a way to characterize the spectral evolution of SNe Ia. These measurements are reproduced in Figures 5.12 (features #1 to #4) and 5.13 (features #5 to #8). The emphasis is put in the study of homogeneity among normal SNe Ia and differences between normal and peculiar

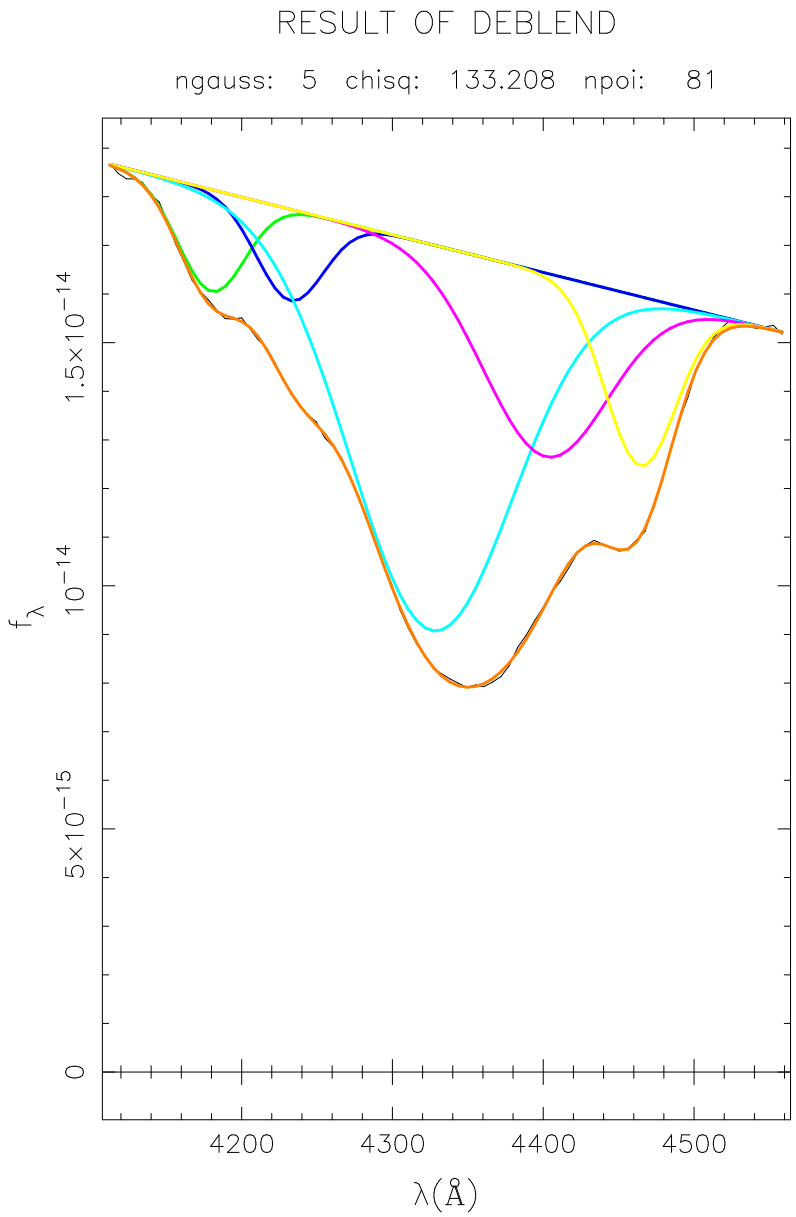

Figure 5.9: Example of other applications of the EW measuring code. A complex SN feature is "deblended" in 5 Gaussian absorptions. Each Gaussian fit produces a value of EW, intensity, flux and centroid position. Note that, in general, a Gaussian model is not accurate to represent SN features.

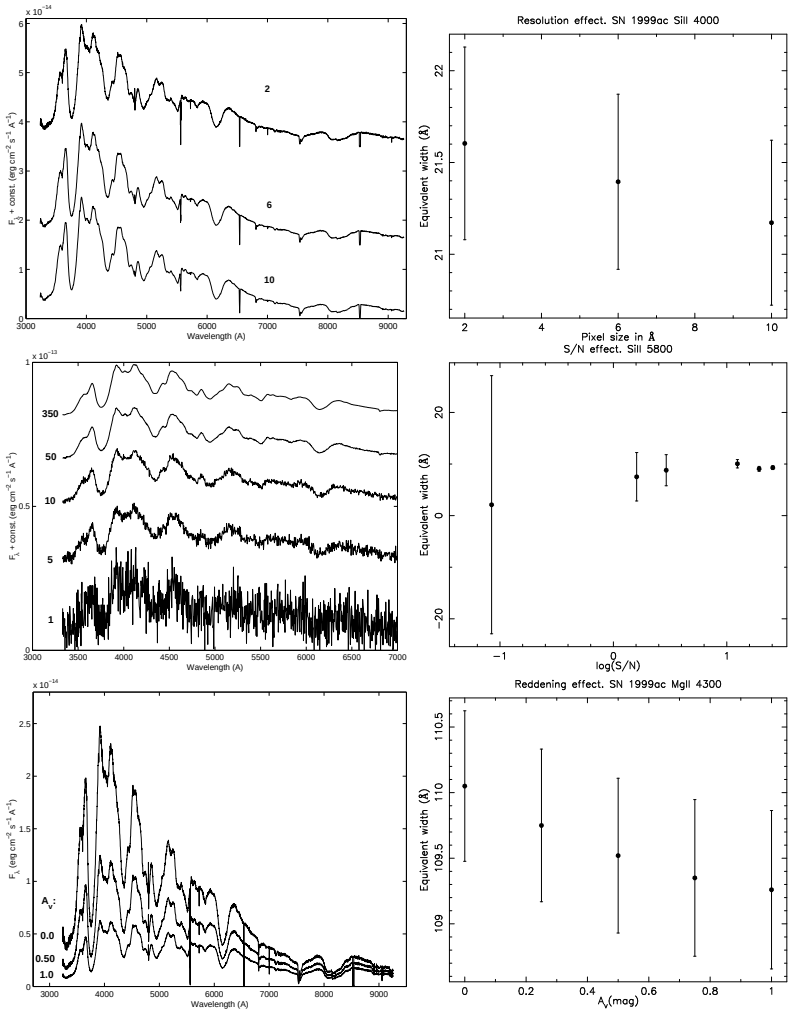

Figure 5.10: Examples of tests for possible systematic effects on EW measurements. *Upper panels*: The effect of resolution. The spectra in the left-hand panel were smoothed to reproduce the dispersions indicated (in Å). The right-hand panels show no significant variations. *Middle panels*: The effect of noise. The spectra in the left-hand panel were artificially deteriorated to reproduce the indicated signal-to-noise ratios. No significant deviations were found. *Lower panels*: The effect of reddening. The spectra in the left-hand panel were treated to reproduce the indicated extinction levels (from $A_V = 0$ to $A_V = 1$ mag). Again, no significant effect is observed.

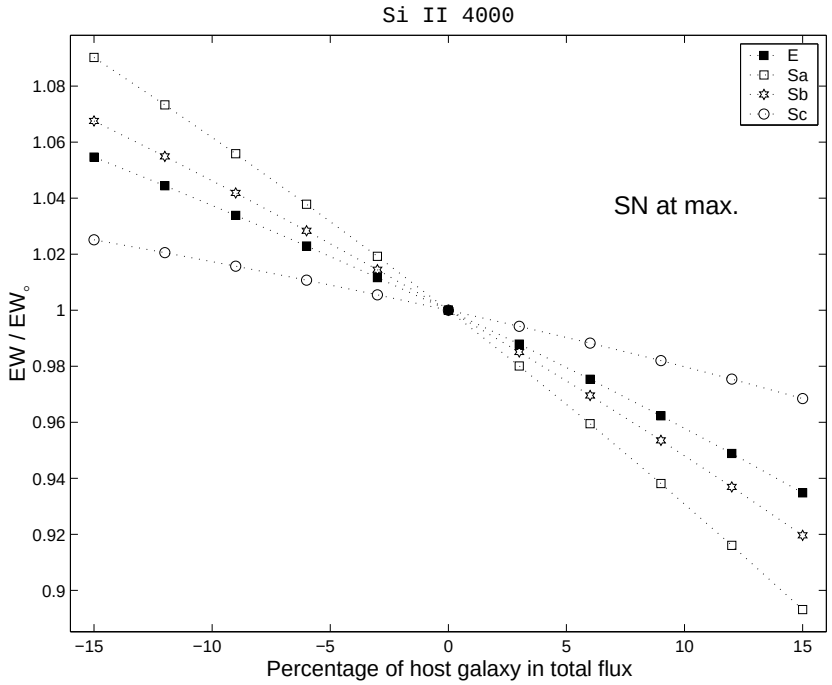

Figure 5.11: The effect of residual host-galaxy contamination on the EW. This is the example of a test done on "Si II 4000" for a SN spectrum at maximum light and different host galaxy Hubble types. The values of EW measured relative to the non-contaminated case are plotted versus the percentage of host galaxy in the total flux. Note that *negative* contamination levels (i.e., over-subtracted host-galaxy flux) are considered. This exercise can be repeated for any epoch and feature under consideration.

SNe that would provide a quantified classification method. For features #3, #4, #6 and #8, empirical curves were built to represent the average evolution with phase of normal SNe Ia (see Figures 2, 3, 4 and 7 in the paper). These curves were used to calculate the intrinsic scatter among normal SNe and the divergences of peculiar objects (see Tables 5 to 8 in the paper). In general, the estimated dispersions around the average curves for normal SNe are between ~5% and ~30%, depending on the feature and epoch. The EW values for 1991T-like SNe generally evolve parallel to the curves, but systematically below them. For 1991bg-like objects, the opposite is true: the features are usually stronger and the EW's are thus larger. Their evolution with phase is also roughly parallel to the curves for normal SNe. The differences among the three subtypes, considered in relative terms, are enhanced in the cases of the two weakest Si II features, "Si II 4000" and "Si II 5800" (see Figures 5 and 6 in the paper). The behavior of "Ca II H&K" (Figure 8 in the paper) is generally more complex, with a trend of decreasing EW with time, as opposed to all other features which show growing EW's.

Correlations with Luminosity

Section 5 of **Paper II** presents the study of spectral parameters based on EW measurements and their possible correlation with absolute peak magnitude (e.g., in B-band, $M_B^{\max}$). Table 5.1 gives a summary of some spectral parameters found to correlate with $M_B^{\max}$. The table lists the name of the spectral parameter (defined below), the number of SNe measured, the reduced χ^2 of a linear fit, the residual dispersion around the fit, and the coefficients of the fit.

The silicon ratio parameter defined by Nugent et al. [49] (see Section 5.1) was reproduced using EW's instead of line depths. The correlation with absolute peak magnitude is comparable for both definitions of the ratio, as shown in Figure 10 of the paper and in Table 5.1. The ratio of EW's may present the advantage of a more robust computation in the case of low signal-to-noise ratio spectra.

The behavior of feature #3 ("Mg II 4300") with SN phase provides a new spectral parameter which correlates linearly with the lightcurve-shape parameter $\Delta m_{15}(B)$ and thus, with peak luminosity. This parameter, called t_{br}, is related to the epoch at which the EW of this feature presents a sudden increase. This epoch is found to vary according to the lightcurve decline rate. This step-like behavior is modeled for each SN by a parametrized function of epoch (t):

$$f(\vec{\theta}, t) = \frac{A}{e^{\frac{t_{br}-t}{\tau}} + 1} + B, \tag{5.1}$$

where the parameters are $\vec{\theta} = (A, B, t_{br}, \tau)$. Thus, t_{br} can be obtained for each SN with good coverage over the time when the sudden increase occurs. Figure 11 in the paper shows the correlations of t_{br} with $\Delta m_{15}(B)$ and $M_B^{\max}$.

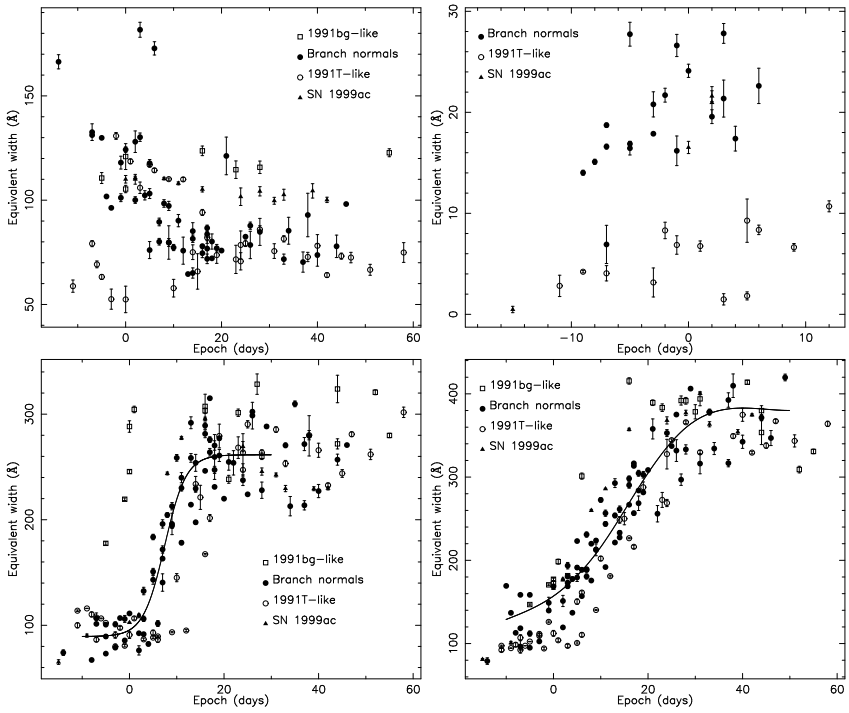

Figure 5.12: Results of the EW measurements on low-z SN spectra, as given in **Paper II**. The evolution with phase of features #1 to #4, sorted by feature number, from left to right and from top to bottom. The solid lines represent the average models for normal SNe Ia, as described in the paper. The error-bars include the measurement uncertainties and the error introduced by the choice of the pseudo-continuum fitting regions (see text).

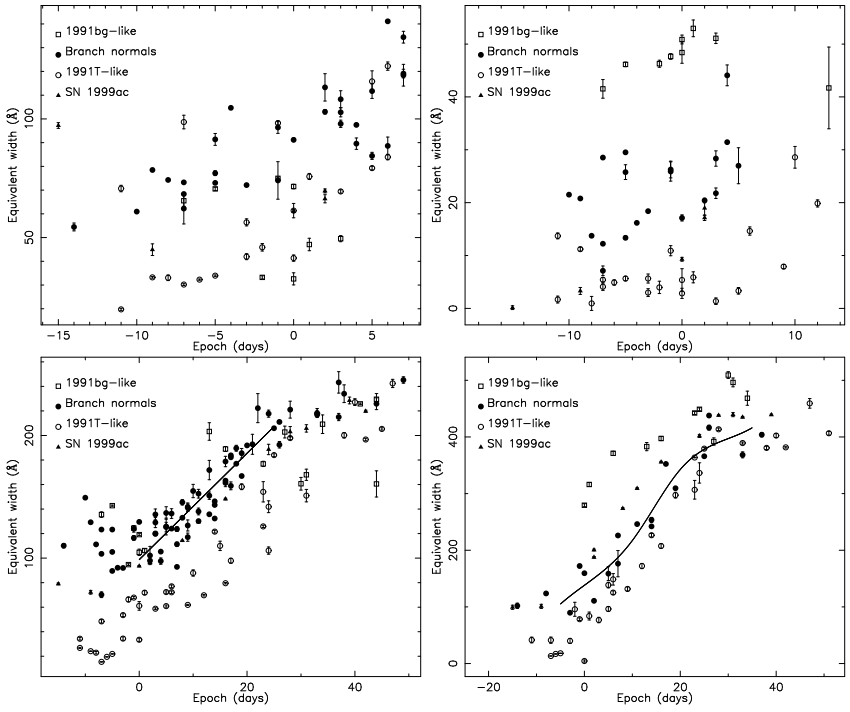

Figure 5.13: Results of the EW measurements on low-z SN spectra, as given in **Paper II**(cont.). The evolution with phase of features #5 to #8, sorted by feature number, from left to right and from top to bottom. The solid lines represent the average models for normal SNe Ia, as described in the paper. The error-bars include the measurement uncertainties and the error introduced by the choice of the pseudo-continuum fitting regions (see text).

The observation that 1991bg-like SNe (sub-luminous) show stronger features, and that 1991T-like SNe (slightly over-luminous) show weaker features suggests that some EW measurements would correlate with peak luminosity. This was investigated using the EW's of all eight features measured around the time of maximum light, where the bulk of the data was obtained. The EW's of single features or sums of these in various combinations were studied. In general, the strongest correlations found involved features #2, #3, #4, #6, #7 and #8.

In addition to the values at the epoch of maximum light, the behavior near that epoch was considered. In some cases, the evolution of the values with time was approximated by a straight-line which allowed to interpolate the values at the desired epoch, and provided with additional parameters: the slopes of those lines. Figure 5.14 shows an example of the computation of the values of EW at the time of maximum light ($\mathrm{EW}^{t_{\max}}$) and the slopes α for the sum of features #2 and #3. The graph shows the cases of the 1991bg-like SN 1986G, the normal SN 1989B, and the 1991T-like SN 1999aa. It is noted that as the the value of $\mathrm{EW}^{t_{\max}}$ increases, the slope α also increases. This behavior is found in the whole sample for several combinations of features, which gives rise to correlations of both $\mathrm{EW}^{t_{\max}}$ and α with $M_B^{\max}$. Some of the tightest correlations are listed in Table 5.1, and shown in Figures 5.15 and 5.16. It should be noted that, while measuring $\mathrm{EW}^{t_{\max}}$ requires one spectrum taken at maximum light, the calculation of the slopes α requires at least two spectra taken around the time of maximum light. However, as described in **Paper II**, since the effect of host-galaxy contamination is to lower (or rise, for over-subtraction) all the EW values, the slopes are expected to be more robust against this effect than quantities such as $\mathrm{EW}^{t_{\max}}$.

The example of the EW sum of features #2 and #3 and, in particular, its slope $\alpha_{(2+3)}$ is given in **Paper II**. This combination is important because it leads to the tightest correlation with $M_B^{\max}$ found for the present data, and its measurement is particularly convenient, since the features lie on a bright region of the spectrum which is visible in the optical range up to $z \sim 1$. The correlation between $\alpha_{(2+3)}$ and $M_B^{\max}$ reduces the scatter in the present sample (which includes peculiar SNe Ia) from 0.5 to 0.14 mag, a number which may be dominated by the uncertainties in the distances to the supernovae. If confirmed by larger data sets, $\alpha_{(2+3)}$ would allow a strong refinement of the standard candle, independently of the lightcurve properties. The requirement to obtain a value of $\alpha_{(2+3)}$ is two spectra covering the range ~3900 to ~4600 Å, obtained around maximum light. Other combinations of EW measurements, or their evaluation at different epochs, might prove equally or even more useful when tested on larger spectra samples.

5.3 Low- and High-Redshift Supernovae

As mentioned in Section 4.2, part of the set of high-redshift SN spectra obtained by the SCP using the *Very Large Telescope* (VLT) deserved further analysis.

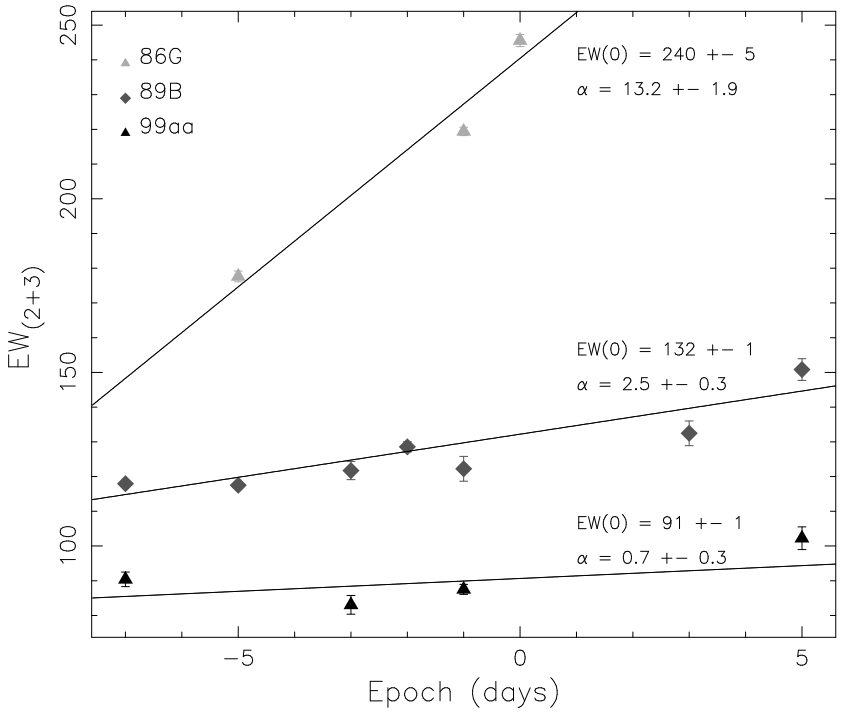

Figure 5.14: An example of the $\mathrm{EW}_{(2+3)}$ measurements around maximum light for a 1991bg-like SN (*top*), a normal SN Ia (*middle*), and a 1991T-like SN (*bottom*). The solid lines represent straight-line fits to the data used to determine both the values of the intercept $\mathrm{EW}_{(2+3)}^{t_{\max}}$, and slope $\alpha_{(2+3)}$.

Table 5.1: Correlations of spectral parameters with $M_B^{\max}$.

Spectral Parameter	n	χ^2_ν	σ_{M_B} (mag)	Linear fit Coefficients[a]
$\mathcal{R}$(Si II)	13	0.88	0.33±0.05	$a = -20.20 \pm 0.22$
				$b = 5.04 \pm 0.63$
$\mathcal{R}(\text{Si II})_{\text{EW}}$	13	1.15	0.39±0.09	$a = -20.03 \pm 0.16$
				$b = 5.91 \pm 0.60$
$\text{EW}^{t_{\max}}_{(3)}$	13	1.50	0.30±0.05	$a = -20.24 \pm 0.16$
				$b = 0.011 \pm 0.001$
$\alpha_{(3)}$	11	2.4	0.34±0.09	$a = -19.40 \pm 0.11$
				$b = 0.123 \pm 0.018$
$\text{EW}^{t_{\max}}_{(2+3)}$	13	1.23	0.29±0.05	$a = -20.43 \pm 0.18$
				$b = 0.012 \pm 0.001$
$\alpha_{(2+3)}$	10	0.23	0.14±0.03	$a = -19.27 \pm 0.10$
				$b = 0.103 \pm 0.025$
$\text{EW}^{t_{\max}}_{(2+3+4)}$	13	2.34	0.40±0.08	$a = -21.18 \pm 0.26$
				$b = 0.0082 \pm 0.0008$
$\alpha_{(2+3+4)}$	10	0.38	0.18±0.04	$a = -19.60 \pm 0.17$
				$b = 0.082 \pm 0.021$
$\text{EW}^{t_{\max}}_{(2+3+6)}$	13	1.17	0.29±0.04	$a = -20.33 \pm 0.17$
				$b = 0.0095 \pm 0.0009$
$\alpha_{(2+3+6)}$	9	0.74	0.30±0.09	$a = -19.13 \pm 0.10$
				$b = 0.099 \pm 0.028$

[a] Coefficients of a linear fit: $M_B^{\max} = a + b \cdot (\text{Spectral Parameter})$.

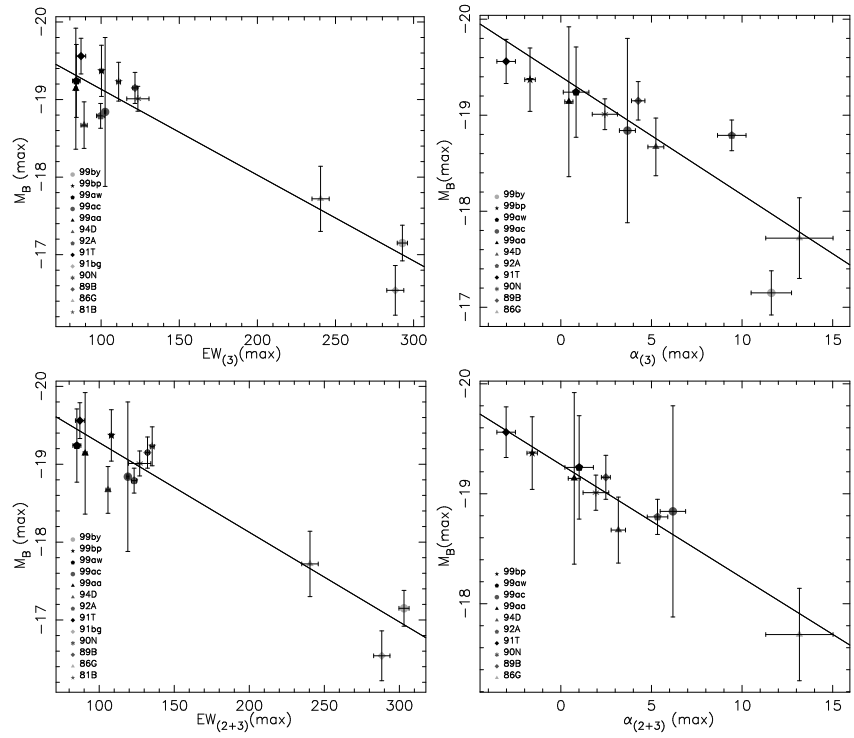

Figure 5.15: Examples of the correlations found between EW-related spectral parameters and $M_B^{\max}$ for the presented sample of SNe Ia. Parameters related to feature #3 and the sum (#2 + #3) are shown. The left-hand panels show intercept values ($\mathrm{EW}^{t_{\max}}$) for different feature combinations. The right-hand panels show the correlations for the corresponding slope parameters (α). The solid lines represent straight-line fits done to study the strength of the correlations. Table 5.1 summarizes the results of the fits.

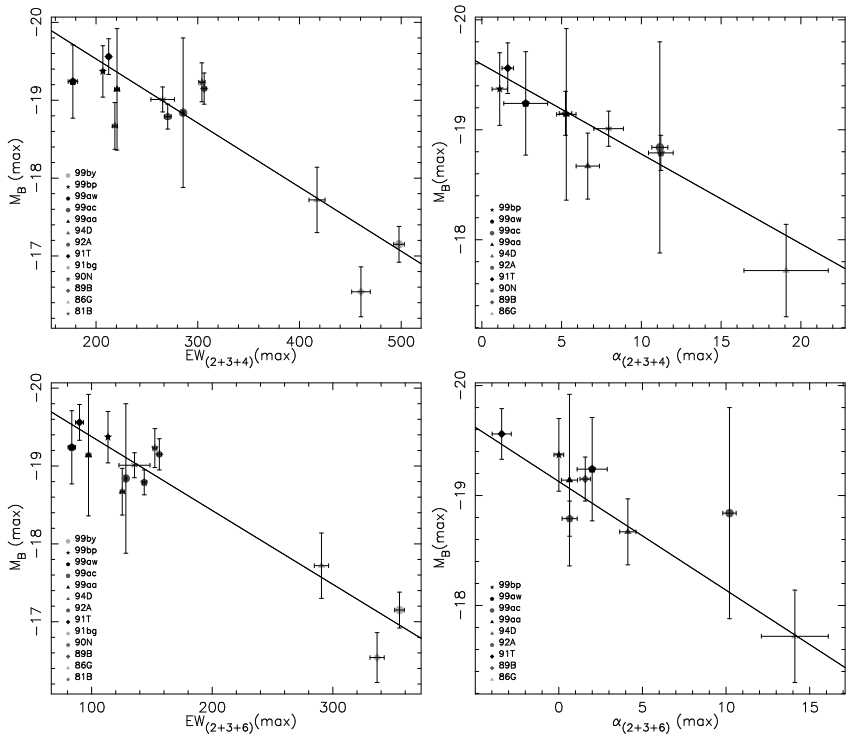

Figure 5.16: Examples of the correlations found between EW-related spectral parameters and $M_B^{\max}$ for the presented sample of SNe Ia (cont.). Parameters related to the sums of features (#2 + #3 + #4) and (#2 + #3 + #6) are shown. The left-hand panels show intercept values ($\mathrm{EW}^{t_{\max}}$) for different feature combinations. The right-hand panels show the correlations for the corresponding slope parameters (α). The solid lines represent straight-line fits done to study the strength of the correlations. Table 5.1 summarizes the results of the fits.

These spectra, originally intended to provide a secure classification and redshift of the discoveries, presented high enough quality to allow the measurements introduced for low-redshift SNe. **Paper IV** presents the measurements and analysis of 14 spectra from 12 SNe Ia (see Table 1 in the paper). The comparison of the results for low- and high-redshift samples aims to test the possibility of SN brightness evolution with redshift, which may mimic the effect of an accelerated expansion. This test is necessary to address a potential source of systematic effects in the cosmological parameters, as described in Section 3.5.

Velocities. For the high-redshift SNe, the velocity corresponding to the Doppler shift of the absorption minimum of Ca II H&K was measured. Other lines used to measure velocities of low-redshift SNe were either too faint or not covered by the spectra. Figure 5.17, extracted from **Paper IV**, shows the velocities of the high-z SNe compared to those of the nearby objects. No deviations between the samples are found. Furthermore, all the high-redshift SNe show higher velocities than the local sub-luminous SNe (`SN 1991bg` and `SN 1999by`).

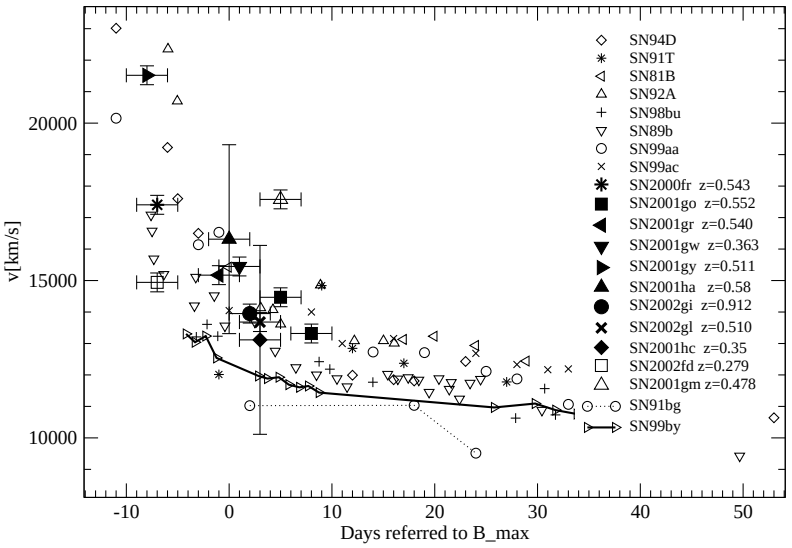

Figure 5.17: Ca II H&K velocities measured on the high-z SNe Ia observed at the VLT. This velocities are compared with those of a sample of low-z SNe. No deviations are found.

Equivalent widths. The rest-frame wavelength ranges covered by the VLT spectra generally allowed to measure the EW's of features #1 to #5, according to the definitions of **Paper II**. Figure 5.18 shows these measurements in

comparison with those of low-redshift SNe. Due to lower signal-to-noise ratios and greater uncertainties in the estimation of the host-galaxy contamination (see Section 4.2), the error bars are larger for high-z SNe. In general, there is no evidence of a significant discrepancy between high-redshift SNe and normal, low-redshift SNe, with the exception of SN 2002fd, as discussed below.

In the case of feature #3 ("Mg II 4300"), a trend for higher EW's around maximum light is noted for high-z SNe, although the data is consistent with the nearby sample with a probability of 15% (see Table 3 in **Paper IV**). SN 2001go, which was observed at three different epochs, follows the behavior of nearby SNe, with a sudden increase in EW about one week after maximum light.

A peculiar SN at $z = 0.279$. The case of SN 2002fd, the SN with the lowest redshift in the VLT sample, is of special interest. Already from a qualitative analysis of its host-galaxy subtracted spectrum, the evidence is found for it to be a peculiar SN, similar to SN 1991T and SN 1999aa. This is determined by the weakness of the Si II and Ca II H&K lines, as shown in Figure 5.19. SN 2002fd is the first 1991T-like SN confirmed at such high redshift, suggesting that the SN population might be equal to the one in the local Universe. From the strengths of the absorption features, this SN can be considered as an intermediate case between SN 1991T and SN 1999aa, which adds evidence to the hypothesis that there is a continuous variation of spectral properties from normal to 1991T-like SNe. The EW measurements confirm the qualitative analysis, in particular, in the case of "Ca II H&K", which before maximum light, emphasizes the difference between SN 1991T and normal SNe Ia.

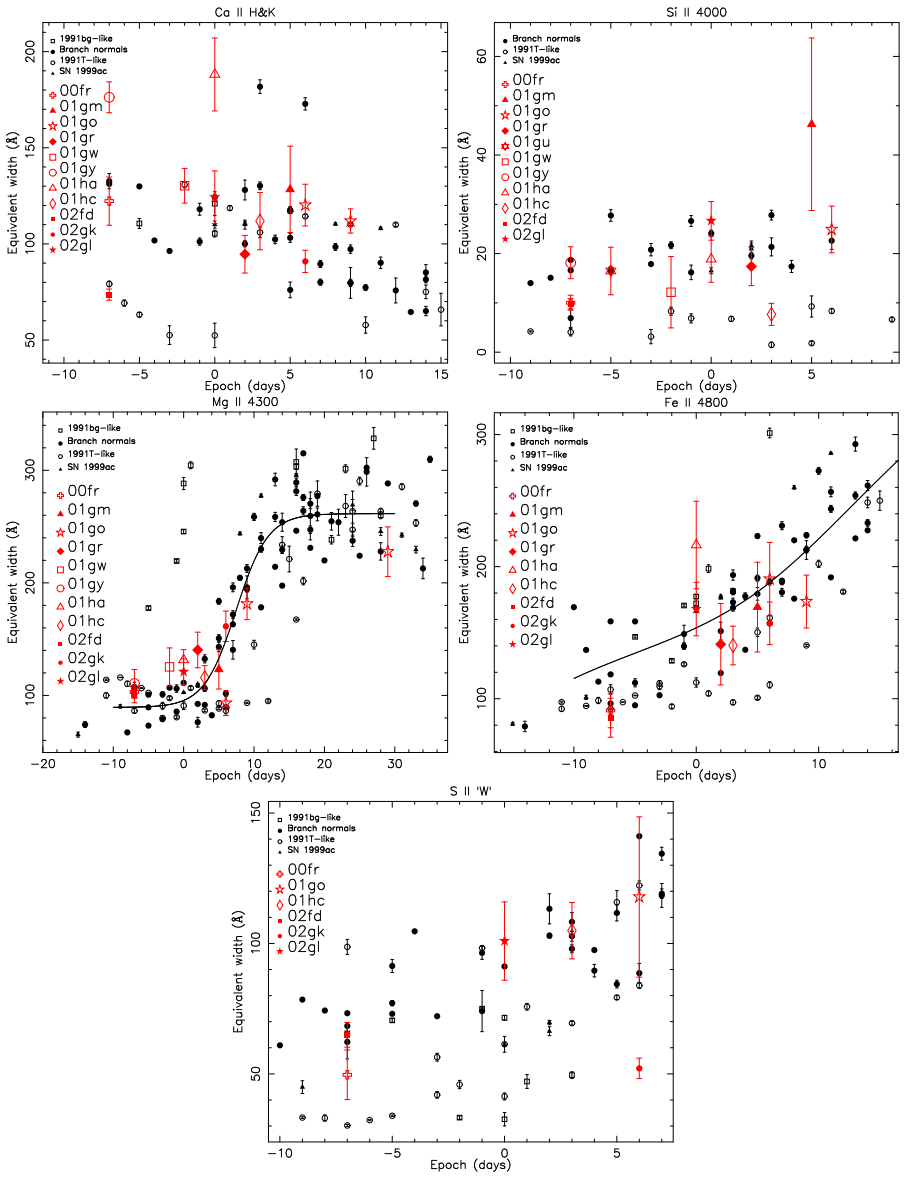

Figure 5.18: Comparisons of the EW measurements on spectra of low-z (*smaller symbols*) and high-z (*larger, gray symbols*) SNe Ia for features #1 to #5. The solid lines represent the average evolution of the normal SNe Ia in the low-z sample, as given in **Paper II**. No significant differences are seen between the two samples.

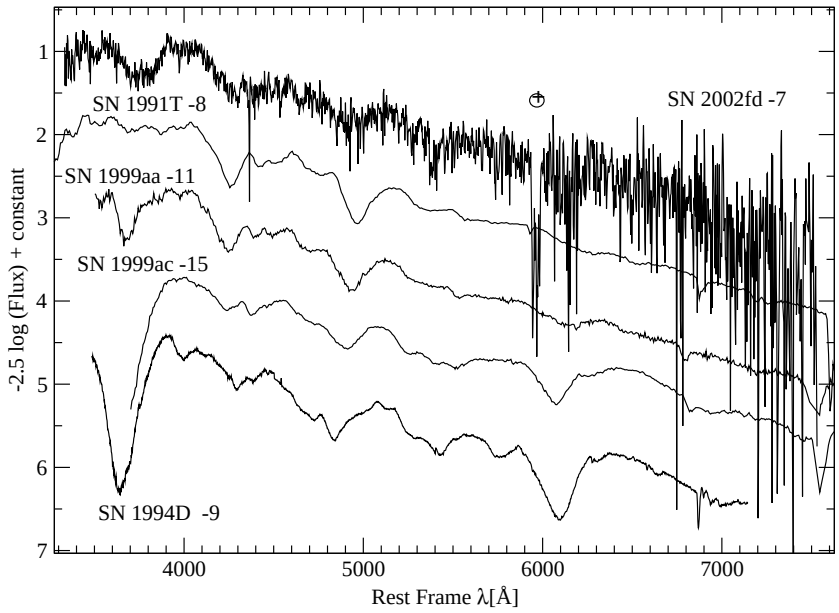

Figure 5.19: Comparison of the spectrum of `SN 2002fd` at $z = 0.279$, observed one week before maximum light, with those of nearby SNe Ia at similar epochs. `SN 2002fd` appears to be an intermediate case between `SN 1991T` and `SN 1999aa`, adding support to a continuous variation of spectral properties between normal and `1991T`-like SNe.

Chapter 6

Summary

The main purpose of this thesis is to introduce tools that would allow a quantitative analysis of type Ia supernova (SN Ia) spectra, with the ultimate goals of improving our understanding of these objects and increasing their quality as distance indicators.

In the past years, SNe Ia have been successfully exploited as excellent distance indicators and used to measure the energy content of the Universe through the distance–redshift relation. The results indicate that the Universe is undergoing a phase of accelerated expansion caused by an unknown component of the cosmic fluid with negative equation-of-state parameter. This exciting result has been corroborated by measurements of the geometry from the cosmic microwave background radiation which point to a flat Universe, and studies of the large-scale structure of matter, the dynamics of galaxy clusters and weak gravitational lensing which favor a Universe with a sub-dominant component of non-relativistic matter (mostly in the form of dark matter).

Nevertheless, our current knowledge of the physical processes involved in a SN Ia event is limited. The exact nature of the progenitor system and explosion mechanism leading to a SN Ia are topics of active research. Also, systematic effects of evolutionary or environmental origin that may hamper the accuracy of the measurements need to be thoroughly addressed. As the amount of high-quality supernova data keeps being gathered, and statistical uncertainties in the measured cosmological parameters are reduced, the control of potential systematic effects becomes crucial.

The information provided by spectra on the physical properties of SNe Ia plays a principal role in this respect. Qualitative spectral analysis and comparisons serve in classifying SNe Ia and detecting peculiarities. However, a quantitative approach is needed to carry out statistically robust studies. In addition, these studies may provide new ways of improving the properties of SNe Ia as distance indicators.

This work presents quantitative spectral analyses developed by introducing

a thorough data treatment method and a set of newly defined spectral measurements. The observational data is treated in order to produce calibrated spectra in a standardized manner and, most importantly, with estimated statistical and systematic uncertainties. The newly defined spectral measurements, similar to equivalent widths, are used to study the properties of a large number of low-redshift SNe Ia. In particular, the evolution with phase of the most prominent spectral features is quantified, and the degree of homogeneity among the supernovae is assessed. Based on the measurements, a number of spectral parameters are defined and their possible correlation with the luminosity at maximum light is studied, in the search of a further refinement of the standard candle. One such parameter is found to reduce the dispersion in the distance estimation of the sample studied to a value below 6%, which, if confirmed by larger data-sets, is comparable with the precision attained by currently used lightcurve shape – luminosity correlations.

The same measurements were applied to spectra of high-redshift SNe Ia in order to test the possibility of evolution with redshift. The results from the low- and high-redshift samples are compatible, thus providing no evidence of brightness evolution.

List of Figures

2.1 Theoretical Hubble diagram 13
2.2 Theoretical Hubble diagram for dark energy 15

3.1 Supernova Classification 19
3.2 Spectra of SN Ia subtypes 20
3.3 Lightcurve stretch parameter 22
3.4 Local Hubble diagram for SNe Ia 24
3.5 Optical passbands 28
3.6 Simulated Ω_M–Ω_Λ confidence regions 30
3.7 Dependence of m on z 31
3.8 Color excess histograms 34
3.9 Measured Hubble diagram 35
3.10 Measured Ω_M–Ω_Λ confidence regions 36
3.11 Hubble diagram for the 11 HST SNe 37
3.12 Confidence regions for different treatments of extinction 38
3.13 Combined confidence regions in Ω_M–Ω_Λ 40
3.14 Confidence regions in Ω_M–w 42

4.1 Finding chart for a low-z SN 49
4.2 Reduction log 51
4.3 Reduction log (cont.) 52
4.4 Extraction 55
4.5 Arc-lamp lines 56
4.6 Airmass distribution. 63
4.7 Redshifts and epochs of Spring '99 SNe Ia 63
4.8 Host-galaxy spectra 65
4.9 Host-galaxy spectra (cont.) 66
4.10 Host-galaxy spectra (cont.) 67
4.11 Host-galaxy subtraction test 69
4.12 Spring '99 spectra (1) 71
4.13 Spring '99 spectra (2) 72
4.14 Spring '99 spectra (3) 73
4.15 Spring '99 spectra (4) 74

4.16 Spring '99 spectra (5) . . . 75
4.17 Spring '99 spectra (6) . . . 76
4.18 Spring '99 spectra (7) . . . 77
4.19 Spring '99 spectra (8) . . . 78
4.20 Spring '99 spectra (9) . . . 79
4.21 Spring '99 spectra (10) . . . 80
4.22 Spring '99 spectra (11) . . . 81
4.23 Spring '99 spectra (12) . . . 82
4.24 Spring '99 spectra (13) . . . 83
4.25 Spring '99 spectra (14) . . . 84
4.26 Problematic Spring '99 spectra . . . 85
4.27 Finding chart of a high-z SN . . . 88
4.28 Background subtraction techniques . . . 90
4.29 Redshifts and epochs of the 12 high-z SNe Ia . . . 91

5.1 SN spectrum formation process . . . 94
5.2 `SYNOW` spectrum . . . 96
5.3 Spectral time series of `SN 1999aa` . . . 98
5.4 Velocities of `SN 1999aa` . . . 100
5.5 Silicon ratios . . . 101
5.6 Silicon ratios vs. velocities . . . 102
5.7 EW feature definitions . . . 104
5.8 EW measurement . . . 105
5.9 Deblend fit . . . 107
5.10 EW measurement tests . . . 108
5.11 Host contamination and EW . . . 109
5.12 EW measurements for low-z SNe (1) . . . 111
5.13 EW measurements for low-z SNe (2) . . . 112
5.14 Definition of an EW slope parameter . . . 114
5.15 Correlations of EW parameters with peak luminosity (1) . . . 116
5.16 Correlations of EW parameters with peak luminosity (2) . . . 117
5.17 Velocities of high-z SNe Ia . . . 118
5.18 EW measurements for high-z SNe . . . 120
5.19 A peculiar SN Ia at $z = 0.279$ . . . 121

List of Tables

4.1 Spectra reduction steps 54
4.2 Wavelength calibration uncertainties 57
4.3 Standard star observations 58
4.4 The 19 followed-up Spring '99 SNe Ia. 64

5.1 Correlations of spectral parameters with $M_B^{\max}$. 115

Bibliography

[1] G. Aldering. Type Ia supernovae and cosmic acceleration. In Stephen S. Holt and William W. Zhang. American Institute of Physics, editors, *Cosmic Explosions: Tenth Astrophysics Conference. AIP Conference Proceedings*, volume 522, pages 75–84, 2000.

[2] G. Aldering, R. Knop, and P. Nugent. The Rise Times of High- and Low-Redshift Type Ia Supernovae Are Consistent. *AJ*, 119:2110–2117, May 2000.

[3] S. W. Allen, R. W. Schmidt, and A. C. Fabian. Cosmological constraints from the x-ray gas mass fraction in relaxed lensing clusters observed with chandra. *MNRAS*, 334:L11–L15, April 2002.

[4] R. Amanullah, E. Mörtsell, and A. Goobar. Correcting for lensing bias in the Hubble diagram. *A&A*, 397:819–823, January 2003.

[5] B. J. Barris, J. L. Tonry, S. Blondin, P. Challis, R. Chornock, A. Clocchiatti, A. V. Filippenko, P. Garnavich, S. T. Holland, S. Jha, R. P. Kirshner, K. Krisciunas, B. Leibundgut, W. Li, T. Matheson, G. Miknaitis, A. G. Riess, B. P. Schmidt, R. C. Smith, J. Sollerman, J. Spyromilio, C. W. Stubbs, N. B. Suntzeff, H. Aussel, K. C. Chambers, M. S. Connelley, D. Donovan, J. P. Henry, N. Kaiser, M. C. Liu, E. L. Martín, and R. J. Wainscoat. Twenty-Three High-Redshift Supernovae from the Institute for Astronomy Deep Survey: Doubling the Supernova Sample at $z > 0.7$. *ApJ*, 602:571–594, February 2004.

[6] C. L. Bennett, M. Halpern, G. Hinshaw, N. Jarosik, A. Kogut, M. Limon, S. S. Meyer, L. Page, D. N. Spergel, G. S. Tucker, E. Wollack, E. L. Wright, C. Barnes, M. R. Greason, R. S. Hill, E. Komatsu, M. R. Nolta, N. Odegard, H. V. Peiris, L. Verde, and J. L. Weiland. First-Year Wilkinson Microwave Anisotropy Probe (WMAP) Observations: Preliminary Maps and Basic Results. *ApJS*, 148:1–27, September 2003.

[7] Lars Bergström and Ariel Goobar. *Cosmology and Particle Astrophysics (Second Edition)*. Praxis Publishing Ltd., Chichester, UK, 2004. ISBN 3-540-43128-4.

[8] J. P. Blakeslee, Z. I. Tsvetanov, A. G. Riess, H. C. Ford, G. D. Illingworth, D. Magee, J. L. Tonry, N. Benítez, M. Clampin, G. F. Hartig, G. R. Meurer, M. Sirianni, D. R. Ardila, F. Bartko, R. Bouwens, T. Broadhurst, N. Cross, P. D. Feldman, M. Franx, D. A. Golimowski, C. Gronwall, R. Kimble, J. Krist, A. R. Martel, F. Menanteau, G. Miley, M. Postman, P. Rosati, W. Sparks, L.-G. Strolger, H. D. Tran, R. L. White, and W. Zheng. Discovery of Two Distant Type Ia Supernovae in the Hubble Deep Field-North with the Advanced Camera for Surveys. *ApJ*, 589:693–703, June 2003.

[9] R. C. Bohlin, L. Colina, and D. S. Finley. White Dwarf Standard Stars: G191-B2B, GD 71, GD 153, HZ 43. *AJ*, 110:1316, September 1995.

[10] R. C. Bohlin, M. E. Dickinson, and D. Calzetti. Spectrophotometric Standards from the Far-Ultraviolet to the Near-Infrared: STIS and NICMOS Fluxes. *AJ*, 122:2118–2128, October 2001.

[11] S. Borgani, P. Rosati, P. Tozzi, S. A. Stanford, P. R. Eisenhardt, C. Lidman, B. Holden, R. Della Ceca, C. Norman, and G. Squires. Measuring Ω_m with the ROSAT Deep Cluster Survey. *ApJ*, 561:13–21, November 2001.

[12] D. Branch, A. Fisher, and P. Nugent. On the relative frequencies of spectroscopically normal and peculiar type Ia supernovae. *AJ*, 106:2383–2391, December 1993.

[13] J. A. Cardelli, G. C. Clayton, and J. S. Mathis. The relationship between infrared, optical, and ultraviolet extinction. *ApJ*, 345:245–256, October 1989.

[14] A. L. Coil, T. Matheson, A. V. Filippenko, D. C. Leonard, J. Tonry, A. G. Riess, P. Challis, A. Clocchiatti, P. M. Garnavich, C. J. Hogan, S. Jha, R. P. Kirshner, B. Leibundgut, M. M. Phillips, B. P. Schmidt, R. A. Schommer, R. C. Smith, A. M. Soderberg, J. Spyromilio, C. Stubbs, N. B. Suntzeff, and P. Woudt. Optical Spectra of Type Ia Supernovae at $z = 0.46$ and $z = 1.2$. *ApJL*, 544:L111–L114, December 2000.

[15] A. V. Filippenko. The importance of atmospheric differential refraction in spectrophotometry. *PASP*, 94:715–721, August 1982.

[16] W. L. Freedman, B. F. Madore, B. K. Gibson, L. Ferrarese, D. D. Kelson, S. Sakai, J. R. Mould, R. C. Kennicutt, H. C. Ford, J. A. Graham, J. P. Huchra, S. M. G. Hughes, G. D. Illingworth, L. M. Macri, and P. B. Stetson. Final Results from the Hubble Space Telescope Key Project to Measure the Hubble Constant. *ApJ*, 553:47–72, May 2001.

[17] G. Goldhaber, D. E. Groom, A. Kim, G. Aldering, P. Astier, A. Conley, S. E. Deustua, R. Ellis, S. Fabbro, A. S. Fruchter, A. Goobar, I. Hook, M. Irwin, M. Kim, R. A. Knop, C. Lidman, R. McMahon, P. E. Nugent,

R. Pain, N. Panagia, C. R. Pennypacker, S. Perlmutter, P. Ruiz-Lapuente, B. Schaefer, N. A. Walton, and T. York. Timescale Stretch Parameterization of Type Ia Supernova B-Band Light Curves. *ApJ*, 558:359–368, September 2001.

[18] A. Goobar. Cosmological parameters from type Ia supernovae. *Nuclear Physics B Proceedings Supplements*, 95:8–14, 2001.

[19] A. Goobar, E. Mörtsell, R. Amanullah, M. Goliath, L. Bergström, and T. Dahlén. SNOC: A Monte-Carlo simulation package for high-z supernova observations. *A&A*, 392:757–771, September 2002.

[20] A. Goobar and S. Perlmutter. Feasibility of Measuring the Cosmological Constant Λ and Mass Density Ω Using Type Ia Supernovae. *ApJ*, 450:14, September 1995.

[21] M. Hamuy, M. M. Phillips, N. B. Suntzeff, R. A. Schommer, J. Maza, A. R. Antezan, M. Wischnjewsky, G. Valladares, C. Muena, L. E. Gonzales, R. Aviles, L. A. Wells, R. C. Smith, M. Navarrete, R. Covarrubias, G. M. Williger, A. R. Walker, A. C. Layden, J. H. Elias, J. A. Baldwin, M. Hernandez, H. Tirado, P. Ugarte, R. Elston, N. Saavedra, F. Barrientos, E. Costa, P. Lira, M. T. Ruiz, C. Anguita, X. Gomez, P. Ortiz, M. della Valle, J. Danziger, J. Storm, Y.-C. Kim, C. Bailyn, E. P. Rubenstein, D. Tucker, S. Cersosimo, R. A. Mendez, L. Siciliano, W. Sherry, B. Chaboyer, R. A. Koopmann, D. Geisler, A. Sarajedini, A. Dey, N. Tyson, R. M. Rich, R. Gal, R. Lamontagne, N. Caldwell, P. Guhathakurta, A. C. Phillips, P. Szkody, C. Prosser, L. C. Ho, R. McMahan, G. Baggley, K.-P. Cheng, R. Havlen, K. Wakamatsu, K. Janes, M. Malkan, F. Baganoff, P. Seitzer, M. Shara, C. Sturch, J. Hesser, A. N. P. Hartig, J. Hughes, D. Welch, T. B. Williams, H. Ferguson, P. J. Francis, L. French, M. Bolte, J. Roth, S. Odewahn, S. Howell, and W. Krzeminski. BVRI Light Curves for 29 Type Ia Supernovae. *AJ*, 112:2408, December 1996.

[22] M. Hamuy, M. M. Phillips, N. B. Suntzeff, R. A. Schommer, J. Maza, and R. Aviles. The Absolute Luminosities of the Calan/Tololo Type Ia Supernovae. *AJ*, 112:2391, December 1996.

[23] M. Hamuy, M. M. Phillips, N. B. Suntzeff, R. A. Schommer, J. Maza, R. C. Smith, P. Lira, and R. Aviles. The Morphology of Type Ia Supernovae Light Curves. *AJ*, 112:2438, December 1996.

[24] M. Hamuy, N. B. Suntzeff, S. R. Heathcote, A. R. Walker, P. Gigoux, and M. M. Phillips. Southern spectrophotometric standards, 2. *PASP*, 106: 566–589, June 1994.

[25] M. Hamuy, A. R. Walker, N. B. Suntzeff, P. Gigoux, S. R. Heathcote, and M. M. Phillips. Southern spectrophotometric standards. *PASP*, 104:533–552, July 1992.

[26] K. Hatano, D. Branch, E. J. Lentz, E. Baron, A. V. Filippenko, and P. M. Garnavich. On the Spectroscopic Diversity of Type Ia Supernovae. *ApJL*, 543:L49–L52, November 2000.

[27] E. Hawkins, S. Maddox, S. Cole, O. Lahav, D. S. Madgwick, P. Norberg, J. A. Peacock, I. K. Baldry, C. M. Baugh, J. Bland-Hawthorn, T. Bridges, R. Cannon, M. Colless, C. Collins, W. Couch, G. Dalton, R. De Propris, S. P. Driver, G. Efstathiou, R. S. Ellis, C. S. Frenk, K. Glazebrook, C. Jackson, B. Jones, I. Lewis, S. Lumsden, W. Percival, B. A. Peterson, W. Sutherland, and K. Taylor. The 2dF Galaxy Redshift Survey: correlation functions, peculiar velocities and the matter density of the Universe. *MNRAS*, 346:78–96, November 2003.

[28] P. Höflich, A. Khokhlov, J. C. Wheeler, M. M. Phillips, N. B. Suntzeff, and M. Hamuy. Maximum Brightness and Postmaximum Decline of Light Curves of Type Ia Supernovae: A Comparison of Theory and Observations. *ApJL*, 472:L81, December 1996.

[29] P. Höflich, J. C. Wheeler, and F. K. Thielemann. Type Ia Supernovae: Influence of the Initial Composition on the Nucleosynthesis, Light Curves, and Spectra and Consequences for the Determination of Omega M and Lambda. *ApJ*, 495:617, March 1998.

[30] K. Horne. An optimal extraction algorithm for CCD spectroscopy. *PASP*, 98:609–617, June 1986.

[31] E. Hubble. A Relation between Distance and Radial Velocity among Extra-Galactic Nebulae. *Proceedings of the National Academy of Science*, 15: 168–173, March 1929.

[32] I. Iben and A. V. Tutukov. Supernovae of type I as end products of the evolution of binaries with components of moderate initial mass (M not greater than about 9 solar masses). *ApJS*, 54:335–372, February 1984.

[33] D. J. Jeffery and D. Branch. Analysis of Supernova Spectra. In *Supernovae, Jerusalem Winter School for Theoretical Physics*, pages 149, 1990.

[34] R. C. Kennicutt. A spectrophotometric atlas of galaxies. *ApJS*, 79:255–284, April 1992.

[35] A. Kim, A. Goobar, and S. Perlmutter. A Generalized K Correction for Type Ia Supernovae: Comparing R-band Photometry beyond $z = 0.2$ with B, V, and R-band Nearby Photometry. *PASP*, 108:190, February 1996.

[36] R. P. Kirshner and J. Kwan. Distances to extragalactic supernovae. *ApJ*, 193:27–36, October 1974.

[37] B. Leibundgut and G. A. Tammann. Supernova studies. III - The calibration of the absolute magnitude of supernovae of type Ia. *A&A*, 230:81–86, April 1990.

[38] W. Li, A. V. Filippenko, R. Chornock, E. Berger, P. Berlind, M. L. Calkins, P. Challis, C. Fassnacht, S. Jha, R. P. Kirshner, T. Matheson, W. L. W. Sargent, R. A. Simcoe, G. H. Smith, and G. Squires. SN 2002cx: The Most Peculiar Known Type Ia Supernova. *PASP*, 115:453–473, April 2003.

[39] W. Li, A. V. Filippenko, E. Gates, R. Chornock, A. Gal-Yam, E. O. Ofek, D. C. Leonard, M. Modjaz, R. M. Rich, A. G. Riess, and R. R. Treffers. The Unique Type Ia Supernova 2000cx in NGC 524. *PASP*, 113:1178–1204, October 2001.

[40] W. Li, A. V. Filippenko, R. R. Treffers, A. G. Riess, J. Hu, and Y. Qiu. A High Intrinsic Peculiarity Rate among Type Ia Supernovae. *ApJ*, 546: 734–743, January 2001.

[41] P. Lira. MS thesis. Universidad de Chile, 1995.

[42] K.G. Malmquist. *Medd. Lund Astron. Obs. Ser. II*, 32:64, 1924.

[43] K.G. Malmquist. *Stockholm Observatory Medd.*, 26, 1936.

[44] P. Massey and C. Gronwall. The Kitt Peak spectrophotometric standards - Extension to 1 micron. *ApJ*, 358:344–349, July 1990.

[45] D. L. Miller and D. Branch. Supernova absolute-magnitude distributions. *AJ*, 100:530–539, August 1990.

[46] R. Minkowski. Spectra of Supernovae. *PASP*, 53:224, August 1941.

[47] K. Nomoto. Accreting white dwarf models for type 1 supernovae. II - Off-center detonation supernovae. *ApJ*, 257:780–792, June 1982.

[48] P. Nugent, G. Aldering, and The Nearby Campaign. The Spring 1999 Nearby Supernovae Campaign. In *Supernovae and gamma-ray bursts: The Greatest Explosions Since the Big Bang: poster papers from the Space Telescope Science Institute Symposium, May 1999 / Mario Livio, Nino Panagia, Kailash Sahu, editors. [Baltimore, Md.] : Space Telescope Science Institute, [2000]., p.47*, pages 47, 2000.

[49] P. Nugent, M. Phillips, E. Baron, D. Branch, and P. Hauschildt. Evidence for a Spectroscopic Sequence among Type Ia Supernovae. *ApJL*, 455:L147, December 1995.

[50] J. E. O'Donnell. R_ν-dependent optical and near-ultraviolet extinction. *ApJ*, 422:158–163, February 1994.

[51] J. B. Oke. Faint spectrophotometric standard stars. *AJ*, 99:1621–1631, May 1990.

[52] J. B. Oke and A. Sandage. Energy Distributions, K Corrections, and the Stebbins-Whitford Effect for Giant Elliptical Galaxies. *ApJ*, 154:21, October 1968.

[53] J. Orear. *CLNS*, 496, 1981.

[54] B. Paczyński. Evolution of cataclysmic binaries. In *ASSL Vol. 113: Cataclysmic Variables and Low-Mass X-ray Binaries*, pages 1–12, 1985.

[55] S. Perlmutter, G. Aldering, M. della Valle, S. Deustua, R. S. Ellis, S. Fabbro, A. Fruchter, G. Goldhaber, D. E. Groom, I. M. Hook, A. G. Kim, M. Y. Kim, R. A. Knop, C. Lidman, R. G. McMahon, P. Nugent, R. Pain, N. Panagia, C. R. Pennypacker, P. Ruiz-Lapuente, B. Schaefer, and N. Walton. Discovery of a supernova explosion at half the age of the universe. *Nature*, 391:51, January 1998.

[56] S. Perlmutter, G. Aldering, S. Deustua, S. Fabbro, G. Goldhaber, D. E. Groom, A. G. Kim, M. Y. Kim, R. A. Knop, P. Nugent, C. R. Pennypacker, M. della Valle, R. S. Ellis, R. G. McMahon, N. Walton, A. Fruchter, N. Panagia, A. Goobar, I. M. Hook, C. Lidman, R. Pain, P. Ruiz-Lapuente, B. Schaefer, and The Supernova Cosmology Project. Cosmology From Type Ia Supernovae: Measurements, Calibration Techniques, and Implications. *Bulletin of the American Astronomical Society*, 29:1351, December 1997.

[57] S. Perlmutter, G. Aldering, G. Goldhaber, R. A. Knop, P. Nugent, P. G. Castro, S. Deustua, S. Fabbro, A. Goobar, D. E. Groom, I. M. Hook, A. G. Kim, M. Y. Kim, J. C. Lee, N. J. Nunes, R. Pain, C. R. Pennypacker, R. Quimby, C. Lidman, R. S. Ellis, M. Irwin, R. G. McMahon, P. Ruiz-Lapuente, N. Walton, B. Schaefer, B. J. Boyle, A. V. Filippenko, T. Matheson, A. S. Fruchter, N. Panagia, H. J. M. Newberg, W. J. Couch, and The Supernova Cosmology Project. Measurements of Omega and Lambda from 42 High-Redshift Supernovae. *ApJ*, 517:565–586, June 1999.

[58] S. Perlmutter et al. A supernova at $z = 0.458$ and the implications for measuring the cosmological deceleration. *ApJ*, 440:L41–L44, February 1995.

[59] S. Perlmutter et al. Measurements of the cosmolocial parameters Ω and Λ from the first seven supernovae at $z \geq 0.35$. *ApJ*, 483:565–581, July 1997.

[60] S. Perlmutter and B. P. Schmidt. Measuring Cosmology with Supernovae. In *LNP Vol. 598: Supernovae and Gamma-Ray Bursters*, page 195, 2003.

[61] M. M. Phillips. The absolute magnitudes of Type Ia supernovae. *ApJL*, 413:L105–L108, August 1993.

[62] M. M. Phillips, P. Lira, N. B. Suntzeff, R. A. Schommer, M. Hamuy, and J. Maza. The Reddening-Free Decline Rate Versus Luminosity Relationship for Type Ia Supernovae. *AJ*, 118:1766–1776, October 1999.

[63] A. G. Riess, A. V. Filippenko, P. Challis, A. Clocchiatti, A. Diercks, P. M. Garnavich, R. L. Gilliland, C. J. Hogan, S. Jha, R. P. Kirshner, B. Leibundgut, M. M. Phillips, D. Reiss, B. P. Schmidt, R. A. Schommer, R. C. Smith, J. Spyromilio, C. Stubbs, N. B. Suntzeff, and J. Tonry. Observational Evidence from Supernovae for an Accelerating Universe and a Cosmological Constant. *AJ*, 116:1009–1038, September 1998.

[64] A. G. Riess, A. V. Filippenko, W. Li, and B. P. Schmidt. Is there an Indication of Evolution of Type Ia Supernovae from their Rise Times? *AJ*, 118:2668–2674, December 1999.

[65] A. G. Riess, R. P. Kirshner, B. P. Schmidt, S. Jha, P. Challis, P. M. Garnavich, A. A. Esin, C. Carpenter, R. Grashius, R. E. Schild, P. L. Berlind, J. P. Huchra, C. F. Prosser, E. E. Falco, P. J. Benson, C. Briceño, W. R. Brown, N. Caldwell, I. P. dell'Antonio, A. V. Filippenko, A. A. Goodman, N. A. Grogin, T. Groner, J. P. Hughes, P. J. Green, R. A. Jansen, J. T. Kleyna, J. X. Luu, L. M. Macri, B. A. McLeod, K. K. McLeod, B. R. McNamara, B. McLean, A. A. E. Milone, J. J. Mohr, D. Moraru, C. Peng, J. Peters, A. H. Prestwich, K. Z. Stanek, A. Szentgyorgyi, and P. Zhao. BVRI Light Curves for 22 Type IA Supernovae. *AJ*, 117:707–724, February 1999.

[66] A. G. Riess, W. H. Press, and R. P. Kirshner. A Precise Distance Indicator: Type Ia Supernova Multicolor Light-Curve Shapes. *ApJ*, 473:88, December 1996.

[67] A. G. Riess, L. Strolger, J. Tonry, Z. Tsvetanov, S. Casertano, H. C. Ferguson, B. Mobasher, P. Challis, N. Panagia, A. V. Filippenko, W. Li, R. Chornock, R. P. Kirshner, B. Leibundgut, M. Dickinson, A. Koekemoer, N. A. Grogin, and M. Giavalisco. Identification of Type Ia Supernovae at Redshift 1.3 and Beyond with the Advanced Camera for Surveys on the Hubble Space Telescope. *ApJL*, 600:L163–L166, January 2004.

[68] A. Saha, A. Sandage, G. A. Tammann, A. E. Dolphin, J. Christensen, N. Panagia, and F. D. Macchetto. Cepheid Calibration of the Peak Brightness of Type Ia Supernovae. XI. SN 1998aq in NGC 3982. *ApJ*, 562:314–336, November 2001.

[69] A. Sandage. The redshift-distance relation. II. The Hubble diagram and its scatter for first-ranked cluster galaxies: a formal value for q_0. *ApJ*, 178: 1–24, November 1972.

[70] A. Sandage. Observational tests of world models. *ARA&A*, 26:561–630, 1988.

[71] D. J. Schlegel, D. P. Finkbeiner, and M. Davis. Maps of Dust Infrared Emission for Use in Estimation of Reddening and Cosmic Microwave Background Radiation Foregrounds. *ApJ*, 500:525, June 1998.

[72] B. P. Schmidt, N. B. Suntzeff, M. M. Phillips, R. A. Schommer, A. Clocchiatti, R. P. Kirshner, P. Garnavich, P. Challis, B. Leibundgut, J. Spyromilio, A. G. Riess, A. V. Filippenko, M. Hamuy, R. C. Smith, C. Hogan, C. Stubbs, A. Diercks, D. Reiss, R. Gilliland, J. Tonry, J. Maza, A. Dressler, J. Walsh, and R. Ciardullo. The High-Z Supernova Search: Measuring Cosmic Deceleration and Global Curvature of the Universe Using Type Ia Supernovae. *ApJ*, 507:46–63, November 1998.

[73] D. N. Spergel, L. Verde, H. V. Peiris, E. Komatsu, M. R. Nolta, C. L. Bennett, M. Halpern, G. Hinshaw, N. Jarosik, A. Kogut, M. Limon, S. S. Meyer, L. Page, G. S. Tucker, J. L. Weiland, E. Wollack, and E. L. Wright. First-Year Wilkinson Microwave Anisotropy Probe (WMAP) Observations: Determination of Cosmological Parameters. *ApJS*, 148:175–194, September 2003.

[74] R. P. S. Stone. Spectrophotometry of Flux Calibration Stars for Hubble Space Telescope. *ApJS*, 107:423, November 1996.

[75] L.-G. Strolger, R. C. Smith, N. B. Suntzeff, M. M. Phillips, G. Aldering, P. Nugent, R. Knop, S. Perlmutter, R. A. Schommer, L. C. Ho, M. Hamuy, K. Krisciunas, L. M. Germany, R. Covarrubias, P. Candia, A. Athey, G. Blanc, A. Bonacic, T. Bowers, A. Conley, T. Dahlén, W. Freedman, G. Galaz, E. Gates, G. Goldhaber, A. Goobar, D. Groom, I. M. Hook, R. Marzke, M. Mateo, P. McCarthy, J. Méndez, C. Muena, S. E. Persson, R. Quimby, M. Roth, P. Ruiz-Lapuente, J. Seguel, A. Szentgyorgyi, K. von Braun, W. M. Wood-Vasey, and T. York. The Type Ia Supernova 1999aw: A Probable 1999aa-like Event in a Low-Luminosity Host Galaxy. *AJ*, 124: 2905–2919, November 2002.

[76] John L. Tonry et al. Cosmological results from high-z supernovae. *PASP*, 115:1340–1350, November 2003.

[77] M. Turatto. Classification of Supernovae. In *LNP Vol. 598: Supernovae and Gamma-Ray Bursters*, pages 21, 2003.

[78] D. A. Turnshek, R. C. Bohlin, R. L. Williamson, O. L. Lupie, J. Koornneef, and D. H. Morgan. An atlas of Hubble Space Telescope photometric, spectrophotometric, and polarimetric calibration objects. *AJ*, 99:1243–1261, April 1990.

[79] L. Verde, A. F. Heavens, W. J. Percival, S. Matarrese, C. M. Baugh, J. Bland-Hawthorn, T. Bridges, R. Cannon, S. Cole, M. Colless, C. Collins, W. Couch, G. Dalton, R. De Propris, S. P. Driver, G. Efstathiou, R. S. Ellis, C. S. Frenk, K. Glazebrook, C. Jackson, O. Lahav, I. Lewis, S. Lumsden, S. Maddox, D. Madgwick, P. Norberg, J. A. Peacock, B. A. Peterson, W. Sutherland, and K. Taylor. The 2dF Galaxy Redshift Survey: the bias of galaxies and the density of the Universe. *MNRAS*, 335:432–440, September 2002.

[80] J. Whelan and I. J. Iben. Binaries and Supernovae of Type I. *ApJ*, 186: 1007–1014, December 1973.

[81] S. E. Woosley and T. A. Weaver. The physics of supernova explosions. *ARA&A*, 24:205–253, 1986.